

**QUANTIFICATION AND MITIGATION OF
ATMOSPHERE-INDUCED EFFECTS ON
REPEAT-PASS DIFFERENTIAL SAR
INTERFEROMETRY OVER THE VOLCANO
*PITON DE LA FOURNAISE***

GEO 511 – Master's Thesis

University of Zurich - Faculty of Science - Department of Geography

Remote Sensing Laboratories RSL

Author: Philippe Ott
08603243

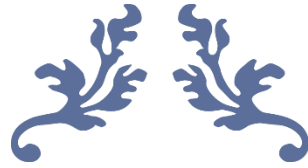
Supervisor: Dr. David Small (RSL)

Co-Supervisor: Dr. Adrian Schubert (RSL)

Faculty Member: Prof. Dr. Michael E. Schaepman (RSL)

Submitted on:
September 30st, 2016
Zürich, Switzerland





Acknowledgments

First and foremost, I would like to extend my deepest gratitude to my supervisor from the SARLAB Dr. David Small, who was leading and supporting me throughout my research period. The completion of this thesis would have not been possible without his encouragement and guidance. Also I am very grateful to him for giving me the opportunity to perform the master thesis with him and sharing his knowledge with me.

I am very thankful to my co-supervisor Dr. Adrian Schubert who stood as a backbone throughout my research period. He encouraged and helped me with his valuable suggestions and comments. I especially owe him my gratitude for offering some scripting steps and his knowledge, which made my work a success.

A special thanks to my friend Daniel Kükenbrink for extending his help whenever in need.

Most importantly, none of this could have happened without my mother with her own brand of humour. She has been kind and always supportive to me. Last but not the least, a very deep gratitude for encouragement to my friends Luca Moser, Leon Mehlau, Sandro Sax, Simon Schäfer, Tatjana Gal, Amedeo Cassina, Michael Moore, Simon Ljungberg, James Patrick and my family for creating a very friendly and cooperative environment and for providing me all the help and support I needed throughout my research.



Abstract

Observing the Earth's surface with repeat-pass Synthetic Aperture Radar (SAR) systems is a common geodetic technique. The satellite-based monitoring and mapping of the surface can reveal the Earth's topography and displacement but also may be affected by atmospheric artefacts. The study area of this thesis is located on an island in the western Indian Ocean, *La Réunion*. *Piton de la Fournaise* is a typical massive basaltic shield volcano sourced by a Hot Spot magma system sitting on the southeastern flank of the French Island of *La Réunion*. The Sentinel-1A (S1A) CSAR Instrument delivered Stripmap mode SAR data used in this thesis. Single Look Complex (SLC) data were processed to generate differential interferograms.

As the Interferometric Synthetic Aperture Radar (InSAR) technique is especially prone to tropospheric and ionospheric errors, it is essential to perform an atmospheric correction over the same study site. However, the atmosphere can interfere with the propagating wave signal from the SAR sensor and this can cause a signal delay, called path delay. The atmosphere-induced path delay can impair the quality of the received interferometric phase measurement and may lead to errors in estimations of the topography or displacement. Clouds and water vapour from the tropospheric layer and the free electrons measured in the Total Electron Content (TEC) from the ionospheric layer can cause the signals path delay. Therefore, an atmospheric correction model was estimated and applied to the Differential Interferometric Synthetic Aperture Radar (DInSAR) measurements. In detail, the corresponding tropospheric input parameters to calculate its path delay were atmospheric pressure, humidity (water vapour) and temperature provided in micro-scale by the modelled meteorological data set of ERA-Interim. The calculation of the ionospheric path delay was based on Total Electron Content (TEC) Maps from the Global Navigation Satellite System (GNSS) Network.

The DInSAR results showed that detection of surface displacement from the processed data of S1A was possible and led to acceptable results. However, the performed DInSAR output provided only a restrictive area of good coherence. Especially on a tropical island such as *La Réunion* the vegetation can cause significant decorrelation. In addition, the data has mostly large temporal baselines, reducing the coherence more. Considering the atmospheric aspects, a forward modelled path delay estimation was generated based on ERA-Interim modelled meteorological parameters and applied for mitigation of the DInSAR interferograms. The total atmospheric path delay (APD) difference showed that the ionospheric path delay difference is 9.2 times higher, respectively 5.1 times higher for the tropospheric path delay difference. The ionosphere-induced effect showed almost no variation (1%) over the study area. What was more interesting was the fact that the high variation of the troposphere-induced effect on the path delay difference was 40%, leading to a remarkable height-dependency over the observed volcano. Hence the APD estimation proved that the path delays were dependent on height. The mitigation method succeeded in reducing the height dependency caused mainly by the tropospheric wet delay. This used pixel wise APD mitigation method largely corrected the height-dependency induced by the troposphere. The output of this thesis presented an effective method to estimate and significantly mitigate the tropospheric and ionosphere-induced path delay based on repeat-pass SAR interferometry and ERA-Interims micro-scale atmosphere variables.

Keywords: SAR, InSAR, DInSAR, phase, spatial baseline, temporal baseline, path delay, atmosphere, troposphere, ionosphere, APD, ERA-Interim, TEC, Volcano, *La Réunion*, *Piton de la Fournaise*

Contents

Abstract	VII
Contents	IX
Symbols & Acronyms	XI
List of Figures	XIII
List of Tables	XVI
1. Introduction	1
1.1. DInSAR and the atmospheric influence	1
1.2. Motivation & Research Question	2
2. Theoretical Background	5
2.1. Fundamentals of SAR	5
2.1.1. SAR Interferometry	6
2.2. Atmospheric Influence	8
2.2.1. Meteorological-related Troposphere	10
2.2.2. Dependence of Ionosphere on the Sun	11
3. Data	13
3.1. Study Site	13
3.2. Digital Elevation Model	16
3.3. Acquisition modes of Sentinel-1A and data sets	18
3.4. Meteorological data of ERA-Interim.....	24
4. Methodology	29
4.1. SAR data processing	30
4.2. Meteorological data processing.....	34
4.3. Generation of path delay reference map for APD correction	37
5. Results	39
5.1. DInSAR Results	40
5.2. Generating the total APD difference	49
5.3. Atmospheric corrected DInSAR measurements.....	51
5.3.1. Pair One: 02.03.2016 & 07.04.2016.....	51
5.3.2. Pair Two: 02.03.2016 & 19.04.2016.....	53
6. Discussion	55
6.1. Phase to elevation relationship	55
6.2. DInSAR Phase consistency of displacement and noisy effects.....	56
6.3. Validation and processing of the atmospheric data	57
6.4. Three-dimensional DInSAR approach	58
7. Conclusion	59

8. Outlook	61
Bibliography	63
A. DInSAR Scene	73
B. Meteorology Data	76
C. Auxiliary product of the APD estimation and mitigation	78

Symbols & Acronyms

B_p or B_{\perp}	Parallel Baseline or Orthogonal Baseline. The component of the baseline between two or more data acquisitions [m]
f	Frequency (s^{-1})
I	Real Unit
Q	Imaginary Unit
γ	InSAR coherence value = $1 - \rho$
$\Delta\varphi$	Difference phase of the two or more SAR measurements
λ	wavelength [m]
π	pi (dimensionless)
ρ	InSAR Decorrelation value = $1 - \gamma$
φ	Phase value of a pixel expressed in $(0 \text{ to } 2\pi)$ or $(-\pi \text{ to } +\pi)$
1D, 2D, 3D	One-, Two-, Three-dimensional
ALOS	Advanced Land Observing Satellite
AOA	Angle Of Arrival fluctuation
APD	Atmospheric Path Delay
cm	Centimetre
C-Band	Certain portions of the electromagnetic spectrum: e.g. Sentinel-1, 5.546cm
COSMO-SkyMed	Constellation of small Satellites for the Mediterranean Basin Observation
CPM	Coregistration Polynomial
CSAR	C-Band based Synthetic Aperture Radar
DEM	Digital Elevation Model
DInSAR	Differential Interferometric Synthetic Aperture Radar
ECMWF	European Centre for Medium-Range Weather Forecasts
ERA-Interim	ECMWF Re-Analysis-Interim
ERS-1/2	ESA European Remote Sensing Satellites (ERS-1 and ERS-2)
ESA	European Space Agency
ENVISAT	ESA Environmental Satellite
GCP	Ground Control Point
GHz	Gigahertz
GIM	Global Ionospheric Map
GNSS	Global Navigation Satellite System
GPS	Global Positioning System
Hz	Hertz (s^{-1})
InSAR	Interferometric Synthetic Aperture Radar, SAR Interferometry
km	Kilometre
L-Band	Certain portions of the electromagnetic spectrum: e.g. ALOS, 23.6cm
LOS	Line of Sight
m	Meter
MAI	Multiple-Aperture SAR Interferometry
MERIS	Medium Resolution Imaging Spectrometer
MHz	Megahertz
mm	Millimetre
MODIS	Moderate Resolution Imaging Spectroradiometer
NASA	National Aeronautics and Space Administration
PSInSAR	Permanent (or persistent) scattered InSAR

RADAR	Radio Detection and Ranging
RMS	Root-Mean-Square
s	Second
S1A	Sentinel-1A
S1B	Sentinel-1B
S1C	Sentinel-1C
S1D	Sentinel-1D
S4	Stripmap mode 4
S6	Stripmap mode 6
SAR	Synthetic Aperture Radar
SBAS	Small BAseline Subset technique
SLC	Single-look complex
SM	Stripmap mode
SNAP	Sentinel Application Platform
SNAPHU	Statistical-Cost Network-Flow Algorithm for Phase Unwrapping
SNR	Signal to Noise Ratio
SRTM	Shuttle Radar Topography Mission (NASA)
StaMPS	Stanford Method for Persistent Scatterers
TanDEM-X	TerraSAR-X-Add-on for Digital Elevation Measurements
TEC	Total Electron Content
TID	Traveling Ionospheric Disturbance
TOPSAR	Topographic Synthetic Aperture Radar
X-Band	Certain portions of the electromagnetic spectrum: e.g. COSMO-SkyMed, 3.1 cm
XSAR	X-Band based Synthetic Aperture Radar
ZWD	Zenith Wet Delay

List of Figures

Figure 1: Repeat-pass imagine geometry, B : baseline, B_{\perp} : perpendicular baseline, B_p : parallel baseline, ζ : baseline angular, $S1,2$: position of the sensor/satellite, $\theta1,2$: angle of incidence, $r1,2$: slant range-vectors, P : target on surface (Meier, 2013).	6
Figure 2: (A) Point p (top) and q (foot) show the differential tropospheric delay due to their height difference, and the correspondent different vertical refractivity profile N^h during the SAR acquisition times t_1 and t_2 . (B) Delay curves of t_1 and t_2 indicating the point p and q . The results are shown by l_1 and l_2 which represent the effect of the delay of the SAR measurement caused by the atmosphere. In addition, the dashed line represents a cloud layer called c , which causes a shift of the cumulative delay below the cloud, indicated by the dotted line (Hanssen, 2002).	9
Figure 3: La Réunion Island via laser. S1A radar satellite test image taken on 26 May 2016, recorded and relayed to Earth by EDRS-A on 31 May 2016 (left). The study site of volcano Piton de la Fournaise (right) (ESA La Reunion Island via laser).	13
Figure 4: The three calderas are indicated in red lines on the Piton de la Fournaise. The first dotted line was reconstructed by field observations. The second could be observed at the point Pas des Sables in the volcanic area, whereas the eastern and southern extensions are estimated. (IPGP Le Piton de la Fournaise).	14
Figure 5: Precipitation zones of La Réunion (Climat et Hydrologie Etude climatique).	14
Figure 6: Temperature zones of La Réunion (Climat et Hydrologie Etude climatique).	15
Figure 7: DEM of the eastern part of La Réunion, grayscale map from sea level to highest point (Shuttle Radar Topography Mission 1 Arc-Second Global).	16
Figure 8: Shaded relief of the eastern part of La Réunion (Shuttle Radar Topography Mission 1 Arc-Second Global).	17
Figure 9: Characteristic of the SLCs based on the temporal baseline, own representation.	22
Figure 10: Characteristic of the SLCs based on the spatial baseline, own representation.	22
Figure 11: Characteristic of the SLCs based on the modelled coherence, own representation.	23
Figure 12: Characteristic of the SLCs based on the height ambiguity, own representation.	23
Figure 13: This represents the raster of the retrieved ERA-Interim modelled meteorological data overlaid on a coherence map, own representation based on Google Earth imagery.	25
Figure 14: Histogram about the elevation of the volcanic area, corresponding to figure 13, own representation.	25
Figure 15: Characteristic of the SLCs based on the modelled total APD difference. This is the total mean difference of ionospheric and tropospheric path delay, own representation.	26
Figure 16: Temperature data of ERA-Interim from July 2015 to June 2016.	27
Figure 17: The total cloud coverage data of ERA-Interim from July 2015 to June 2016.	27
Figure 18: Dew point temperature data of ERA-Interim from July 2015 to June 2016.	27
Figure 19: Surface pressure data of ERA-Interim from July 2015 to June 2016.	27
Figure 20: Dew point temperature data of ERA-Interim from July 2015 to June 2016.	27
Figure 21: Workflow diagram of the processing steps for SLC data from S1A in S6. In addition, the processing of the meteorological data set. Boxes were made based on the used software, own representation.	29
Figure 22: A simplified visualization of a sinking or rising surface modification can be interpreted using InSAR/DInSAR. Important are the sequences of colors (yellow, red, pink, blue, green and yellow again), which correspond to a C-Band (S1A/B/C/D, ENVISAT, ERS, RADARSAT-1, etc.) measurements of a 28 mm (wavelength by two) LOS change. Depending on the direction of movement, the gradient is in the opposite color scheme, (Dzurisin, 2007: 13).	31
Figure 23: A simplified visualization of a sinking or rising surface modification can be interpreted using InSAR. Important are the sequences of colors (yellow, red, pink, blue, green and yellow again), which correspond at a C-band (Sentinel-1A, ENVISAT, ERS, RADARSAT-1, etc.) measurements of a 28 mm (wavelength by two) LOS change. Depending on the form of movement of the gradient is the opposite, from . 13.	31

Figure 24: Coherence output of pair One including the corresponding histogram of the represented values, own representation.....	40
Figure 25: Coherence output of pair Two including the corresponding histogram of the represented values, own representation.....	41
Figure 26: Wrapped phase values in radians of pair One. Also a demonstration of the bandwidth of the values $[-\pi, \pi]$, own representation	42
Figure 27: Wrapped phase values in radians of pair Two. Also a demonstration of the bandwidth of the values $[-\pi, \pi]$, own representation	43
Figure 28: Unwrapped phase values in radians of pair One. Minimum and maximum of the unwrapped phase represented, own representation.....	44
Figure 29: Unwrapped phase values in radians of pair Two. Minimum and maximum of the unwrapped phase represented, own representation,.....	45
Figure 30: Unwrapped absolute values converted into cm of pair One.	46
Figure 31: Unwrapped absolute values converted into cm, showing only the coherent pixels with values above 0.4 of pair One.....	47
Figure 32: Unwrapped absolute values converted into cm of pair Two.	47
Figure 33: Unwrapped absolute values converted into cm, showing only the coherent pixels with values above 0.4 of pair Two.....	48
Figure 34: Total APD difference of pair One.	50
Figure 35: Total APD difference of pair Two.	50
Figure 36: Atmospheric corrected DInSAR measurement with the total APD difference of pair One.	51
Figure 37: Density map based on the elevation of the volcanic area and the unwrapped absolute values of the DInSAR measurement of pair One.	52
Figure 38: Density map based on the elevation of the volcanic area and the atmospheric corrected DInSAR measurement with the APD of pair One.....	52
Figure 39: Density map based on the total APD difference and the unwrapped absolute values of the DInSAR measurement of pair One.	52
Figure 40: Density map based on the total APD difference and the atmospheric corrected DInSAR measurement with the APD of pair One.....	52
Figure 41: Atmospheric corrected DInSAR measurement with the total APD difference of pair Two.	53
Figure 42: Density map based on the elevation of the volcanic area and the unwrapped absolute values of the DInSAR measurement of pair Two.	54
Figure 43: Density map based on the elevation of the volcanic area and the atmospheric corrected DInSAR measurement with the APD of pair Two.	54
Figure 44: Density map based on the total APD difference and the unwrapped absolute values of the DInSAR measurement of pair Two.....	54
Figure 45: Density map based on the total APD difference and the atmospheric corrected DInSAR measurement with the APD of pair Two.	54
Figure 46: Intensity image in VV Polarization in ascending mode of SLC 02.03.2016. Product level: LI. Product name: S1A_S6_SLC__ISDV_20160302T145244_20160302T145307_010191_00F0AD_D28E.	73
Figure 47: Intensity image in VV Polarization in ascending mode of SLC 07.04.2016. Product level: LI. Product name: S1A_S6_SLC__ISDV_20160407T145244_20160407T145308_010716_00FFC7_A6F9.	74
Figure 48: Intensity image in VV Polarization in ascending mode of SLC 19.04.2016. Product level: LI. Product name: S1A_S6_SLC__ISDV_20160419T145245_20160419T145309_010891_01050B_A397.....	75
Figure 49: Correlation of atmospheric pressure meteorological data between the meteorological station St. Denis Gillot. The station is 20m above sea level.....	76
Figure 50: Correlation of relative humidity meteorological data between the meteorological station St. Denis Gillot. The station is 20m above sea level.....	76
Figure 51: Correlation of temperature meteorological data between the meteorological station St. Denis Gillot. The station is 20m above sea level.....	77

<i>Figure 52: Correlation of cloud cover meteorological data between the meteorological station St. Denis Gillot</i>	<i>77</i>
<i>Figure 53: TEC Maps for the three SLC acquisition dates.....</i>	<i>78</i>
<i>Figure 54: Unwrapped absolute values converted into cm, showing only the coherent pixels with values above 0.4 of pair One.....</i>	<i>79</i>
<i>Figure 55: Atmospheric corrected DInSAR measurement with the total APD difference, showing only the coherent pixels with values above 0.4 of pair One.....</i>	<i>79</i>
<i>Figure 56: Only total ionospheric path delay difference (two-way) of pair Two.....</i>	<i>80</i>
<i>Figure 57: Only total tropospheric path delay difference (two-way) of pair Two.....</i>	<i>80</i>
<i>Figure 58: Unwrapped absolute values converted into cm, showing only the coherent pixels with values above 0.4 of pair Two.....</i>	<i>81</i>
<i>Figure 59: Atmospheric corrected DInSAR measurement with the total APD difference, showing only the coherent pixels with values above 0.4 of pair Two.....</i>	<i>81</i>
<i>Figure 60: Only total ionospheric path delay difference (two-way) of pair Two.....</i>	<i>82</i>
<i>Figure 61: Only total tropospheric path delay difference (two-way) of pair Two.....</i>	<i>82</i>

List of Tables

<i>Table 1: Characteristics of SAI satellite (Fletcher, 2012).</i>	18
<i>Table 2: Overview of Sentinels-1A various measurement modes (Fletcher, 2012).</i>	19
<i>Table 3: Characteristics of Sentinels-1A Stripmap mode 6 (Fletcher, 2012).</i>	20
<i>Table 4: Weather station at the Airport of La Réunion (Historical Weather St. Denis Gillot).</i>	24
<i>Table 5: Product information of the 02.03.2016 SLC, own representation.</i>	28
<i>Table 6: Product information of the 07.04.2016 SLC, own representation.</i>	28
<i>Table 7: Product information of the 19.04.2016 SLC, own representation.</i>	28
<i>Table 8: Average and seasonal variation magnitudes of the temperature and water vapour lapse rates (Schubert and Small, 2016).</i>	35
<i>Table 9: Pair One - SLC from 02.03.2016 & 07.04.2016 and its characteristics, own representation.</i>	39
<i>Table 10: Pair Two - SLC from 02.03.2016 & 19.04.2016 and its characteristics, own representation.</i>	39
<i>Table 11: The atmospheric path delay measured on time and date of the SLC acquisition. Minimum, maximum and mean values are shown in correspondence to the respective atmospheric layer, own representation.</i>	49
<i>Table 12: Total APD difference of the particular SLC is subtracted for obtaining the path delay difference, own representation.</i>	49

1. Introduction

Smoking and fire-breathing mountains have always threatened humankind. The phenomenon of volcanism has often endangered fields and homes. A quote from Günter Kunert (1962) reflects this contradiction: *"Auf einem Vulkan lässt sich leben, besagt eine Inschrift im zerstörten Pompeji."* Today volcanoes are still a mystery. Worldwide there are approximately 1900 potentially active volcanoes, where let people live in danger until today.

Preliminary findings from the observation of volcanoes using remote sensing have become an indispensable basis for decision making. Remote sensing has intensified satellite-based Radio Detection and Ranging (RADAR) systems in the past decades. Synthetic aperture radars (SAR) are advanced, high-resolution and active radar systems can illuminate an area of investigation independently, depending on its specific viewing angle. This sensing technique works in the electromagnetic spectrum with wavelengths from 1 meter (m) to 1 centimetre (cm) (Massonnet and Souyris, 2008). Imaging works independent of the meteorological conditions during both, day and night. The resolution of a SAR system is independent of the distance to the scene in principle, also large areas can be measured in a very short sensing time. Advanced signal processing combined with the orbit of a satellite, make SAR to a powerful and useful remote sensing technique, able to provide a high spatial resolution (Balaji, 2011). Applications such as high precision Interferometric Synthetic Aperture Radar (InSAR) and Differential Interferometric Synthetic Aperture Radar (DInSAR) can be used to identify small surface displacements with millimetre (mm) to cm accuracy. Interferometric SAR and differential InSAR methods have been widely used (Kim and van Zyl, 1998; Amelung et al., 2000; Beauducel et al., 2000; Dzurisin, 2007; Sigmundsson et al., 2010; Balaji, 2011; Stramondo et al., 2014; González et al., 2015). The literature reveals a broad list of InSAR and DInSAR based application studies, such as surface displacement caused by land subsidence associated with underground water (Fruneau et al., 2005) or surface movement studies of different volcanos (Beauducel et al., 2000; González et al., 2015).

1.1. DInSAR and the atmospheric influence

To generate an interferometric product, two or more SAR images over the same scene have to be acquired at different times. The focus lies in this context more on the phase measurement to extract terrain information and therefore it is possible to retrieve height information from SAR data using the phase of the transmitted and received wave (Crosetto, 2002). A comparison between two or more phase measurements can lead to a path length difference, which can be a fraction of a wavelength (Woodhouse, 2005). This principle of superposition of two or more waves is called interference and is based on the phase shift of two or more SAR images (Rees and Rees, 2013).

First, it is important to understand that an interferogram contains different layers of information. These layers are widely mixed together and cannot be easily distinguished. The superposition of phase information delivers on one hand the surface displacement, the topography, various sources of noise and on the other hand containing atmospheric effect (Sarti et al., 1999; Rosen et al., 2000).

It is well known that interferometric measurements are influenced by several complex confounding factors, especially the Earth's atmosphere (Goldstein, 1995; Zebker et al., 1997). The SAR signal passes through the atmosphere twice before the platform receives the backscattered signal from the Earth's surface (two-way). In addition, a repeat-pass SAR system is even more sensitive due to the temporal and spatial baseline and the changing atmospheric heterogeneities (Goldstein, 1995; Balaji, 2011). According to this, the atmosphere modifies the SAR signal and causes a signal delay, called path delay. This effect can vary in time and space and therefore it is important to understand and identify this matter

to estimate, correct and interpret the interferometric measurements (Beauducel et al., 2000; Li et al., 2007). The literature shows numerous studies on quantification and mitigation of atmospheric delays effectively (Askne and Nordius, 1987; Zebker et al., 1997; Williams et al., 1998; Sarti et al., 1999; Hanssen, 1999; Beauducel et al., 2000; Bonforte et al., 2001; Wadge et al., 2002; Li et al., 2003; Emardson et al., 2003; Janssen et al., 2004; Li, 2005; Lohman and Simons, 2005; Puyssegur et al., 2007; Ding et al., 2008; Danklmayer et al., 2009; Doin et al., 2009; Li et al., 2009a; Li et al., 2009b; Jung et al., 2014).

Some studies showed methods to estimate the Atmospheric Path Delay (APD) of SAR measurements based on GPS (Wadge et al., 2002; Li et al., 2003; Li, 2005), on meteorological information of a meteorological station (Bonforte et al., 2001) or on ESA Environmental Satellite's (ENVISAT) Medium Resolution Imaging Spectrometer (MERIS) / Moderate Resolution Imaging Spectroradiometer (MODIS) based multispectral data. Emardson et al. (2003) demonstrated a statistical approach to perform a separation of the stochastic noise from surface movements (Doin et al., 2009). Further studies of Peltzer et al. (2001) and Schmidt (2005) performed a time independent stacking method: Bonforte et al. (2001) and Berardino et al. (2002) reduced atmospheric noise by applying a temporal low-pass filter or creating time series to smooth the interferometric data, given that no ground movement has occurred in the test area. The above listed studies used various approaches. Hanssen (1999) demonstrated early various atmospheric correction options, and special data processing. Although several studies reveal different approaches, there is no standard atmospheric correction method. This thesis continues the successive work based on following studies as Baby et al. (1988), Delacourt et al. (1998) and Taylor and Peltzer (2006), Elliott et al. (2008) and Doin et al. (2009) that used an elevation-dependent filter based on an atmospheric model fed with meteorological data (temperature, partial pressure, water vapour and humidity) close to the study site, extrapolating the values to higher elevations (Doin et al., 2009).

Until today, it remains a challenge to estimate short term meteorological related errors, that can affect the DInSAR measurement. There is still a certain insufficiency of understanding and the lack of comprehensive methods (Puyssegur et al., 2007). Therefore, obtaining methods for estimating and correcting the properties of the atmospheric effects remains a topic of research (Li et al., 2007).

1.2. Motivation & Research Question

To ensure the accuracy of surface displacement using an interferometric approach, it is necessary that the measured values are reliable at cm or mm level. Therefore, it is of importance to estimate and correct the interferometric measurements for the encountered atmospheric signal delay; further external effects also exist. Emardson et al. (2003) said that the propagation delays in the atmosphere cause the dominant noise source for interferometric measurements and might be a limiting parameter for, observing cm or mm displacement movement. Differential InSAR measurements in combination with atmospheric analysis require a suitable study site: for example, a volcano. On the island of *La Réunion* there is an active and currently erupting volcano. This study area is convenient because it fulfils the need of the turbulent mixing of the atmosphere, which are mainly due to spatial heterogeneity in refractivity during a SAR acquisitions and effects flat as well as mountainous terrain (Rosen et al., 1996; Ding et al., 2008). More important, it surely complies the demand of the vertical stratification profile, which varies with different height (Bonforte et al., 2001; Hanssen, 2002). Also the fact that the volcano is based on a tropical island and the volcanos foothills reach into the ocean, qualifies the study site. The drawback of this study area is the tropical climate which may lead to strong vegetation that can reduce the image coherence. The processed SAR data was organised in Stripmap mode 6 (S6) of Sentinel-1A (S1A). An assessment regarding ground displacement was performed to evaluate that no surface movement between the two image acquisitions occurred. This helped to isolate atmospheric signatures. The shallow

angle of the S6 acquisition mode allowed having even a longer travelling time through the atmosphere and therefore encounter as much atmospherical signal delay as possible. A pixel based path delay model of RSL (Jehle et al., 2008; Schubert and Small, 2016) was fed with high resolution ERA-Interim data to be able to calculate and estimate the precise APD for the volcano. The APD estimation was applied on the DInSAR measurements for correction.

This thesis has its aim to perform DInSAR measurements of *Piton de la Fournaise* and estimate the APD caused by the atmosphere for mitigation. Therefore, the following research questions were evaluated and assessed:

- Which components of the atmosphere control the electromagnetic waves emitted of satellite-based SAR systems in the repeat-pass mode as Sentinel-1A Stripmap mode 6?
- How strong and with which magnitude do the atmospheric dishomogeneities affect the interferometric phase signal on a tropical island as *La Réunion* ?
- What are the methods to estimate and correct the atmospheric effects on different SAR interferograms in the case of a volcanic scenario, and does the correction properly mitigate for atmospheric effects?

To answer these research questions, this thesis is structured as following. In the beginning a brief theoretical background introduces the topic of interferometry and gives insight; into why and how severe the atmosphere properties modify SAR signals. This is followed by information about the chosen study site and the used datasets. The succeeding chapter is about the methodology, containing the developed methods and the correspondent processing steps of this thesis. In the next chapter, the conducted results of the methods are presented. In the discussion, the obtained and relevant results corresponding to the research question are debated and correlated with existing research literature. A critical analysis of the used methods is induced. In the end, the thesis concludes along with an outlook.

2. Theoretical Background

Before focusing at the data set and the methodology, it was necessary to have a short theoretical overview for comprehension of the various involved parameters. This section is specifically addressed to the topic of surface measurements by SAR interferometry and how the Earth's atmosphere is involved in the SAR measurement process.

2.1. Fundamentals of SAR

A widespread imaging technique called SAR processing, containing an amplitude and a phase, which are calculated from a re-radiated object and are processed to a complex-valued SAR image (Woodhouse, 2005). The received echoes of the SAR are multiplied by a reference signal and by means of a quadrature system split into a real unit (I) and an imaginary unit (Q) component (Ferretti et al., 2007; Meier, 2013).

$$\text{Amplitude} \quad A = \sqrt{I^2 + Q^2} \quad (\text{Meier, 2013: 42}) \quad (2.1)$$

$$\text{Phase} \quad \varphi = \text{atan}\left(\frac{Q}{I}\right) \quad (\text{Meier, 2013: 42}) \quad (2.2)$$

The product, after successful processing the raw SAR data, is a Single-Look Complex image (SLC), that contains an amplitude and phase image. Thus, SAR recording (amplitude) is a representation of the wavelength-dependent backscatter mechanisms, represented in a gray scale image (Massonnet and Souyris, 2008; Meier, 2013). The intensity of the signal strength in the form of an electromagnetic wave is characterized by surface inclinations, surface roughness and surface conductivity (Trevett, 1987). The phase of a SAR image depends on other factors, such as the path length (sensor-surface-sensor) and the interaction of the signal with the material properties depend (Allen, 1995). The path length is proportional to the transit time, which in turn is the speed of light in proportion. It should be noted that the speed of light is influenced by water molecules (troposphere) and electrons (ionosphere). Finally, this effect can lead to delay or speed up the transit time, which leads to a change of speed and can affect the phase measurement. This problem will be discussed later in this thesis (chapter 2.2). The different wavelengths (λ) vary from 1 mm to 1 m and the equivalent frequency (f) ranges from 300 Megahertz (MHz) to 300 Gigahertz (GHz): X-band (8-12 GHz = f , $\lambda = 2.5\text{-}3.75$ cm), C-Band ($f = 4\text{-}8$ GHz, $\lambda = 3.75\text{-}7.5$ cm) and L-band ($f = 1\text{-}2$ GHz, $\lambda = 15\text{-}30$ cm). With respect to this work, only the C-Band for the S1A platform was considered (Ferretti et al., 2007).

In this thesis, the focus lied on the repeat-pass / monostatic data acquisition. This recording method was done with a single satellite (S1A), which covered the same scene (multiple-pass, multi-baseline) at least two or more times. In the past, there were similar missions (European Remote Sensing Satellites (ERS-1/2), TerraSAR-X-Add-on for Digital Elevation Measurements (TanDEM-X), Constellation of small Satellites for the Mediterranean Basin Observation (COSMOS-SkyMed) etc.) that worked with a monostatic data acquisition procedure. Tandem programs consist a pair of satellites, that passes within short time sequences with slightly different orbits to generate precise DInSAR outputs and decent Digital Elevation Models (DEM). Even though Sentinel-1B (S1B) was already shot into orbit, the Sentinel missions were not considered as a tandem mission. S1B is cutting the revisiting times down from 12 days to 6 days at the equator (ESA Sentinel-1A & Sentinel-1B delivers). Sentinel-1C (S1C) and Sentinel-1D (S1D) are joining soon, offering an even shorter revisiting time (ESA Sentinel-1 SAR Revisit and Coverage).

By using repeat-pass modes, it is likely that an altered imaging geometry results when passing the same scene. This deviation can affect the coherence of the image. A strong decorrelation might lead to difficulties in comparability. It is important that accurate orbit information, the imaging modes of satellites and its polarization are available and traceable (Gupta, 2013).

Leading over to the concept of baseline, there are two different types of baselines, the spatial and temporal baseline. The spatial baseline is the spatial distance (m) between two or more flight paths of the sensor. This consists the normal/orthogonal baseline (B_{\perp}) and the secondly parallel baseline (B_p). In addition to the spatial baseline, there is a temporal baseline (day), relying on the overflight intervals of satellite (Ferretti et al., 2007; Massonnet and Souyris, 2008; Meier, 2013).

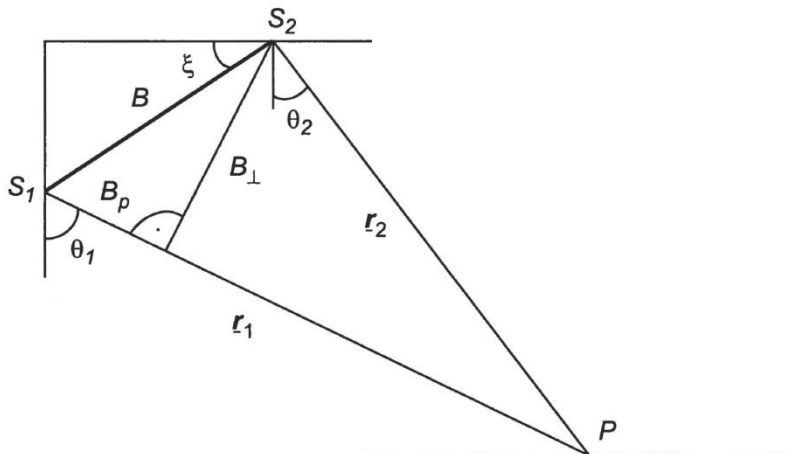


Figure 1: Repeat-pass imagine geometry, B : baseline, B_{\perp} : perpendicular baseline, B_p : parallel baseline, ξ : baseline angular, $S1,2$: position of the sensor/satellite, $\theta1,2$: angle of incidence, $r1,2$: slant range-vectors, P : target on surface (Meier, 2013).

2.1.1. SAR Interferometry

Space-borne InSAR is used for topography and displacement measurement and is a widely used technology to determine surface changes in the cm and mm range. Products and results of this method are DEMs and interferograms (Ferretti et al., 2007; Stramondo et al., 2014). As the Earth's surface is affected of geophysical processes like displacement phenomena, several investigation were done for analysis of natural events such as volcano unrest periods (Mogi, 1958) and landslides (Farrell, 1972). SAR played a major role to detect such natural phenomena by providing high-resolution microwave images in any weather condition (Ferretti et al., 2015). Compared to infrared radiation, microwaves have the ability of traversing clouds, fog, and possible ash or powder coverage, in case of an erupting volcano. Besides this, some atmospheric disturbances can affect both the amplitude and, more importantly, the phase of SAR images (Sansosti et al., 2015), (Costantini et al., 2016).

The focus lied in this context more on the phase measurement to extract terrain information (Crosetto, 2002), (Massonnet and Souyris, 2008). A measurement of a single phase is usually not useful, as the absolute wave cycle is rarely known. A comparison instead between two or more phase measurements can lead to a path length difference, that can be a fraction of a wavelength (Woodhouse, 2005; Kükenbrink, 2014).

This principle of superposition of two or more waves is called interference and is based on the phase shift of two or more SAR images over the same scene taken at different times (Rees and Rees, 2013). For example, one of the two images is the reference image (master), the others are defined as additional images (slave). Phase measurements were not available for a long time, since the phase of the echo was

a random variable. When two congruent SAR phases contrast each other, there is a connection between two arbitrary resolution cells. Therefore, the requirement of two transmitter positions with different distances is requested (Meier, 2013; Rees and Rees, 2013). However, the baseline should come to lie within the system given critical value (maximum distance between the antenna positions), as well as the temporal baseline should not be too strongly stressed and the wavelength should be congruent by two acquisitions. The result is a path length difference which corresponds to the interferometric phase (0 to 2π or $-\pi$ to $+\pi$). The phase difference of two acquisitions is often related for a two-way path length difference (ΔR) and will be noted as the following (Bamler and Philipp Hartl, 1998; Gens and van Genderen, 2007):

$$\delta\phi = 2\pi \frac{\Delta R}{\lambda} \quad (2.3)$$

Where the phase difference $\delta\phi$ is measured in radians and λ stands for the wavelength. An interferogram can be created by a pixel wise cross-multiplying function. This technique is only applicable when a coherent signal is detected. But especially in practice some of the phase measurements show incoherence and this provides no meaningful information. Also the interferograms is often influenced by noise (e.g. radar shadow, vegetation/leaf movement). Therefore, only meaningful phase information is required and can be processed. This directs to the topic of coherence, which is the complex correlation between the phase information of the two complex SAR images (Kükenbrink, 2014). This coherence provides the information how well the two single phase values correlate with each other. This leads to the question of how consistent the prediction of the phase difference is in the interferogram (Ferretti et al., 2007; Kükenbrink, 2014). The calculation of the coherence $|\gamma|$ is stated here:

$$\gamma = \frac{\sum_N p_1 p_2^*}{\sqrt{\sum_N |p_1|^2 \sum_N |p_2|^2}} \quad (2.4)$$

Where p_1 and p_2 are pixel values and N is the number of pixels in the N -sample window used to estimate the coherence. The magnitude of the complex correlation coefficient γ , called the interferometric coherence and can be used to detect changes in the observed target over time between two acquisitions (Koppel et al., 2015). The magnitude of the InSAR coherence value = $1 - \rho(\gamma)$ ranges from 0 to 1. Note that γ is a complex number and it corresponds to the phase difference and the amplitude and its meaningfulness. A coherence value of $|\gamma|=1$ means a complete correlation (fully coherent), where $|\gamma|=0$ provides a complete decorrelation (Zebker and Villasenor, 1992; Bamler and Philipp Hartl, 1998). Natural targets tend to lose coherence faster than non-natural targets, giving raise to the use of the coherence parameter for detecting built-up, anthropological areas (Zebker et al., 1997; Ferretti et al., 2007; Koppel et al., 2015; Spaans and Hooper, 2016).

2.2. Atmospheric Influence

There are several phenomena caused by the atmosphere that influences InSAR/DInSAR measurements, like meteorological-related cases, damping and refractive effects, which lead to distortion, clutter and really affect the travelling signal for a space-borne SAR system working in a 0.2–3.0 GHz frequency range (Bilow, 1984). It is well known that propagating waves, like amplitudes and phases, fluctuate and vary in time and space. Especially in this case of a repeat-pass space-borne SAR system, the troposphere, the ionosphere and the interstellar media effects the fluctuation of altering energy distribution, skewness, kurtosis, broadening pulse width and first and most notably of arrival time, resp. the time of path propagation. In relation to the InSAR measurements, where the signals are sent to the Earth's surface and back, the signal is effected by a two-way propagation. In the context of repeat-pass InSAR measurement, the phase difference in time is a serious problem, because the two rays must pass through completely different propagation media at different times, depending on the revisit times of the sensor, leading to different travelling times know as phase delays resp. path delays (Li, 2005; Schubert et al., 2015). Therefore, the SAR acquisitions include artefacts that are spatially and temporally variable based on the atmosphere variation. This leads to a major limitation in accuracy (Janssen et al., 2004). The atmosphere-induced effects on the interferometric measurements need to be taken into account and should possibly be corrected by a correction method or filter (Kim and van Zyl, 1998). Goldstein (1995), Tarayre and Massonnet (1996) and Massonnet and Feigl (1998) demonstrated that the atmospheric delay variation might cause interpretation issues of interferogram. It is currently impossible to measure the refractivity distribution causing the delay simultaneously with a SAR acquisition (Hanssen, 2002). There are two types of atmospheric effects in SAR interferometry, based on their physical origin: The turbulent atmospheric mixing and the vertical stratification.

Turbulent mixing in the atmosphere

The turbulent mixing causes spatial heterogeneity in refractivity during a SAR acquisitions and effects flat as well as mountainous terrain (Rosen et al., 1996; Hanssen, 2002; Janssen et al., 2004; Ding et al., 2008). In general, there are three special conspicuity of atmospheric signals in interferograms:

- An absolute signal of atmospheric delay cannot be observed of the relative character of a single interferogram, because the total atmospheric delay can be the same but differ in its vertical refractivity composition. The orbit errors can easily cause a linear trend over the entire interferometric scene. These trends are hard to detect from atmospheric signal delay trends but can be eliminated, using a residual flattening, such as tie-points or high-pass Filter).
- Also the temporal variability of the atmospheric signal is broad. On one hand, there might be a SAR acquisition without any atmospheric influence, but on the other hand the next acquisition, will show a strong atmospheric influence. Hence, it is said that the acquisition time intervals of more than one day leads to an uncorrelated atmosphere setting (Hanssen, 2002).
- Numerous studies demonstrated, that the distribution of water vapour in the lower troposphere is the predominant factor, causing atmospheric signal delay (Goldstein, 1995; Tarayre and Massonnet, 1996; Hanssen and Feijt, 1997; Zebker et al., 1997; Hanssen, 1998; Crosetto et al., 2005; Ding et al., 2008).

This leads to the corollary of the fact that for microwave frequencies, the permanent molecular dipole moment of H₂O dominates the variability of the refractive index. Hence, Ishimaru (1978) demonstrated that, the more water vapour is in the atmosphere, the more mechanical turbulence will occur. For instance, the water vapour saturation on a windward and leeward sides of a mountain, is most likely to differ due to the high variability of the temporally and spatially turbulent patterns at each acquisition date (Doin et al., 2009). Ducret (2013) said that the fluctuation caused by the atmospheric turbulence

might reach up to one or two fringes in C-Band interferograms. These effects can be removed by the method of interferogram stacking (Zebker et al., 1997; Peltzer et al., 2001), with InSAR time series (Ferretti et al., 2001; Cavalié et al., 2007) or with an elevation-dependent filter based on an atmospheric model fed with meteorological data (Baby et al., 1988; Delacourt et al., 1998; Taylor and Peltzer, 2006; Elliott et al., 2008; Doin et al., 2009)

Vertical stratification in the troposphere

The vertical stratification results from the different vertical refractivity profile in the atmosphere between SAR acquisitions, assuming there are no heterogeneities within the horizontal layers. This is based on the phase difference between two arbitrary resolution cells with different topographic heights (Hanssen, 2002; Ding et al., 2008; Doin et al., 2009). This effects were particularly seen over high topographic structures as mountains or volcanos, because of the variable tropospheric path length and the correspondent local air flow induced by the topography (Wadge et al., 2002; Ding et al., 2008; Doin et al., 2009). This phenomenon was explored while deformation studying Mount Etna (Tarayre and Massonnet, 1996; Massonnet and Feigl, 1998; Delacourt et al., 1998; Ferretti et al., 2001). This effect correlates with topography and affects only mountainous areas (Hanssen, 2002; Massonnet and Feigl, 1998). In a study of Hanssen (2002) it can be shown, that the atmospheric path delay could reach up to more than 1cm for a height interval of 500m or more. In case of flat areas, there was almost no horizontal delay difference, even for different refractivity profiles during SAR acquisitions. Since it is justified that interferograms weren't sensitive to image-wide phase biases (Hanssen, 2002; Ding et al., 2008; Doin et al., 2009).

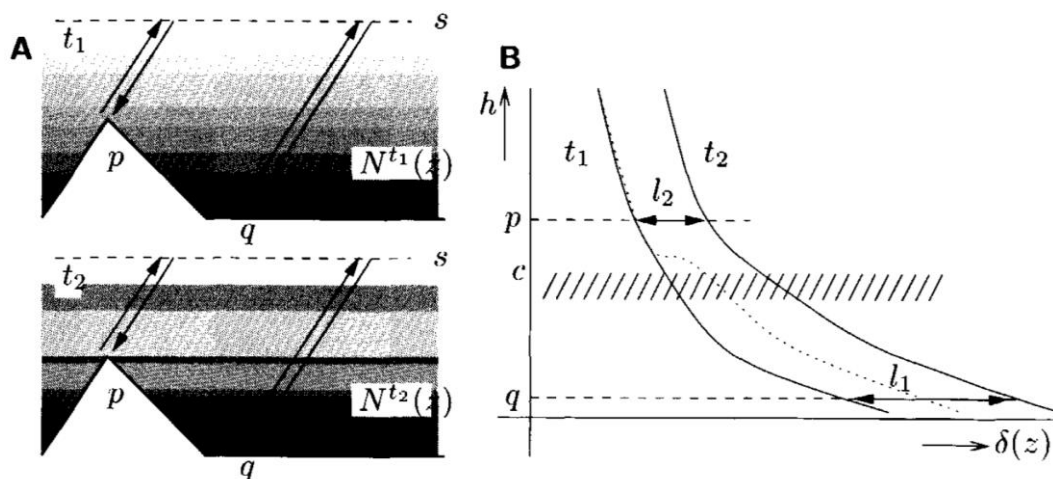


Figure 2: (A) Point p (top) and q (foot) show the differential tropospheric delay due to their height difference, and the correspondent different vertical refractivity profile N during the SAR acquisition times t_1 and t_2 . (B) Delay curves of t_1 and t_2 indicating the point p and q . The results are shown by l_1 and l_2 which represent the effect of the delay of the SAR measurement caused by the atmosphere. In addition, the dashed line represents a cloud layer called c , which causes a shift of the cumulative delay below the cloud, indicated by the dotted line (Hanssen, 2002).

Overall, a phase difference from two resolution cells of an interferogram has most likely a phase error, and the observed phase gradients are often a combination of differential vertical stratification, displacement, horizontal atmospheric heterogeneity and topographic residuals. Hence, it is not possible to simply determine the error source of the phase error on interferograms (Sarti et al., 1999). There are different studies, in which radiosondes were used to study the vertical radiosondes profile and calculate the statistics of the delay variation referring to height intervals (Hanssen, 2002; Li et al., 2003; Ding et al., 2008). In this thesis, another approach was performed, by interpolating and calculating the in-situ meteorological micro-scale data from ERA-Interim for the certain acquisition dates of the SAR acquisitions to receive an estimation of the path delay caused by the atmosphere.

2.2.1. Meteorological-related Troposphere

The non-ionized troposphere is defined as the part of the atmosphere that stretches from the Earth's surface to a height of approximately 52 kilometre (km) (Janssen et al., 2004). Most of the path delays typically occur in the lower part of the troposphere (first 10km) and depend on the atmospheric pressure, humidity (water vapour), and temperature. In addition, the above mentioned terrain difference can also have an effect. These tropospheric signal impacts can be split into a wet, liquid and dry component (Hanssen, 2002; Jehle et al., 2004; Balaji, 2011).

$$\Psi_{\text{tropospheric delay}} = \Psi_{\text{wet}} + \Psi_{\text{liq}} + \Psi_{\text{dry}} \quad (2.5)$$

Where Ψ_{dry} stands primarily for the dry gases in the troposphere, and can be accurately modelled by integrating pressure and temperature (Xu et al., 2011). In addition, the dry part is often smaller in magnitude and is more evenly distributed through the interferometric image. The liquid component (Ψ_{liq}) is referring to clouds and water droplets, but in the context of path delay estimation, the liquid component can be almost neglected (Li et al., 2003; Li et al., 2006; Jehle et al., 2008). Even though that the paper of Sarti et al. (1999) claims that a cumulonimbus clouds formation might lead up to three fringes. In general, the wet component (Ψ_{wet}) makes it more challenging to provide a correct and precise moisture field model, due to its high temporal and spatial (vertical and lateral) variability (Doin et al., 2009; Xu et al., 2011). Large amount of water vapour can compromise the effectiveness of SAR Interferometry for both the measurement of topography and surface determination from space (Zebker et al., 1997).

The models of Hopfield (1969) and Saastamoinen (1973) provided a model that accounts for the standard atmosphere respectively the wet troposphere. In this thesis, the model of Saastamoinen (1973) was implemented and subsequently refined to calculate the wet delay, which basically is fed by a function of zenith angle, atmospheric pressure, humidity (partial pressure of water vapour) and temperature (ESA Galileo Tropospheric Correction Model). Essen and Froome (1951) showed the refractivity constant, that is used in the Saastamoinen model (Janssen et al., 2004). In addition, Hanssen and Feijt (1997) used Saastamoinen's model and were able to prove the signal delay induced by the atmosphere. Regarding the modelling of the wet propagation delay, several studies has used a Global Positioning System (GPS) (Dodson et al., 1996; Williams et al., 1998; Jarlemark et al., 1998; Johansson et al., 1998; Li et al., 2003). The benefit in using the GPS technology is to calculate the water vapour very precisely at a high temporal resolution, generating a tropospheric Zenith Wet Delay (ZWD). The drawback was, that all these GPS-based methods provided a poor spatial distribution, which are solved by performing a spatial interpolation. However, all this GPS based models did not consider the terrain elevation dependency of water vapour. Especially when performing an interpolation, ignoring the topography of a mountain or volcano structure could provide a misleading result. Else, the usage of a wind model could have been implemented to see the specific water vapour congregations. For instance, the water vapour saturation on windward and leeward sides of a mountain, is most likely to differ due to the high variability of the temporally and spatially turbulent patterns at each acquisition date (Ishimaru, 1978; Wadge et al., 2002; Doin et al., 2009). The advection of air masses around mountains and volcanos could cause a considerable effect of water vapour distribution (Wadge et al., 2002).

The expectation of this thesis were that the atmospheric water vapour delays highly correlated with the elevations of the study site (Xu et al., 2011). In different literature, Goldstein (1995) demonstrated that the water vapour turbulence caused an error of 2.4 mm root-mean-square (RMS) amplitude in the Mojave Desert in California (USA). A paper of Zebker et al. (1997) claimed that in Hawaii an RMS error around 1cm of a two-pass measurement could be calculated. Therefore, a tropospheric mitigation seemed to be appropriate based on meteorological data.

2.2.2. Dependence of Ionosphere on the Sun

The ionosphere is a multi-layered medium with a starting point above 85km the Earth's surface and goes up to 1000km. The orbit of S1A is approximately 693km above the Earth's surface and therefore the ionospheric effects might not always be a major error source for causing a relevant path delay (Janssen et al., 2004).

The characteristic of the ionosphere is not static, and can change over time and space. Propagation through the ionospheric medium cannot be predicted and must be accurately calculated in some way for a compensation (Xu et al., 2004). Errors and signal delay induced by the ionosphere causing wide, large-scaled artefacts on SAR interferograms, but mostly spatially stable. Literature showed that this effect could lead up to 1.5 fringes in C-Band (Massonnet et al., 1994; Tarayre and Massonnet, 1996). Two families of ionospheric effects could be identified (Secan and Fremouw, 1988; Xu et al., 2004).

First, the ionosphere (non-turbulent) causes dispersion, group delay, phase shifts and Faraday rotation, especially in L-Band (Kim and van Zyl, 1998). The effects from Faraday rotation is widely discussed for space-borne polarimetric SAR, especially in Freeman and Saatchi (1997). These family effects depend on the electron density along the ray path and are controlled by the Total Electron Content (TEC) (Xu et al., 2004). The solar ultraviolet radiation creates the free electrons in the ionosphere. If solar winds bring high-energy electrons into the ionosphere, the electron density will increase (Balaji, 2011). The effects depend on the solar activity, the sun spot number, other solar phenomena, the time of the day, geographically, seasonally and the flight level of the satellite. As a result, a SAR acquisition will be influenced by the TEC in large scales and therefore the variability was temporally non-abrupt and homogeneous, even though the ionosphere is of inhomogeneous nature and the electron density demonstrate a large variation periodically (Xu et al., 2004).

Second, the ionospheric irregularities cause several major issues like phase perturbation, amplitude scintillation, angle of arrival fluctuation (AOA), refractive index fluctuation, and cluttering. The latter is a result of backscattering by electron density irregularities, often under conditions of geomagnetic disturbance. The scintillation is a stochastic effect, that is based on a temporal and spatial fluctuation of signals (Phase, Amplitude, Polarization and AOA) (Xu et al., 2004). The scintillation often occurs at low frequencies or low angles of the viewing geometry and play a certain role, influencing space-borne SAR systems. Basically scintillation depends on the latitude and can be split in two parts. Scintillation at low latitude is caused by the F-spread, based on the rod-sharped, magnetic field-aligned bubbles (Xu et al., 2004). These bubbles are created and remain in the F-layer of the atmosphere for about 2-3h after the sunset. The peak level of this phenomena is found at $+10^\circ$ and -10° latitude and high sun activities are positive correlated to the scintillation, also low magnetically periods give rise to more scintillation. Scintillation at high latitude is caused of the aurora, which can lead to massive distortions in interferograms. The coloured northern and southern lights are solar winds (high-energy electrons with high density) that break through the barrier of the earth's magnetic fields. The aurora phenomena are highly depended of the solar activity (Bilow, 1984; Xu et al., 2004).

These two effect groups show clearly disturbance factors like dampening, phase shift, time delay, absorption (collisions of the electrons calculated with the Appleton–Hartree expression), dispersion, polarization rotation, refraction, random fluctuations, and multipath, which have been studied over the last years to give a better understanding especially in the context of space-borne SAR systems (Budden, 1961; Yeh and Liu, 1972; Hanssen, 2002; Davies and Smith, 2002).

To correct and solve the created signal delays, there is a possibility for using the GPS network to correct such effects (Dana, 1997). Besides this, the GPS receiver networks can provide maps of the global TEC (Xu et al., 2004; Balaji, 2011). Both, the variation of the Traveling Ionospheric Disturbance (TID) which

can lead to localized artefacts and variation in TEC, cause a APD from the ionosphere (Beach and Kintner, 2001). The terms TID and TEC are linked with long-wavelength effects. For the short-wavelength effects only the TID takes its roll with some ionospheric turbulences (Afraimovich et al., 1992; Xu et al., 2004). As ionosphere behaves like a time varying, dispersive and random medium the signal delay is proportional to λ^2 . The travelling radio signals are slowed down and suffer distortion in the ionosphere compared to a vacuum, where a phase advance could result. Curlander and McDonough (1991) reported that the signal delay for C-Band based SAR system can cause up to 1.4m of path delay. In 2002 Davies and Smith (2002) have published an extended review about the ionospheric effects and issues of a ground looking SAR system in space.

At the end of this section it needed to be said, that waves propagating trough the irregular and highly variable medium suffer distortion. This lead to a performance drop in the image quality of interferograms (Xu et al., 2004). The signal delay caused by the ionospheric medium is mostly considered to be uniform over large scales, compared to the tropospheric small-scaled effects.

3. Data

In this section, information about the chosen study site and the datasets used is provided. Also a short review of the chosen satellite S1A is given with respect to its characteristics and its favourable acquisition modes.

3.1. Study Site

The study area of this thesis is located on an island in the western Indian Ocean. *Piton de la Fournaise* is a typical massive basaltic shield volcano sourced by a Hot Spot sitting on the south-eastern flank of French Island *La Réunion* ($-21.24^{\circ}\text{S} / 55.71^{\circ}\text{E}$). After a two-century long observation, it can be said that an eruption occurs every year. The volcano *Piton de la Fournaise* (2,632 m) showed in the last decades a high frequency of activity. *Piton de la Fournaise* is one of the most active volcanoes in the world with an average eruptive phase every 9 months (IPGP Observatoire volcanologique du Piton de la Fournaise). In the NW part of the island there is a deeply dissected volcano called *Piton des Neiges* which was building up the *Piton de la Fournaise*. During the last 500'000 years, the two volcanos functioned simultaneously. The eastwards slumping of *Piton de la Fournaise* formed three calderas (290'000y, 65'000y and 5'000y), covering by now 26% of the island (figure 3). The building from the very first caldera was formed by stacking thousands of meters thick lava flows, alternating with layers of slag, all intersected by a dyke system more or less interconnected (IPGP Le Piton de la Fournaise).

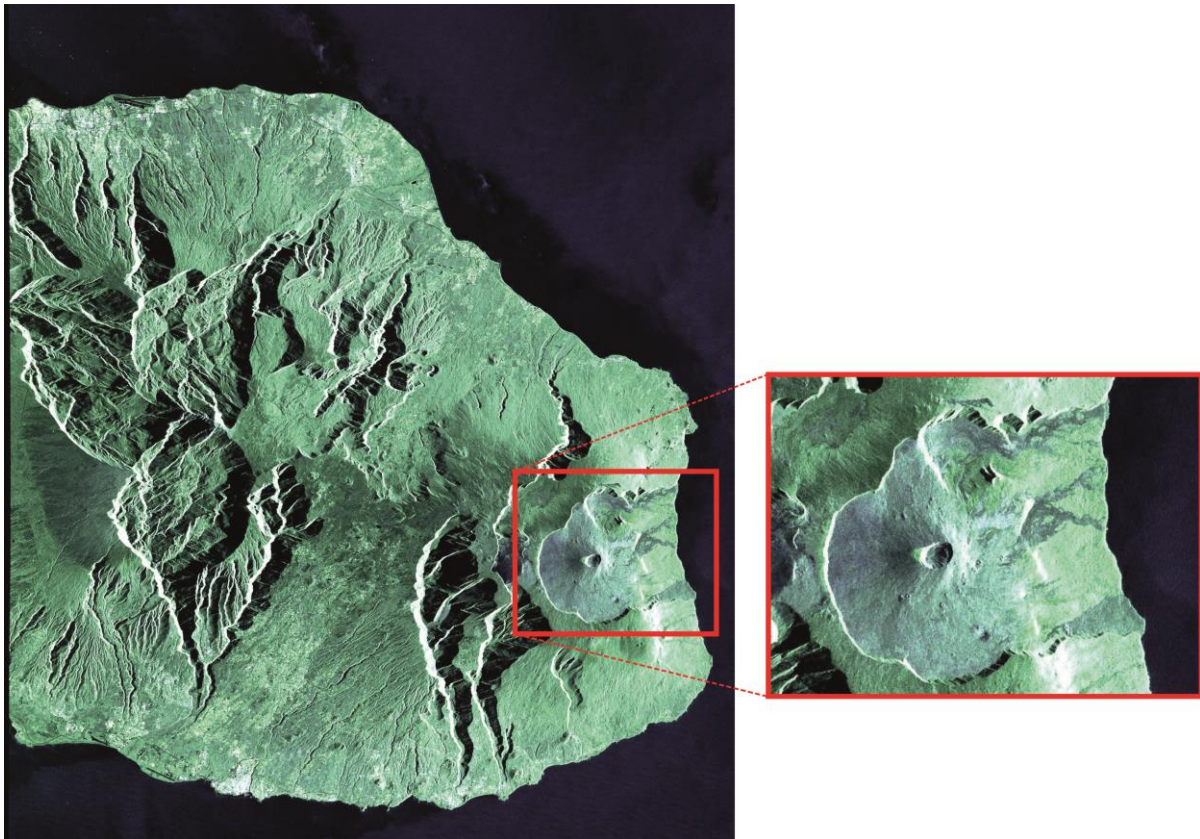


Figure 3: *La Réunion* Island via laser. S1A radar satellite test image taken on 26 May 2016, recorded and relayed to Earth by EDRS-A on 31 May 2016 (left). The study site of volcano *Piton de la Fournaise* (right) (ESA *La Réunion* Island via laser).

4500 years ago, the current terminal cone of *Piton de la Fournaise* was set up in the middle of the last caldera. At the end of the 18th century, the top was crowned by two craters, as reported by drawings of Bory crater by St. Vincent in 1804 (Bachelery et al., 2016). It appeared that the Bory and the Dolomieu basin are one big crater, but the main crater is split into two different ones. The Bory crater in the West

(light green in figure 3) and the main Dolomieu crater in the East (large depression in dark green in figure 3). The Bory crater did not change much since the early 20th century, though great changes were observed in the Dolomieu crater. The newest caldera is characterized by numerous pyroclastic cones. In addition, in the newest caldera there is a 400m high lava shield formed out of fluid lava, mainly by effusive eruptions. It is 8km wide and breached to below sea level on the eastern side. This volcano is intensively monitored by several institutions but especially by the *Institute de Physique du Globe de Paris* (Global Volcanism Program Piton de la Fournaise).

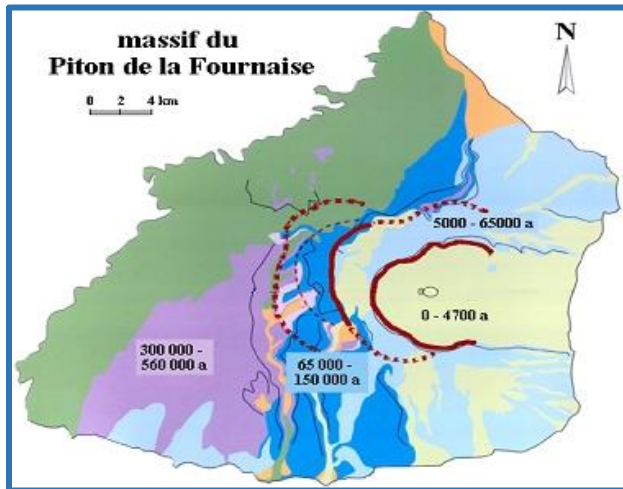


Figure 4: The three calderas are indicated in red lines on the Piton de la Fournaise. The first dotted line was reconstructed by field observations. The second could be observed at the point Pas des Sables in the volcanic area, whereas the eastern and southern extensions are estimated. (IPGP Le Piton de la Fournaise).

The activity of *Piton de la Fournaise* is monitored 24h / 7d by the volcano observatory, by several surveillances, and research networks. The climate on the island is tropical, therefore the vegetation grows strongly. During May to November the climate is rather dry and cool. The period during November to April is hot and rainy. The temperature moderates with elevation and the eastern part of the island shows a higher precipitation than the west (Mohila). The island is known for its several microclimates and its world record for the heaviest and most rainfall during a 12/72/96-hour period. On the volcano it's not a rarity to measure an annual precipitation of more than 6m (Libert). The rainy season lasts from January to March. February is by far the wettest month on the whole island. The dry season lasts from May to November. In the western part of the island the rainfall is almost zero but in the east of the island 700mm of water falls during the wettest months in the wet season.

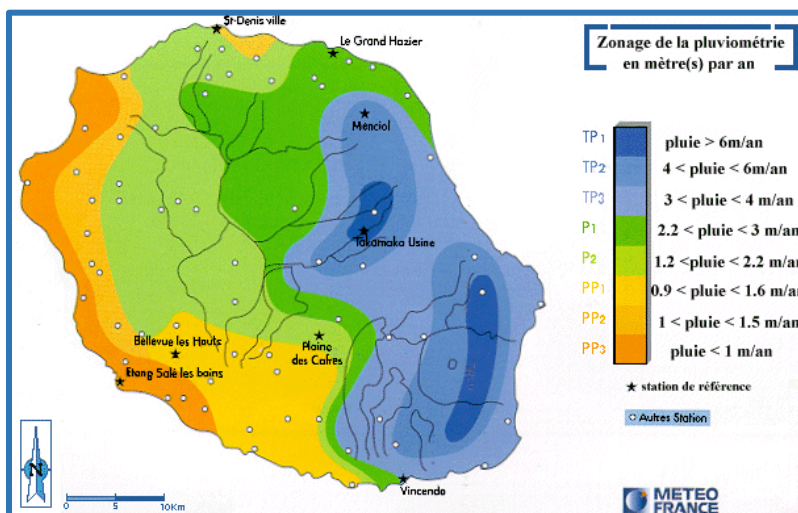


Figure 5: Precipitation zones of La Réunion (Climat et Hydrologie Etude climatique).

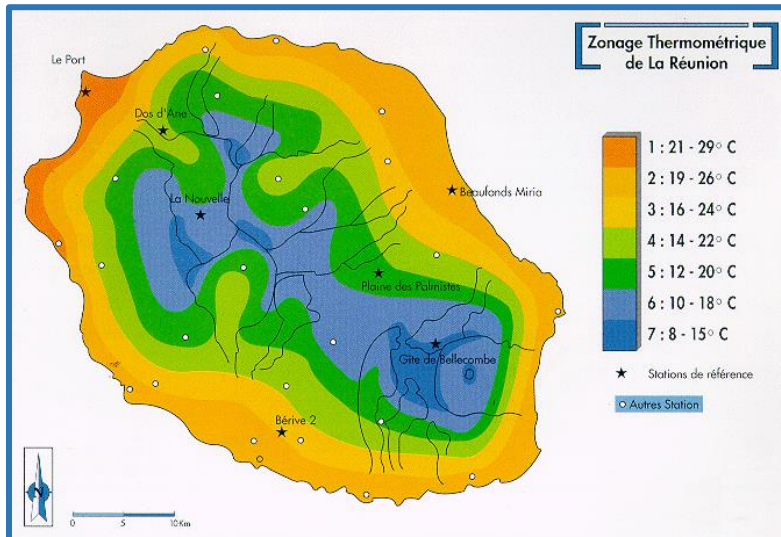


Figure 6: Temperature zones of La Réunion (Climat et Hydrologie Etude climatique).

The temperatures are quite mild on the island. An important characteristic of the temperature is, that it geographically varies on the island, due to its relief.

This study site in this thesis is suited based on its ramp of elevations, which fulfils the need of turbulent mixing in the atmosphere (Rosen et al., 1996; Ding et al., 2008). More important, it surely complied with the demand for a vertical stratification profile, varying with height (Bonforte et al., 2001; Hanssen, 2002). Also the fact that the volcanos foothills reach the Oceanside, qualified the study site, because it might lead to higher image coherence and therefore the phase unwrapping might deliver better results. The drawback of this study site was the tropical climate: heavy rain and the strong vegetation could reduce the image coherence.

3.2. Digital Elevation Model

To investigate the terrain surface of the observation area of *La Réunion* it was necessary to work with a standardised DEM of the SRTM 1-arc second with a pixel resolution of 30.8m. The SRTM mission was based on a single-pass mission and the vehicle was equipped with two antennas for collecting data of the Earth's surface in C-Band (Shuttle Radar Topography Mission 1 Arc-Second Global).

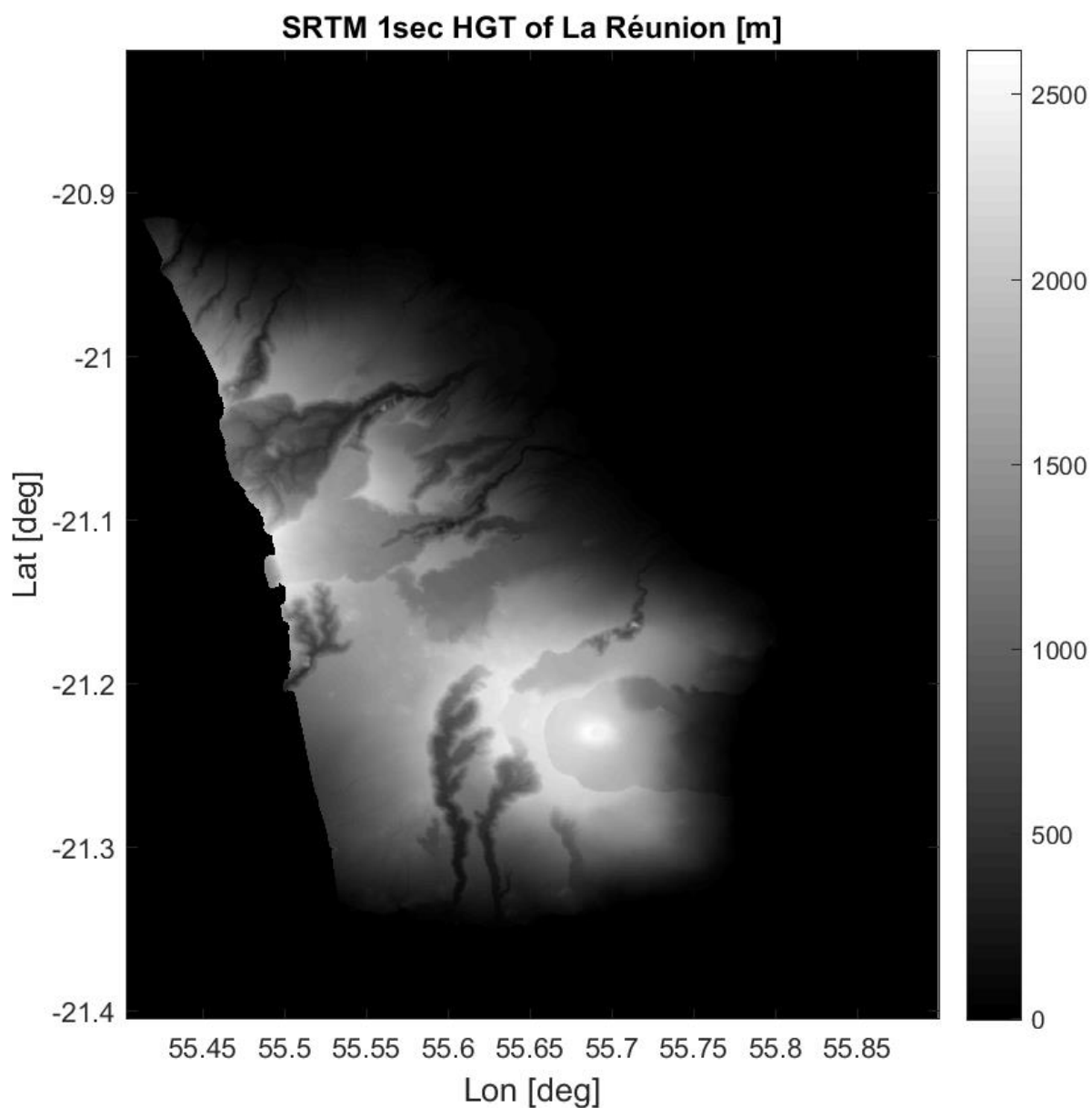


Figure 7: DEM of the eastern part of *La Réunion*, grayscale map from sea level to highest point (Shuttle Radar Topography Mission 1 Arc-Second Global).

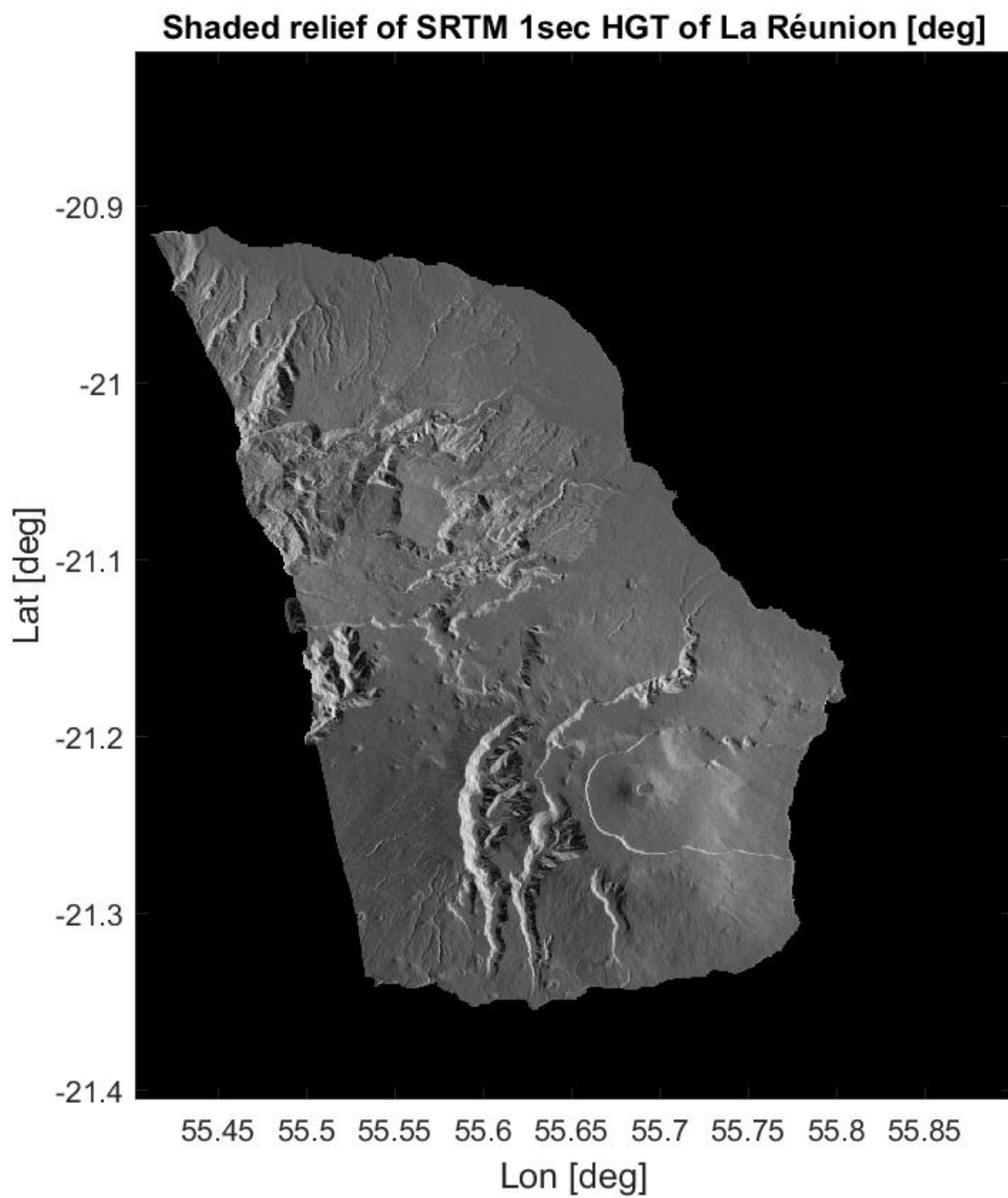


Figure 8: Shaded relief of the eastern part of La Réunion (Shuttle Radar Topography Mission 1 Arc-Second Global).

3.3. Acquisition modes of Sentinel-1A and data sets

As a new promising chapter, the launch of the satellite platform S1A is considered as a milestone regarding the possibility of an operational usage of interferometric data processing, as the Sentinel missions were explicitly designed for large-scale InSAR / DInSAR analysis (Torres et al., 2012; Ferretti et al., 2015; Lanari et al., 2015). Ground displacement can be studied and monitored by multiple applications in geophysics such as earthquake and tectonics, volcano, land subsidence and landslides (Segall, 2010; Gonzalez et al., 2015). In general, the new SAR instrument generation is defined by different acquisition modes, different spatial resolutions, coverages and band-frequencies (Sansosti et al., 2014). Especially the Sentinel constellation promises a high reliability of service and a suitable revisiting time (Elliott et al., 2008; González et al., 2015). The orbits provide a geographically decent coverage and the data dissemination after acquisition is faster than previous space-borne SAR systems, the pre-processing until the release for public use takes up to 1 hour (ESA Sentinel-1 SAR Overview). C-Band (5.405 GHz) data are continually acquired and support land and maritime monitoring and Emergency Management services such as landslide and volcano monitoring (Sakar et al., 2015; Lanari et al., 2015; Schubert et al., 2015; Costantini et al., 2016).

Table 1: Characteristics of S1A satellite (Fletcher, 2012).

Sentinel-1A satellite characteristics	
Lifetime	7 years (consumables for 12 years)
Orbit	Near-polar Sun-synchronous orbit at 693 km altitude; 12-day repeat cycle; 175 orbits per cycle
Mean local solar time	18:00 at ascending node
orbital period	98.6 min
Maximum eclipse duration	19 min
Attitude stabilisation	3-axis stabilised
Attitude accuracy	0.01° (each axis)
Instrument	Right looking with respect to the flight direction
Steering	Zero Doppler yaw steering and roll steering (−0.8° to +0.8°)
Attitude profile	Geocentric and geodetic
Orbit knowledge	10 m (each axis, 3σ) using GPS
Operative autonomy	96 h
Solar array average power	5900 W (end-of-life)
Battery capacity	324 Ah
Satellite availability	0.998
X-band downlink data rate	2 × 260 Mbit/s
Launcher	Soyuz from Kourou

The European Union COPERNICUS (formerly called Global Monitoring for Environmental Security, GMES) programme launched S1A in April 2014, a C-Band satellite with a short revisiting interval of 12 days, which was halved to 6 days by S1B (launched in late April 2016). The in-orbit commissioning phase was successfully completed in September 2014 (Salvi et al., 2012; Nagler et al., 2015; Sansosti et al., 2015), (Sakar et al., 2015). This SAR twin system gives access to more accurate data and leads to an increase of data flow (Torres et al., 2012). The data hub established by ESA provides S1A (soon followed by the S1B) data in a free and open access data policy (Sansosti et al., 2015). Also the 12 day repeat track time should imply and guarantee that ground displacement are more reliably detected, because of improving coherence (Grandin, 2015; Nagler et al., 2015; Polcari, 2016; Wen et al., 2016).

This sensor transmits recordings of the global landmasses and coastal zones on a primary operation mode featuring a wide swath of 250km with high radiometric and geometric resolution (Lanari et al., 2015). S1A delivers four pre-programmed modes. There is the Stripmap mode (SM), as a standard space-borne SAR mode. Second, the interferometric Wide swath (IW) mode is widely used and is the major acquisition mode over land for of S1A. The third mode is Extra Wide swath (EW), which provides more swaths the IW mode, at the expense of spatial resolution. The last mode is the Wave (WV) mode, which is activated when the sensor is located over open water. For this thesis only the data of SM was used on the processed level-1 as SLC data, that contains complex data of amplitude and phase (Schubert et al., 2015; Gonzalez et al., 2015; Kim et al., 2016; Wen et al., 2016).

Sentinel-1 measurement modes				
Measurement modes	Interferometric Wide-swath mode (IW)	Stripmap mode (SM)	Wave mode	Extra Wide-swath mode
Polarisation	Dual (HH+HV, VV+VH)	Dual (HH+HV, VV+VH)	Single (HH, VV)	Dual (HH+HV, VV+VH)
Access (incidence angles)	31° – 46°	20° – 47°	23° + 37°	20° – 47°
Azimuth resolution	20 m	5 m	5 m	40 m
Ground range resolution	5 m	5 m	5 m	20 m
Azimuth and range looks	Single	Single	Single	Single
Swath	250 km	80 km	Vignette 20 x 20 km	410 km
Maximum noise equivalent sigma zero (NESZ)	-22 dB	-22 dB	-22 dB	-22 dB
Radiometric stability	0.5 dB (3 σ)	0.5 dB (3 σ)	0.5 dB (3 σ)	0.5 dB (3 σ)
Radiometric accuracy	1 dB (3 σ)	1 dB (3 σ)	2 dB (3 σ)	3 dB (3 σ)
Phase error	5°	5°	5°	5°

Table 2: Overview of Sentinels-1A various measurement modes (Fletcher, 2012).

Stripmap mode

The three SAR acquisitions used in this thesis are level-1 formatted SAR data. These products are made for the users and have undergone pre-processing steps as internal calibration, Doppler centroid estimation, polynomial fitting, range and azimuth processing, and a single look complex or ground range detected focusing (ESA Sentinel-1 SAR Level-1). The level-1 SAR data is geo-referenced using altitude and orbital information of the satellite, representing in slant-range geometry. The Line Of Sight (LOS) of the radar is in slant range, which corresponds to the standard radar range coordinate. The SLC format means having a single look in each dimension corresponding to full signal bandwidth and complex information as the real and the imaginary units, preserving the important phase information. Besides this, the SM data contain one image per single swath in one polarization (VH/VV) (ESA Sentinel-1 SAR Level-1). In this thesis only VV polarization data were used and processed.

The gathered data in this thesis for the test site of *Piton de la Fournaise* was acquired by S1A in Stripmap mode. The SAR acquisitions to study the *Piton de la Fournaise* was provided by the European Space Agency. The data sets are provided as free and open-access through the Scientific Data Hub (ESA Sentinels Scientific Data Hub). In general, the Stripmap mode data are acquired for extraordinary missions, for testing reasons, for emergency management actions and operations over isolated islands. In particular, the Stripmap mode beam S6 was chosen to do the interferometric modelling. The S6 swath width is 80km; it has a spatial resolution of 5m by 5m in a single look. This mode works by illuminating the ground swath by sequential SAR pulses as the antenna beam is targeting to a fixed azimuth angle and a nearly fixed off-nadir angle. The SM provides a constant along track image quality while the incident angle shows a small variability but is approximately constant. The Stripmap mode contains six predefined elevation beams, which differ in the incident angle (ESA Sentinel-1 SAR Stripmap; Polcari, 2016). Table 3 shows the characteristics of the Stripmap mode:

Table 3: Characteristics of Sentinels-1A Stripmap mode 6 (Fletcher, 2012).

Characteristics of Sentinels-1A Stripmap mode 6	
Swath width	80 km
Range and azimuth looks	Single
Polarisation modes	Dual: HH+HV, VV+VH Single: HH, VV
Maximum Noise Equivalent Sigma Zero (NESZ)	-22 dB
Radiometric stability	0.5 dB
Radiometric accuracy	1 dB
Phase error	5°
Incidence angle range	18.3° - 46.8°
Elevation beams	S1 to S6
Specific incidence angle at orbit altitude for S6	40.79° - 46.73°
Specific off-nadir angle at orbit altitude for S6	35.98° - 41.01°

Orbit Files

The knowledge of the platform position and its accurate Orbital State Vectors (OSVs) is important for the geolocation of the imaging system. The OSVs were already included in the S6 products, also including the precise “S1A_OPER_AUX_POEORB” and restituted “S1A_OPER_AUX_RESORB” orbit files. The Global Navigation Satellite System (GNSS) receiver on-board the Sentinel satellites provide these orbit data. Using the precise data revealed a slant range offset of 1.27 ± 0.06 m and an azimuth offset of 1.96 ± 0.41 m (Schubert et al., 2015). To find the best-suited geolocation accuracy, it is endorsed that precise orbit files to be used. If this will not work properly, the restituted orbit files are the second best choice regarding the accuracy (Schubert et al., 2015). These orbit data showed a high geolocation accuracy. Therefore, there was no need to using Ground Control Points (GCP) for the coregistration of repeat-pass SLCs. Especially in a volcanic region where the surface is permanently changing due to volcanic eruption, the GCP cannot be placed or is too dangerous.

Data evaluation

The following figures 9-12 show the evaluation process of the S6 data covering the study site. The data were gathered from the above mentioned Data Hub (ESA Sentinels Scientific Data Hub). Three criteria were defined to select the desired S6 pairs. First, the time period was set from July 2015 to June 2016 based on the volcanic activity. The period revealed 14 SLC products in S6. From there, the second criterion was applied, based on the time window of the volcanos eruption. As the focus of this thesis lied on the estimation of APD and correction of DInSAR measurements, there was a need to evaluate a data pairs with no surface displacement. A relatively stable volcano enables to study the atmospheric artefacts isolated from ground movements (IPGP Bulletin les dernières actualités de l'observatoire; Interactive Map of Active Volcanoes and recent Earthquakes world-wide). The third criterion was the availability of high resolution meteorological daily data of ERA-Interim from the European Centre for Medium-Range Weather Forecasts (ECMWF) (ERA-Interim Daily).

Based on these three criteria the evaluation was performed. The figures 9-12 distinguish into different technical aspects, the temporal and spatial baseline of the pairs. The height ambiguity and the modelled coherence of the 14 s6 acquisitions were also included. This overview provided a good foundation for decision-making; SLC pair the focus should lie on. Two blue boxes define the optimal period. This was chosen based on the availability of meteorological data and no surface displacement occurring contemporaneously.

3.4. Meteorological data of ERA-Interim

The high resolution meteorological data was retrieved from the ECMWF, which is an independent intergovernmental organisation (ECMWF Landingpage). ECMWF disseminates numerical meteorological predictions in micro-scale resolution. The here chosen datasets of meteorological data were from ERA-Interim Daily, that could be accessed through (ERA-Interim Daily) and were free of charge. The global atmospheric modelled meteorological data from ERA-Interim stands for a global atmospheric reanalysis beginning in 1979 and are continuously updated. The interim modelling takes about three months before releasing the next monthly data set to the public. Studies from (Doin et al., 2009) and (Uppala et al., 2005) have also used data from ECMWF to retrieve atmospheric modelled meteorological data. For verification reasons the NOAA meteorological data (National Centers for Environmental Information (NCEI)) and data of a ground weather station (table 4) on *La Réunion* (Historical Weather St. Denis Gillot) were studied. ERA-Interim and meteorological data from the above mentioned sources proofed a credible correlation.

Table 4: Weather station at the Airport of La Réunion (Historical Weather St. Denis Gillot).

Meteorological Station St. Denis Gillot (La Réunion)	
Name	ST DENIS GILLOT (REUNION)
Network : ID	GHCND : REM00061980
Latitude/Longitude	-20.887°, 55.51°
Elevation	20.1 m
Region Name	AFRICA
Country Area	OCEAN ISLANDS / ILES DANS L'OCEAN

To estimate the dry and wet components of the APD, it was necessary to obtain the following meteorological data sets from ERA-Interim server in vertical profiles. It seems assumably that the listed data is extracted as a vertical profile, representing the average stratification above the SAR scene (Doin et al., 2009). The following parameter were extracted and implemented into the APD model of RSL:

- 2 metre dew point temperature (to calculate the relative humidity)
- Total water vapour column
- 2 metre temperature
- Total cloud cover
- Surface pressure

The requested data from the ECMWF server was retrieved in NetCDF format. The user can choose from 4 steps per day (6,12,18 and 24h), also to adjust the desired attributes as the Area (N, W, S and E) and the spatial resolution (smallest is approximately 13.821km², which is equal to 1.125°) can be individually adjusted. For every date of acquisition of the 14 SLCs, ERA-Interim data were downloaded and fully processed for the APD estimation.

Figure 13 shows the raster points of the retrieved ERA-Interim raster file. These nine points contain the above mentioned parameters and were evaluated and arithmetically averaged to span the modelled meteorological data over the area of interest. Concerning the provided coarse grid of the ERA-Interim daily data, further calculation could have been made to improve the meteorological resolution by interpolating the temperature/pressure/water vapour on the resolution of the DEM (30.8m) and its elevations in a laps rate procedure. Hence, meteorological data at the foothill of the volcano could have been calculated, instead of an arithmetically averaging, over the scene, but the mathematical approach in this thesis was different as chapter 4.2 shows.

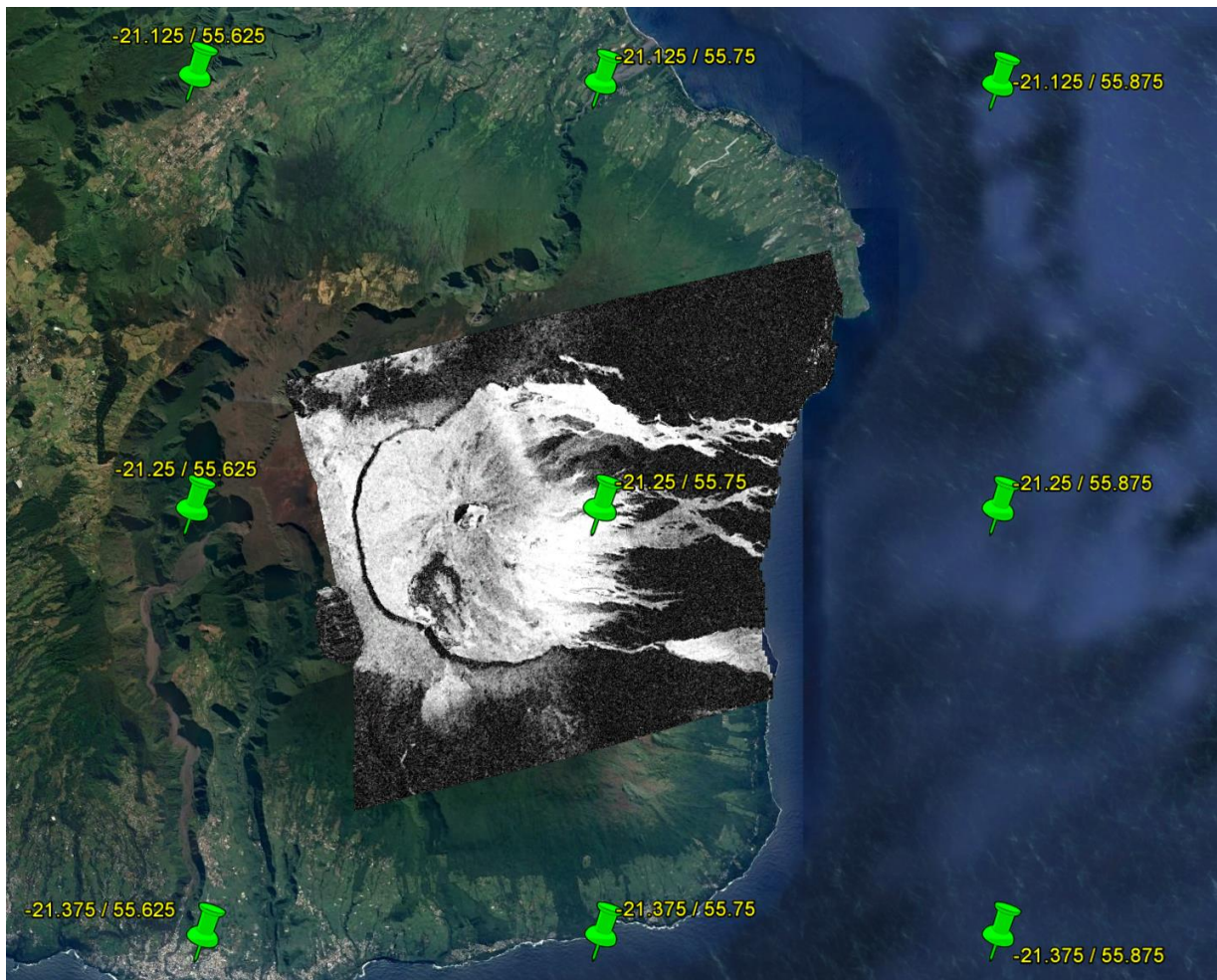


Figure 13: This represents the raster of the retrieved ERA-Interim modelled meteorological data overlaid on a coherence map, own representation based on Google Earth imagery.

Figure 13 includes also a coherence map for demonstration purposes, to see which part of *La Réunion* was analysed using the repeat-pass S1A data. An elevation histogram (figure 14) was generated to see the distribution of heights represented in the volcanic study site of SAR acquisitions.

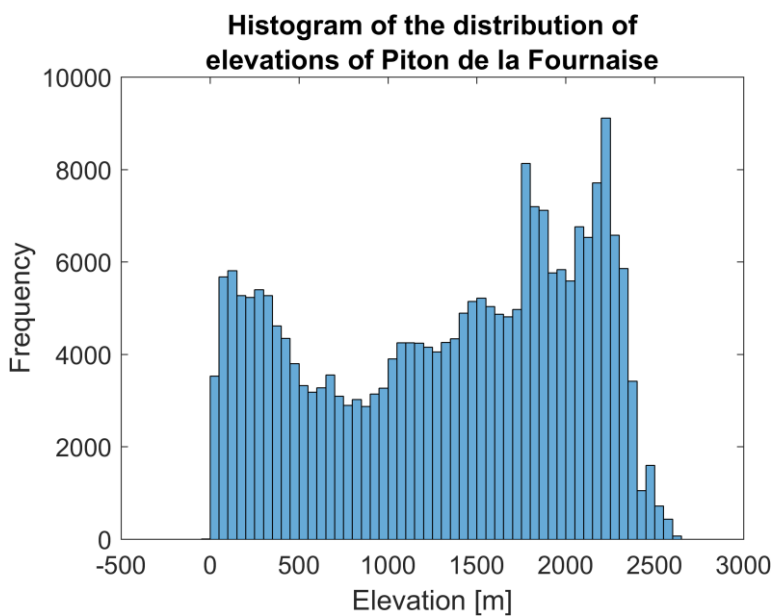


Figure 14: Histogram about the elevation of the volcanic area, corresponding to figure 13, own representation.

Stack Overview		PD Difference of means [m]															
06. Jun 16	Y	Y															0
25. Mai 16	Y	n															0.229
19. Apr 16	Y	n															0.106
07. Apr 16	Y	n															-0.062
02. Mrz 16	Y	n															-0.678
19. Feb 16	Y	n															-0.325
14. Jan 16	Y	n															-0.575
27. Nov 15	Y	n															-0.634
15. Nov 15	Y	n															-0.738
10. Okt 15	Y	Y															0.058
28. Sep 15	Y	Y															-0.089
23. Aug 15	Y	Y															0.223
11. Aug 15	Y	Y															0.105
06. Jul 15	Y	Y															0.209
SLC S6 Dates																	
	Y	Y	06. Jul 15	11. Aug 15	23. Aug 15	28. Sep 15	10. Okt 15	15. Nov 15	27. Nov 15	14. Jan 16	19. Feb 16	02. Mrz 16	07. Apr 16	19. Apr 16	25. Mai 16	06. Jun 16	
	Y	Eruption	Y	Y	Y	Y	Y	n	Y	Y	n	Y	n	Y	n	Y	

Figure 15: Characteristic of the SLCs based on the modelled total APD difference. This is the total mean difference of ionospheric and tropospheric path delay, own representation.

The output in figure 15 is the total difference of mean path delay over the volcanic area. The goal was to find a high APD difference of two S6 dates, under the condition that the values were inside the two blue boxes. The data set showed that, two Pairs could be interesting to perform atmospheric correction on DInSAR measurements.

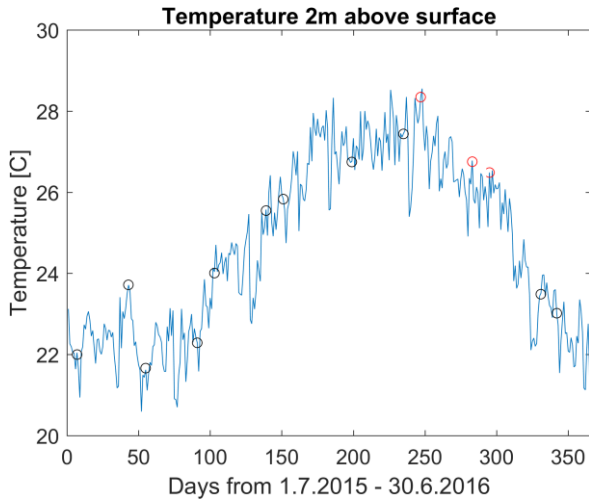


Figure 16: Temperature data of ERA-Interim from July 2015 to June 2016

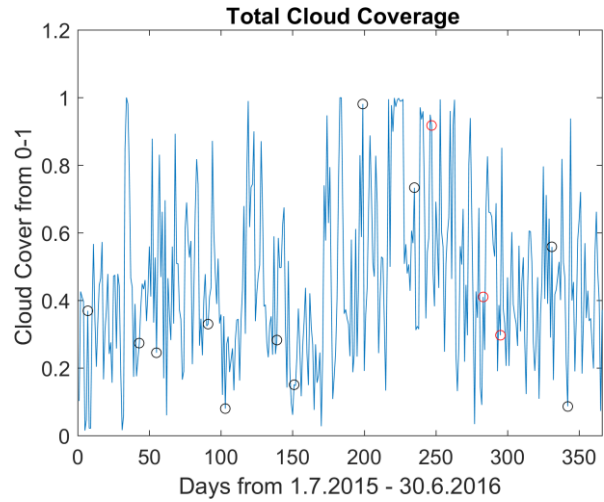


Figure 17: The total cloud coverage data of ERA-Interim from July 2015 to June 2016

The overview of the annual variation of the modelled meteorological data of ERA-Interim revealed the results shown in figures 16-20. The larger the variations were, the larger the expected signal delay by the atmospheric interaction. Red circles indicate the chosen SLC combination of 02. March 2016 / 07. April 2016 (pair One) and 02. March 2016 / 19. April 2016 (pair Two). Through the next chapter the combination of 02.03.2016 & 07.04.2016 is named as “pair One” and the combination of 02.03.2016 & 19.04.2016 is named as “pair Two”. Be aware that there might be other options with an even larger variation, always with a larger temporal baseline which reduces the coherence of the imagery. In this case, the decisions to find the right pair(s) was based on several trade-offs.

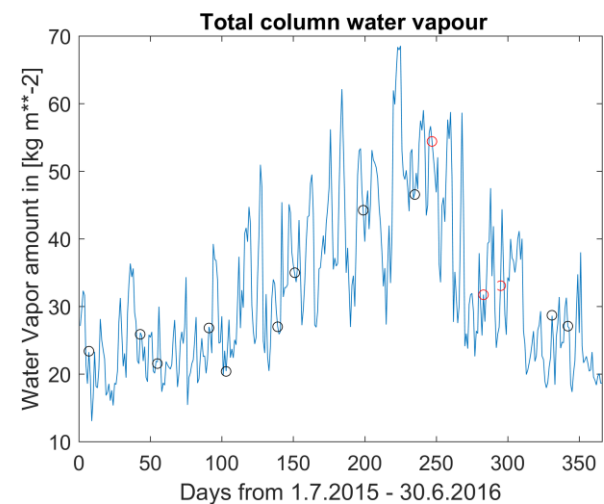


Figure 18: Dew point temperature data of ERA-Interim from July 2015 to June 2016.

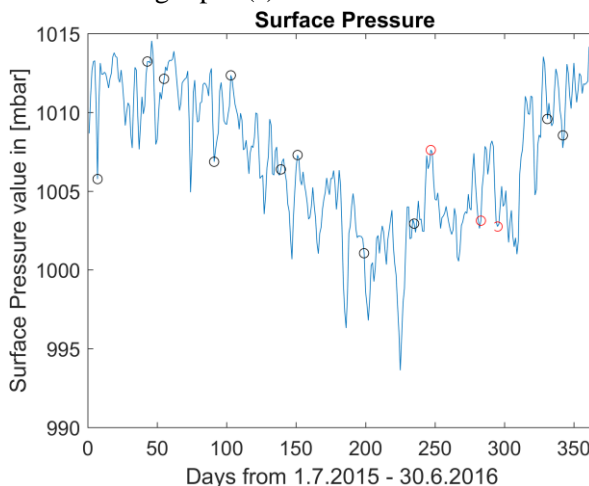


Figure 19: Surface pressure data of ERA-Interim from July 2015 to June 2016

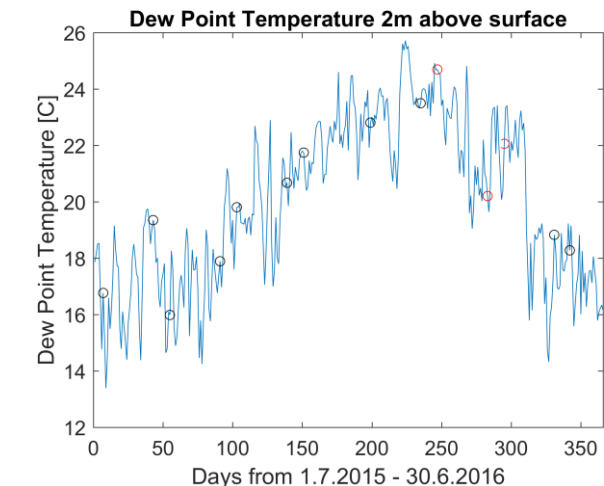


Figure 20: Dew point temperature data of ERA-Interim from July 2015 to June 2016.

Selected Stripmap data sets

In figure 15 the estimated total APD differences are shown also the appropriate pairs were selected, showing one of the highest total APD difference. The figures 9-12 were also strongly considered to find the adequate datasets to answer the mentioned research questions. The temporal baseline of 36 days / 48 days and the spatial baseline of 69.45m / 39.85m with a high coherence value were suitably for a DInSAR procedure. It is important to see that in figure 15 the volcano showed no eruption; therefore, almost none surface displacement was expected. The exact product specification is presented in tables 5-7 for the selected SAR S6 product. This following overview with the corresponding swath, provided a short insight into the product annotation.

Table 5: Product information of the 02.03.2016 SLC, own representation.

SLC of 02. March 2016	
File name	S1A_S6_SLC__1SDV_20160302T145244_20160302T145307_010191_00F0AD_D28E
Instrument mode	SM
Instrument swath	S6
Relative orbit	144
Orbit number	10191
Sensing start:	2016-03-02T14:52:44.088Z
Sensing stop	2016-03-02T14:53:07.855Z
Polarization	VV + VH: only VV chosen
Pass direction	Ascending
Satellite	Sentinel-1A
Instrument	SAR-C
Acquisition type	Nominal
Product class description	SAR Standard L1 Product

Table 6: Product information of the 07.04.2016 SLC, own representation.

SLC of 07. April 2016	
File name	S1A_S6_SLC__1SDV_20160407T145244_20160407T145308_010716_00FFC7_A6F9
Instrument mode	SM
Instrument swath	S6
Relative orbit	144
Orbit number	10716
Sensing start:	2016-04-07T14:52:44.909Z
Sensing stop	2016-04-07T14:53:08.690Z
Polarization	VV + VH: only VV chosen
Pass direction	Ascending
Satellite	Sentinel-1A
Instrument	SAR-C
Acquisition type	Nominal
Product class description	SAR Standard L1 Product

Table 7: Product information of the 19.04.2016 SLC, own representation.

SLC of 19. April 2016	
File name	S1A_S6_SLC__1SDV_20160419T145245_20160419T145309_010891_01050B_A397
Instrument mode	SM
Instrument swath	S6
Relative orbit	144
Orbit number	10891
Sensing start:	2016-04-19T14:52:45.423Z
Sensing stop	2016-04-19T14:53:09.182Z
Polarization	VV + VH: only VV chosen
Pass direction	Ascending
Satellite	Sentinel-1A
Instrument	SAR-C
Acquisition type	Nominal
Product class description	SAR Standard L1 Product

4. Methodology

In this chapter, the sequence of the processing steps is outlined. The methodology gave an insights into the several processing tasks with different software. The given workflow diagram (figure 21) showed the necessary steps, to perform an interferometric approach with S6 data, to estimate the path delay by reference to meteorological ERA-Interim daily data and the final steps, estimating the APD and mitigate the interferometric data set.

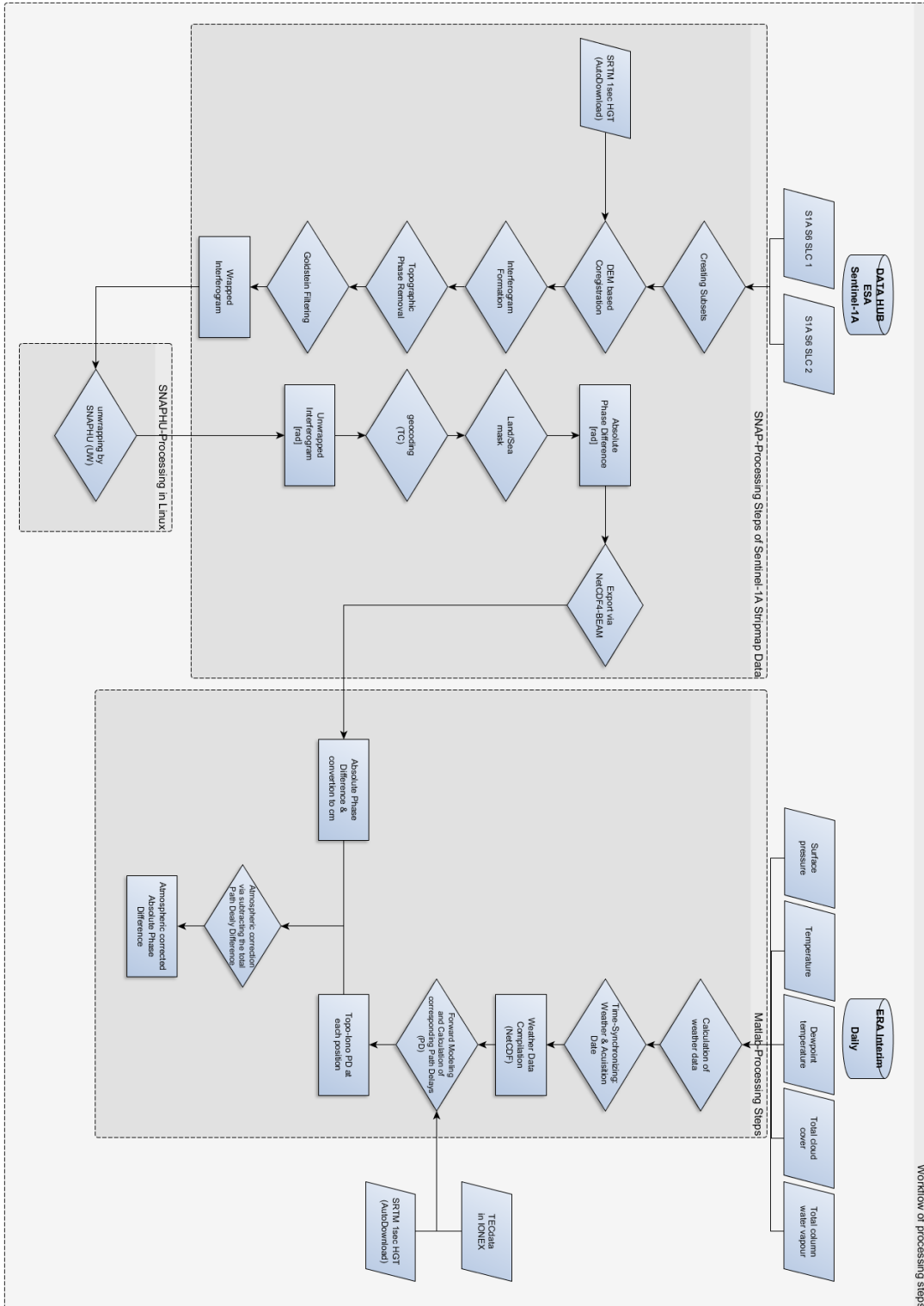


Figure 21: Workflow diagram of the processing steps for SLC data from S1A in S6. In addition, the processing of the meteorological data set. Boxes were made based on the used software, own representation.

4.1. SAR data processing

After selecting the suitable level-1 SAR S6 data from the Scientific Data Hub, it is time to process the data (ESA Sentinels Scientific Data Hub; Fletcher, 2012). The gathered SLC sets were processed with ESAs Sentinel Toolbox the Sentinel Application Platform (SNAP). The SNAP software is made for Earth Observation processing and analysis (SNAP STEP). The Workflow diagram showed the different processing steps, that is outlined further more in this coming section. Starting with the coregistration to create an interferogram, followed by filtering, unwrapping and orthorectification.

General Coregistration

This coregistration processing chain was working with the given orbit state vectors. The interferometric coregistration was performed by stacking, fine cross-correlation and resampling. The “create stack” operator collocates both S6 acquisitions (master and slave) and placed them in a reference geometry, making to make the corresponding pixel pairs congruent by an affine transformation equation. For geometric calculation, orbital data could be used or GCP. Further a fine sub-pixel coregistration was performed which is an essential step for an accurate determination of phase difference and interferometric displacement analysis. The chosen coregistration procedure relied on the fine cross-correlation technique, which was time consuming but increased the accuracy by the sub-pixel alignment. The offsets between master and slave SLCs were calculated by maximizing the cross-correlation. After the coregistration-offsets were computed, the estimation of the Coregistration Polynomial (CPM) were computed by the warp operator, that resampled pixels of the slave image into pixels in the master image. Inaccurate Coregistration increased the variance of the interferometric phase and thus gave raise for decorrelation (Meier, 2013). Factors such as the baseline-decorrelation, errors in coregistration process, temporal variation of the object, not precise orbit files and system noise could contribute to phase anomalies (Zebker and Villasenor, 1992; Woodhouse, 2005).

Interferogram Formation

This processing step was about computing a complex interferogram with subtraction of the flat-earth phase, using a two-dimensional (2D)-polynomial, based on the orbital information and metadata of the S6 data. An interferogram was formed by cross multiplying the master image with the complex conjugate of the slave, where the amplitude of both SLC was multiplied while the phase showed the actual phase difference out of a subtraction of the two acquisitions. Where the phase variation is proportional to difference of the target distance divided by the transmitted and operating wavelength λ (Woodhouse, 2005; Ferretti et al., 2007).

$$\phi_1 = \frac{4\pi R}{\lambda} \quad (4.1)$$

$$\phi_2 = \frac{4\pi(R + \Delta R)}{\lambda} \quad (4.2)$$

$$\Delta\phi = \phi_2 - \phi_1 = \frac{4\pi\Delta R}{\lambda} \quad (4.3)$$

Where ϕ is the actual phase of each SLC product and R is the satellite target distance which varies depending of the orbit. Creating an interferogram is complex. In an interferogram, the interferometric phase is visualized by a color-coded phase area, the so-called “Fringes”. A phase shift of a particular wavelength corresponds to the passage of a rainbow colour spectrum (figure 22) (Curlander and McDonough, 1991; Dzurisin, 2007).

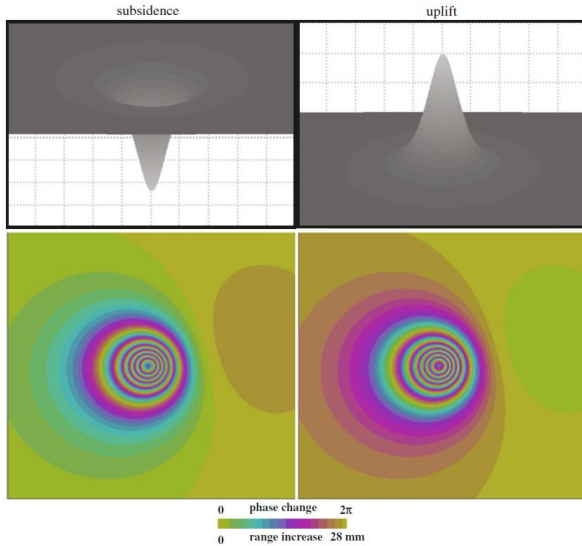


Figure 22: A simplified visualization of a sinking or rising surface modification can be interpreted using InSAR/DInSAR. Important are the sequences of colors (yellow, red, pink, blue, green and yellow again), which correspond to a C-Band (SIA/B/C/D, ENVISAT, ERS, RADARSAT-1, etc.) measurements of a 28 mm (wavelength by two) LOS change. Depending on the direction of movement, the gradient is in the opposite color scheme, (Dzurisin, 2007: 13).

The interferometric phase difference of the two SAR acquisition ($\Delta\phi$) can be interpreted like this (Sheng. et al., 2012):

$$\Delta\phi = \varphi_{Mov} + \varphi_{Atmos} + \varphi_{Topo} + \varphi_{flat} + \varphi_{noise} \quad (\text{Sheng et al., 2012: 228}) \quad (4.4)$$

where φ_{Mov} is the distance offset between the sensor and the object, which is also the surface displacement, φ_{Atmos} is the phase delay of the signal due to atmospheric effects, φ_{Topo} is the topographic distortion factor based on the different angles of the repeated overflights, φ_{flat} is called the flat-earth phase that is the phase contribution due to the Earth’s curvature (ellipsoid) and φ_{noise} is the phase noise, which describes the quality of the interferometric phase signal (temporal change of scatters, different looking angle and volume scattering) (Ferretti et al., 2007; Meier, 2013). The interferometric processing, tried to eliminate other sources of error to be left with only the contributor of interest that were typically the elevation or the displacement.

In this processing step, the interferogram formation was computed. The contribution of φ_{flat} could be directly eliminated by SNAP. Actually the flat-earth phase was the present phase in the interferometric signal due to the curvature of the reference surface. The geometric reference system of the reference surface was defined by the reference system of satellite orbits, in this case WGS84, this was also the reference system used by all space-borne SAR systems. The calculation of the flat-earth was commonly performed in a number of points distributed over the SLC. Hereby the complex interferogram was smoothed by subtracting the 2D-polynomial output (Gupta, 2013).

The interferometric fringes are representing in a full 2π cycle in radians and appear as cycles of arbitrary colours, with each cycle representing half the sensor’s wavelength (figure 22). Relative ground movement between two points were calculated by counting the fringes and multiplying by half of the wavelength. Thus led to phase shifts. Due to the high error rate and the ambiguity of the phase differences, a single interferogram was not sufficient for interpreting a surface displacement. The colour sequence revealed whether the displacement led to a subsidence or an elevation of the terrain (figure 22) (Li and Goldstein, 1990; Ferretti et al., 2007).

A second output in this processing step was the coherence image, that gave important information about the similarities of master and slave SLC. And as mentioned before, a loss of coherence could lead to poor interferometric results.

Topo-Removal: DInSAR 2-pass method (2 SLCs & DEM)

DInSAR is popular in the fields of geophysics, volcanology and glaciology (Franceschetti and Lanari, 1999; Woodhouse, 2005). Results lead to a cm and mm range of vertical and horizontal surface changes (Puységur et al., 2007). This is one of the most effective earth observation techniques (Lanari, 2015). This technique requires a small perpendicular baseline (close flight tracks, close orbits) in addition a high consistency of coherence (Gabriel et al., 1989). Basically, the method of DInSAR was calculated in this thesis by the 2-pass method (2 SLCs and DEM) (Dzurisin, 2007). After creating a complex interferogram in the step before, the SRTM 1 arc sec DEM in HGT tiles was subtracted from the complex interferogram pixel by pixel (Sansosti et al., 2015; Polcari, 2016). This method is in practice most frequently applied (Ferretti et al., 2007; Dzurisin, 2007). Since the synthetic interferogram are based on a DEM, the height (h_a) of fringes can be calculated by the following equation.

$$h_a = \frac{H\lambda \tan \theta}{2b} \quad (\text{Dzurisin, 2007: 172}) \quad (4.5)$$

H is the altitude of the satellite, λ the wavelength of the operating sensor, the incident angle θ and b the length of the perpendicular baseline (Ferretti et al., 2007; Dzurisin, 2007). By consulting this method, the formula (4.4) of the interferogram had changed as the topographic phase of the DEM was removed. It can also be said that the interferograms were smoothed by a undesirable phase trend of the topography (Gupta, 2013). This results in a topographical residual, which can be set to 0 ($\varphi_{Topo} = 0$) (Zebker and Rosen, 1994; Rosen et al., 1996):

$$\Delta\varphi_{DInSAR} = \varphi_{Mov} + \varphi_{Atmos} + \varphi_{noise} \quad (\text{Sheng et al., 2012: 228}) \quad (4.6)$$

As a result, the interferogram only contained surface movement, atmospheric influence and noise. As mentioned earlier, isolating motions from the propagation through the atmosphere is a difficult task, because the atmosphere can induce additional phase shifts, especially with a repeat-pass system (Rosen et al., 1996; Bamler and Philipp Hartl, 1998; Lanari, 2015). The output of this step was a reference phase of the DEM and a topographic corrected interferogram. Optional there are two advanced methods of this DInSAR technique: First the Permanent persistent scattered InSAR (PSInSAR) method (Ferretti et al., 2001; Ferretti et al., 2007) and second, the small baseline (SB) approach (Berardino et al., 2002; Mora et al., 2003; Lanari et al., 2004). Even though these advanced methods were often used in literature, but this thesis is only driven by the basic DInSAR approach, because the data of S1A in combination with the PSInSAR and SB methods were not yet ready to be processed in an ordinary way through SNAP in combination with Stanford Method for Persistent Scatterers (StaMPS) (Ferretti et al., 2007; Hooper et al., 2012; Sansosti et al., 2015).

Interferogram Filtering (Goldstein)

In general, there was a lot of noise in the processed interferogram, this could be triggered by the system temperature, the inaccurate matching, overlays, orbit errors etc. Therefore this next step was necessary to eliminate or reduce the encountered noise. The phase filtering technique reduced the residues and improved the phase unwrapping accuracy. The used method in this thesis was a nonlinear adaptive algorithm by Goldstein and Werner (1998). The used vector filtering reduced the noise in the interferogram. The filtering was important for the following phase unwrapping; therefore, the filter was combined with the current coherence of each pair to get a faster phase unwrapping. This vector filtering has the advantage to deliver high precision and fast results (Qing et al., 2004; Ferretti et al., 2007).

Phase unwrapping

The phase unwrapping is an important processing step, resulting in unwrapped phase values in radians. This crucial step belonged to the most difficult process in the entire processing chain. The unwrapping is a field of intense research for decades. There is no perfect algorithm. Thus the wrapped phase provides less information than the unwrapped phase. Therefore the phase field was interpolated and some additional assumption must be made (Chen and Zebker, 2001). For the unwrapping procedure in this thesis, a 3rd party software by Chen and Zebker (2001) was used called Statistical-Cost, Network-Flow Algorithm for Phase Unwrapping (SNAPHU). To do so the Minimum Cost Flow (MCF) algorithm of (Costantini, 1998) was applied for phase unwrapping (Polcari, 2016). Results of the unwrapped products depended on the estimated coherence of the used data set. The better the coherence, the better the reliability and quality of the output of unwrapping. As interferometry is a relative technique, for example it represents the difference between pixels, rather than showing absolute values. Therefore, the unwrapped results should also be considered as a relative value.

The two-dimensional relative phase signal is a 2π modulus of the absolute phase signal, which can be accessed by phase unwrapping. On one hand, setting the wrapping interval to $[-\pi, \pi]$ is trivial and straightforward, on the other hand, the phase signal is non-linear and non-uniqueness, this challenges the application of SAR interferometry. Also noise, layover effects and foreshortening effects caused massive troubles when unwrapping the signal and did not deliver an adequate result as desired. There are many different processing algorithms that Ghiglia and Pritt (1998) and Chen and Zebker (2001) presented in detail. The most popular processing methods are a part of the path-dependent (path-following) algorithm and secondly the Gaussian least squares method (least square) (Ghiglia and Pritt, 1998).

Terrain correction orthorectification

The data was until that point still in the viewing geometry of the original satellite ground range view. Distances needed to be corrected due to topographical variations or the tilting of the satellite. Especially on S6 acquisition, the image data is off-nadir. The advantage of terrain corrected data allows geometric overlays of data from different satellites (Small and Schubert, 2008). To geocode SAR data from single 2D raster SAR geometry, Small and Schubert (2008) proposed the Range Doppler orthorectification method. This method uses the orbit state vector metadata, SAR timing annotation, parameter of the slant to ground range conversion and a reference DEM (here: SRTM 1 arc sec HGT, which was compatible with the WGS84 and showed a square pixel resolution of 30.8m) to calculate the geolocation information. The pixels spacing of the S6 data were changed, for fitting the DEM.

Masking: Land Mask

To simplify the data, a masking step was performed, turning pixel in the ocean into no data values, while preserving the land pixels. Practically, a DEM was simulated to determine if the pixels were either land or water. After this task the processed data was exported from SNAP into Matlab on the base of a NetCDF4-BEAM format.

4.2. Meteorological data processing

In Literature there are several different methods to calculate the atmospheric delay signal. As mentioned above, the APD was described as the sum of the dry and wet components as well as frequency dependent delay caused by the ionosphere (Jehle et al., 2008). As this atmospheric model is dependent on elevations, it uses a vertical model, providing a zenithal path delay for a given point on the Earth's surface. Therefore, a conversion to a certain slant range viewing angle was needed to obtain the distance of the viewing geometry, i.e. the radar timing delay. The model was neglecting the local incident angle of the topography, because the Earth's surface did not affect the signal path delay (Jehle et al., 2008). Basically the calculation was performed with the nominal (ellipsoidal) incident angle θ_i which is only approximately correct, because the model was set to terrain surface mode and not to ellipsoid mode.

Ionospheric signal delay estimation

The ionospheric effects of space-borne SAR systems were mostly observed in high latitude regions, supplemented with the aurora phenomena. The ionospheric effects have a bigger impact in L-Band than in C-Band, and the X-Band minor effects than C-Band (Jehle et al., 2008; Doin et al., 2009; Mattar and Gray, 2014). The ionosphere is also divided in layers such as D, E, F1, and F2; each interacts differently with electromagnetic waves (Jehle et al., 2004; Schubert and Small, 2016).

The calculation of the ionospheric delay was calculated by the TEC values. Using the GPS information, a global ionospheric TEC map was created and a practical scintillation mode was used, estimating the diurnally phase correction values (Balaji, 2011; Schubert and Small, 2016). The TEC is proportional to the zenith ionospheric range error, for instance for a space-borne SAR system in C-Band, a TEC of $1 * 10^{16} m^2 = \text{phase shift of } 0.5 \text{ cycle}$ (Ding et al., 2008). The University of Zurich used the estimation provided in the IONEX format from the Centre for Orbit Determination Europe (CODE), where the Global Ionospheric Maps (GIMs) were daily generated (Jehle et al., 2008; Balaji, 2011; Schubert and Small, 2016). Together with the exact satellite position and target area, the LOS calculation of a two-way ionospheric delay was calculated by the following formula (Jehle et al., 2008):

$$\Psi_{iono} = K * \frac{TEC}{f_c^2} * \frac{1}{\cos(\theta_i)} \quad (4.7)$$

Where K is the refractive constant of $40.3 \left[\frac{m^3}{s^2} \right]$, f_c the SAR centre frequency [Hz], TEC the vertical TEC [$TECU * 10^{16}$] and the θ_i is the nominal (ellipsoidal) incident angle at a given position in the interferogram that was multiplied by cos for a specific incident angle (Jehle et al., 2008; Balaji, 2011; Schubert and Small, 2016).

Tropospheric signal delay estimation

In this thesis a modulated and straightforward height-dependent model was used, since the delay caused by the troposphere is most sensitive to altitude (Jehle et al., 2008; Schubert and Small, 2016). Ground-based meteorological measurements from atmospheric pressure, humidity (water vapour), and temperature were needed to calculate the tropospheric signal delay for generating a tropospheric path delay estimation (Jehle et al., 2008). The hydrostatic (dry) component stands for a standard atmosphere and can be calculated as a function of latitude and height. Whereby the wet component refers to the water vapour and therefore is more challenging to model, as described in section 2.2.1., water vapour is temporally and spatially fluctuating associated with temperature (Hanssen, 2002).

Meteorological data from ERA-Interim daily, were verified by the meteorological ground station of *St. Denis Gillot* and meteorological data of NOAA. The station and the NOAA data provided useful and relevant verification that support the ERA-Interim data. With this given meteorological data set, it was possible to estimate the total delay of an electromagnetic wave along the slant range in LOS. The APD model of RSL predicts the atmospheric phase parameters at each pixel, while using the SRTM 1arc sec HGT DEM of *La Réunion* for fitting on the DInSAR products with a pixels pacing of 30.8m. The APD model was fed with meteorological data of ERA-Interim, estimating the total path delay (Briole et al., 1997; Bonforte et al., 2001; Jehle et al., 2008; Schubert and Small, 2016).

The APD model was fed with ERA-Interim data of Temperature [$T_{s,c}$ in $^{\circ}C$], atmospheric pressure [P_s in *mbar*], the relative humidity [RH_s in %] and the height above sea of the ERA-Interim measurements, in this case 2m above surface [h_s] (Schubert and Small, 2016; ERA-Interim Daily). Information about the relative humidity (RH_s) was not delivered by ERA-Interim, but ECMWF provided a formula for calculation. First it was necessary to obtain the saturation water vapour pressure ($e_{sat}(T)$), by the following equation (ECMWF Part IV: Physical Processes):

$$e_{sat}(T) = a_1 \exp \left\{ a_3 \left(\frac{T - T_0}{T - a_4} \right) \right\} \quad (4.8)$$

Where the saturation water vapour pressure ($e_{sat}(T)$) is expressed with the Teten's formula (ECMWF Part IV: Physical Processes) combined with the saturation over water parameter ($a_1= 611.21Pha$, $a_3=17.502$, $a_4=32.19K$) from Buck (1981). Now with this parameter and an additional parameter as the dew point temperature it was possible to calculate the relative humidity (RH_s) (Buck, 1981; ECMWF near-surface humidity). Where (T) is the temperature expressed in Kelvin and (Td) stands for the 2m dew point temperature:

$$RH = 100 * \frac{e_{sat}(Td)}{e_{sat}(T)} \quad (4.9)$$

At this point all the requested parameter for the APD model of RSL were combined to calculate the tropospheric path delay. First of all, the laps rates β and λ were estimated. The mean values are latitude dependent, also the deviation is depending on the day of the year. The following table 8 shows the variation of the laps rates β and λ and was calculated by a linear interpolation. For example, for a given latitude, a mean and seasonal deviation were obtained.

Table 8: Average and seasonal variation magnitudes of the temperature and water vapour lapse rates (Schubert and Small, 2016).

Latitude[$^{\circ}$]	Mean		Maximum seasonal deviation	
	[K/m]	$\Delta\lambda[-]$	[K/m]	$\Delta\lambda[-]$
≤ 15	$6.30 * 10^{-3}$	2.77	$0.00 * 10^{-3}$	0.00
30	$6.05 * 10^{-3}$	3.15	$0.25 * 10^{-3}$	0.33
45	$5.58 * 10^{-3}$	2.57	$0.32 * 10^{-3}$	0.46
60	$5.39 * 10^{-3}$	1.81	$0.81 * 10^{-3}$	0.74
≥ 75	$4.53 * 10^{-3}$	1.55	$0.62 * 10^{-3}$	0.30

Also it was necessary to define a temporal offset D_{min} this depended on the hemisphere. The island *La Réunion* is located on the southern hemisphere, which was defined as:

$$D_{min} = 28 + \left(\frac{365.25}{2}\right) = 210.265 \text{ (for southern latitude)} \quad (4.10)$$

For the final calculation of the daily lapse rates of β and λ , there was a need to define D as the specific day of the year.

$$\beta = \bar{\beta} - \Delta\beta * \cos\frac{2\pi(D - D_{min})}{365.25} \quad (4.11)$$

$$\lambda = \bar{\lambda} - \Delta\lambda * \cos\frac{2\pi(D - D_{min})}{365.25} \quad (4.12)$$

After calculating the lapse rates, it was necessary to convert the temperature T_s from Celsius to Kelvin and scale the temperature T_0 to sea level.

$$T_s = T_{s_c} + 273.15 \quad (4.13)$$

$$T_0 = T_s + \beta * h_s \quad (4.14)$$

In addition, the mean tropospheric temperature T_m and the station water vapour pressure e_s needed to be estimated for further procedure.

$$T_m = T_0 \left(1 - \frac{\beta R_d}{g(\lambda + 1)}\right) \quad (4.15)$$

$$e_s = \left(\frac{RH_s}{100}\right) * 6.112 * e^{\left(\frac{17.67(T_{s_c})}{243.5 + T_{s_c}}\right)} \quad (4.16)$$

As mentioned in the theory section, the wet and dry components were calculated in the following steps to obtain the delay sensitivity terms. Followed by the calculation Ψ_{hyd} and Ψ_{wet} of the dry and wet component of 2m above surface.

$$\tau_{hyd} = 10^{-6} k_1 * \frac{R_d}{g_m} \quad (4.17)$$

$$\tau_{wet} = 10^{-6} * \left(\frac{(k_2 T_m + k_3) R_d}{g_m(\lambda + 1) - \beta R_d}\right) \quad (4.18)$$

$$\Psi_{hyd} = \tau_{hyd} * P_s \text{ (hydrostatic delay 2m above surface)} \quad (4.19)$$

$$\Psi_{wet} = \tau_{wet} * \left(\frac{e_s}{T_s}\right) \text{ (wet delay 2m above surface)} \quad (4.20)$$

The parameters were calculated for the fix point 2m above surface [h_s]. Now the same parameters were calculated for the given DEM to receive the corresponding path delays. First of all, the hydrostatic κ_{hyd} and wet κ_{wet} delay scaling factors were defined as the following shows:

$$\kappa_{hyd} = \left(1 - \frac{\beta h}{T_0}\right)^{\frac{g}{\beta R_d}} \quad (4.21)$$

$$\kappa_{wet} = \left(1 - \frac{\beta h}{T_0}\right)^{\left(\frac{g_m(\lambda+1)}{\beta R_d} - 1\right)} \quad (4.21)$$

In addition, the air pressure P_0 and the water vapour pressure e_0 were scaled to sea level:

$$P_0 = P_s \left(\frac{T_0}{T_s}\right)^{\frac{g}{\beta R_d}} \quad (4.22)$$

$$e_0 = e_s \left(\frac{T_0}{T_s}\right)^{\left(\frac{g_m(\lambda+1)}{\beta R_d} - 1\right)} = e_s \left(\frac{P_0}{P_s}\right)^{(\lambda+1)} \quad (4.23)$$

The output was a zenithal hydrostatic Ψ_{hyd} and wet Ψ_{wet} delay equation:

$$\Psi_{hyd} = \tau_{hyd} * \kappa_{hyd} * P_0 \quad (4.24)$$

$$\Psi_{wet} = \tau_{wet} * \kappa_{wet} * \left(\frac{e_0}{T_0}\right) \quad (4.25)$$

Considering the sensors viewing angle in LOS, the equation above needed an additional factor to convert the zenithal delay to the sensors slant range by adding the nominal incident angle θ_i .

$$\Psi_{tropo} = (\Psi_{hyd} * \Psi_{wet}) * \frac{1}{\cos(\theta_i)} \quad (4.26)$$

In summary, the total one-way path delay is the sum of the tropospheric Ψ_{tropo} and the ionospheric Ψ_{iono} delay. For a two-way calculation the product was multiplied by two.

Total atmosphere path delay estimation

$$\Psi_{atmo} = \Psi_{tropo} + \Psi_{iono} \quad (one - way) \quad (4.27)$$

These APD calculations above generated the signal transmit path delay for every pixel on the imagery. The end product was applied to the DInSAR measurements of S1A for correction.

4.3. Generation of path delay reference map for APD correction

At this moment the DInSAR product were processed via an interferometric approach by SNAP and SNAPHU. In addition, the meteorological data from ERA-Interim were structured and processed for calculating the corresponding APD for the volcanic scene.

The APD was generated for the three S6 data (02.03.2016, 07.04.2016 & 19.04.2016). The total APD difference was obtained, analogous to the DInSAR approach, where the calculation was ‘‘Slave minus Master’’. Both, the unwrapped values of the DInSAR measurement and the total APD difference were subtracted pixel wise from each other:

$$(1) \text{ absolute phase values} - (2) \text{ total APD difference} = (3) \text{ Atmospheric corrected DInSAR}$$

On condition that (1) and (2) showed the identical pixel spacing, the same geometry and the same dimensions. This task was a crucial processing step with regard to the exact pixel spacing and the use of the WGS84 reference system. This processing was done with Matlab.

5. Results

In the following the results obtained from the discussed method are showed, described and analysed. First, the DInSAR results are presented. This is followed by the APD estimation based on the ERA-Interim meteorological data and the results of the atmospheric corrected DInSAR measurements. Tables 9 & 10 display the product specification of the evaluated interferometric pair One and Two. The APD was calculated for different elevations, resulting that the lowest part of the island showed higher path delays compared to the higher elevations. Hanssen (2002) and Doin et al. (2009) confirmed this path delay dependency in their studies. Generally, the lower atmosphere is denser than the higher part.

Table 9: Pair One - SLC from 02.03.2016 & 07.04.2016 and its characteristics, own representation.

Pair One: 02. March 2016 & 07. April 2016	
S1A_S6_SLC__1SDV_20160302T145244_20160302T145307_010191_00F0AD_D28E	Master, Track: 144, Orbit: 10191
S1A_S6_SLC__1SDV_20160407T145244_20160407T145308_010716_00FFC7_A6F9	Slave, Track: 144, Orbit: 10716
Perpendicular Baseline	69.45m
Temporal Baseline	36 days
Polarization	VV
Path delay mean differences in total	0.616m
Path delay mean differences 0-500m	0.7308m
Path delay mean differences 500-1000m	0.6917m
Path delay mean differences 1000-1500m	0.6645m
Path delay mean differences 1500-2000m	0.6445m
Path delay mean differences 2000+ m	0.6261m
Modelled coherence	0.91
Ambiguity Height	262.53m
Volcanic activity	negative

Table 10: Pair Two - SLC from 02.03.2016 & 19.04.2016 and its characteristics, own representation.

Pair Two: 02. March 2016 & 19. April 2016	
S1A_S6_SLC__1SDV_20160302T145244_20160302T145307_010191_00F0AD_D28E	Master, Track: 144, Orbit: 10191
S1A_S6_SLC__1SDV_20160419T145245_20160419T145309_010891_01050B_A397	Slave, Track: 144, Orbit: 10891
Perpendicular Baseline	39.85m
Temporal Baseline	48 days
Polarization	VV
Path delay mean differences in total	0.784m
Path delay mean differences 0-500m	0.8295m
Path delay mean differences 500-1000m	0.8026m
Path delay mean differences 1000-1500m	0.7879m
Path delay mean differences 1500-2000m	0.7771m
Path delay mean differences 2000+ m	0.7689m
Modelled coherence	0.92
Ambiguity Height	457.52m
Volcanic activity	negative

5.1. DInSAR Results

Coregistration & Coherence

For Pair One & Two the coherence of volcanic areas was calculated and presented in figures 24 & 25. The red arrows indicate the SA1 look direction.

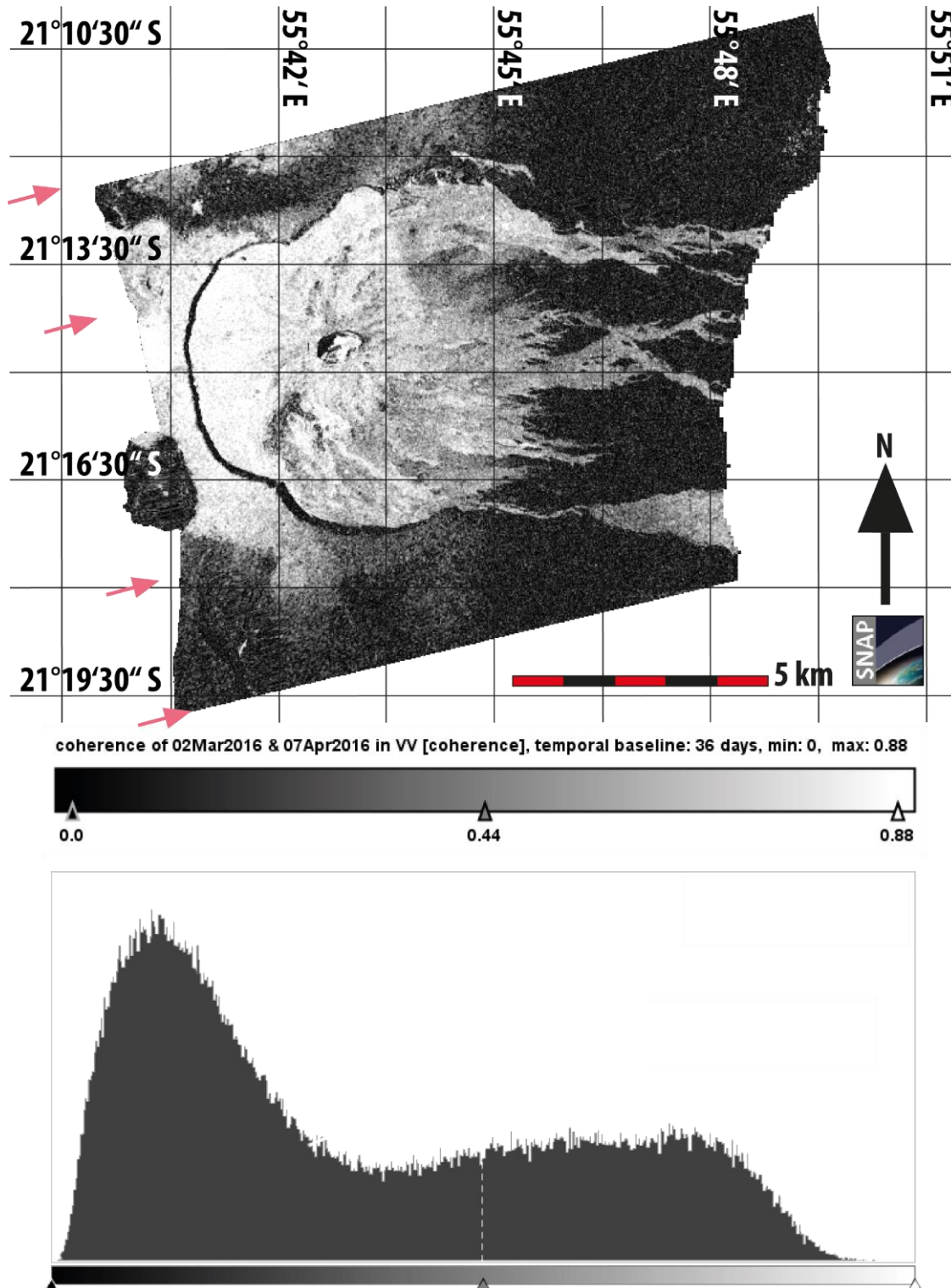


Figure 24: Coherence output of pair One including the corresponding histogram of the represented values, own representation.

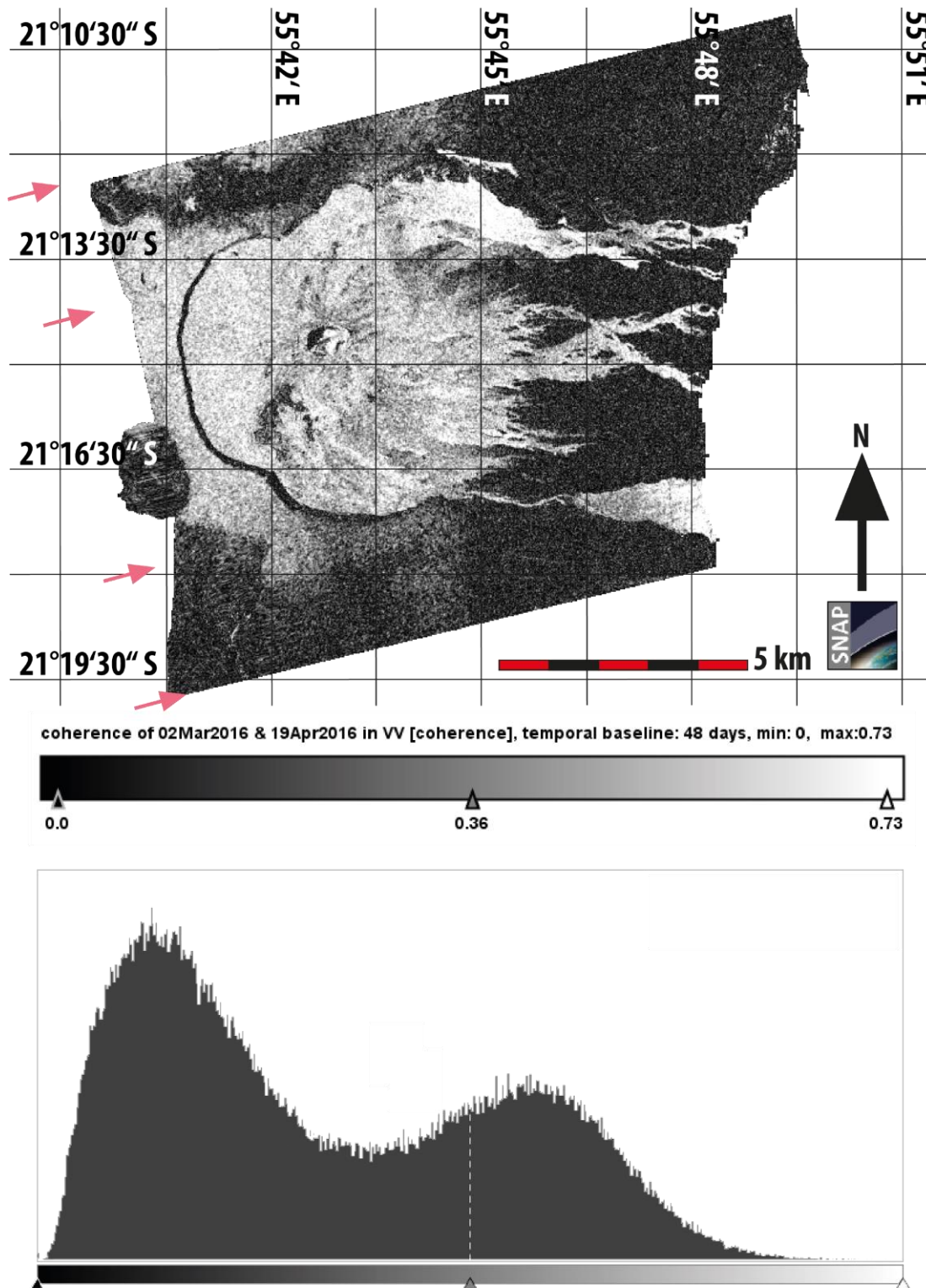


Figure 25: Coherence output of pair Two including the corresponding histogram of the represented values, own representation.

In general, the results of the coherence of Pair One and Two show good coherence on the top of the volcano and the lava flows. This might be due to the absence of vegetation. In pair One the range of min-to-max values are from 0 - 0.88 and the distribution of the histogram shows that most of the values are pixels with low coherence.

Where in pair Two the range of min-to-max values vary from 0 - 0.73, lower than in pair One. Instead of reaching more out to the value of 1, it shortens and the histogram shows relatively more coherent pixels in the range of 0.4 to 0.5.

In both pairs, low coherence was measured and observed. Reasons for this could be atmospheric noise, surface movement or vegetation. For the sake of simplicity, the minor issues which contribute to decorrelation in the case of repeat-pass interferometry like satellite clock errors, phase errors due to thermal noise, baseline errors, false focusing, DEM errors, geometric decorrelation and image disintegration are neglected more (Rosen et al., 1996; Ferretti et al., 2001).

Interferometric data after applying Goldstein Filtering

The next output stands for the following processing steps: Coregistration – Interferogram generation – Topo-Removal and the filtering by Goldstein. The fringes are still wrapped and reach from $-\pi$ to $+\pi$ (radians) as seen in the min-to-max values range of both pairs.

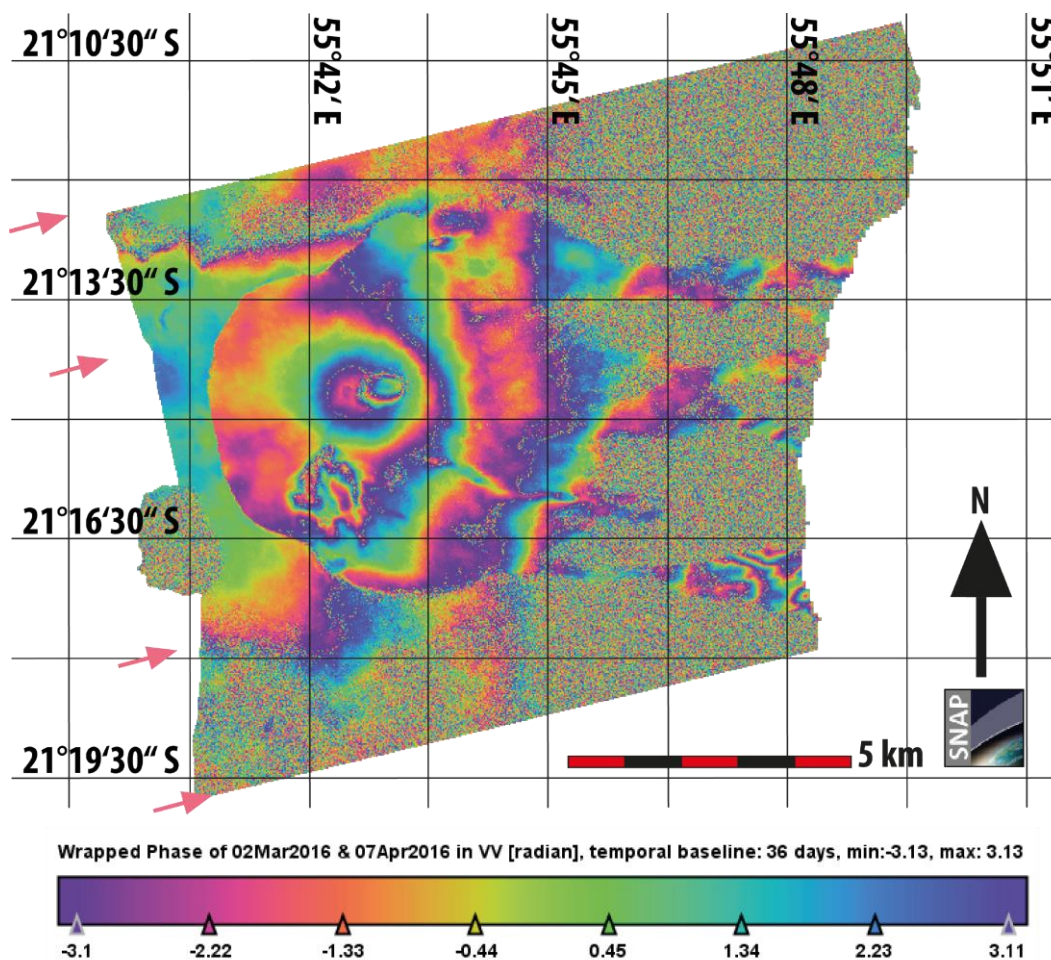


Figure 26: Wrapped phase values in radians of pair One. Also a demonstration of the bandwidth of the values $[-\pi, \pi]$, own representation

The coastal region is on the eastern part where the lava flows into the ocean. South of the crater there are two volcanic outlets that cause distinct fringe pattern. In part Two, there is much more decorrelation detected at the outlets than in pair One. This might be caused by the larger temporal baseline of 48 days (pair One: 36 days).

In both pair outputs there is a semi-circle curvature visible that is in the western part of the images and indicating a cliff (height difference 160m). This geological artefact causes a sudden fringe colour

change. In both interferograms, the dominating noisy parts show in the north and south section some fringe pattern. Also the fringe pattern varies over both areas, but it is obvious, that the coherent pixels deliver the most reliable phase information. The pixels with low coherence values lead to noisy areas in figures 26 & 27, due to vegetation movement. Regarding the surface movement, as the two SLC in pair One and Two were chosen during a restful period of the volcano, there should be little relevant surface movement, otherwise the movement cannot be isolated from atmospheric artefacts.

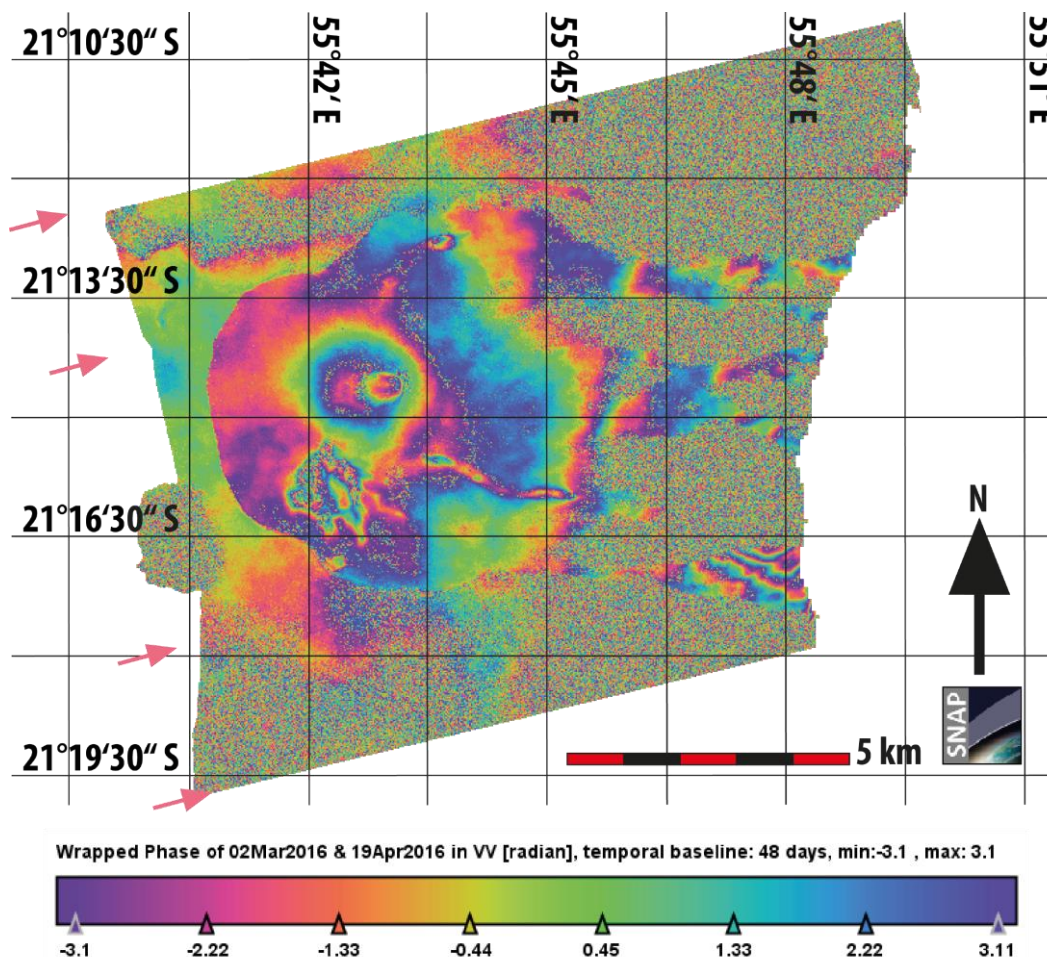


Figure 27: Wrapped phase values in radians of pair Two. Also a demonstration of the bandwidth of the values $[-\pi, \pi]$, own representation.

Unwrapped Interferometric Phase

The next task was to unwrap the DInSAR measurement. The object of phase unwrapping is to determine a continuous phase profile out of the phase cycle with values between $-\pi, \pi$. Usually this is done by adding integer multiples of a phase cycle. At this point there is still no absolute phase information but SNAPHU processed a coherent unwrapped phase field in radians.

In several other unwrapping attempts this geological curvature, which is part of the caldera, led to unwrapping errors. It is obvious that the low coherent regions show a less linear colour trend than the coherent pixels, based also on the unwrapping interpolation. More important, the output of pair One and Two show a linear colour gradient measured from the crater down to the Oceanside. This can be interpreted as an atmospheric contribution given no relevant surface movement. This result fulfils the expectation that the chosen pairs can be taken to study atmospheric artefacts. It is important to understand that the elevation was previously removed in the DInSAR processing by the Topo-Removal task, even if the colour pattern has a bottom-up or top-down colour gradient in figures 28 & 29 that

correlates with the volcanic topographical structure. This was an evidence that the atmospheric effects exist. In addition to that, the atmospheric effects are mostly high-dependent and the lower troposphere was denser than the troposphere on top of the volcano (2632m).

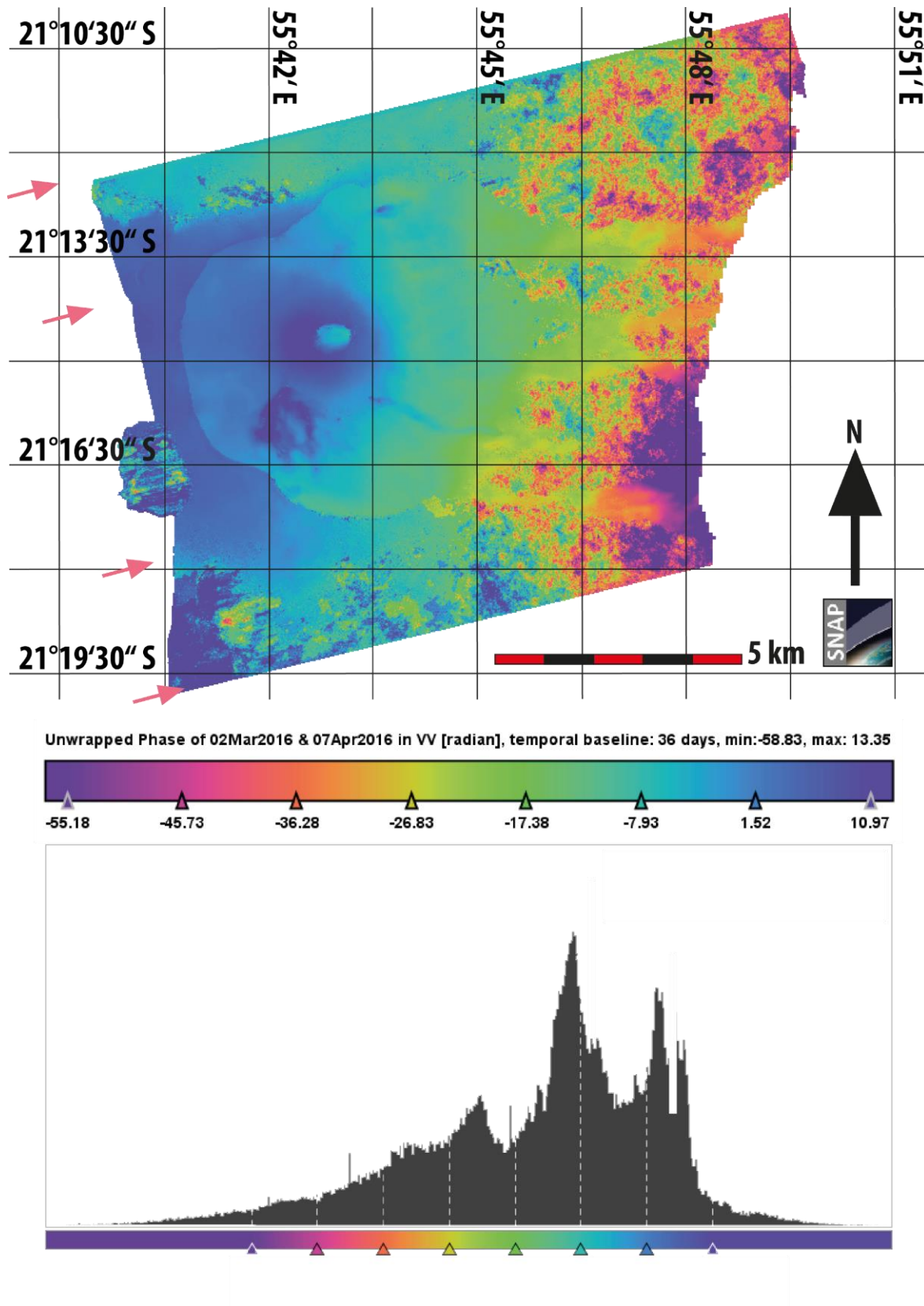


Figure 28: Unwrapped phase values in radians of pair One. Minimum and maximum of the unwrapped phase represented, own representation.

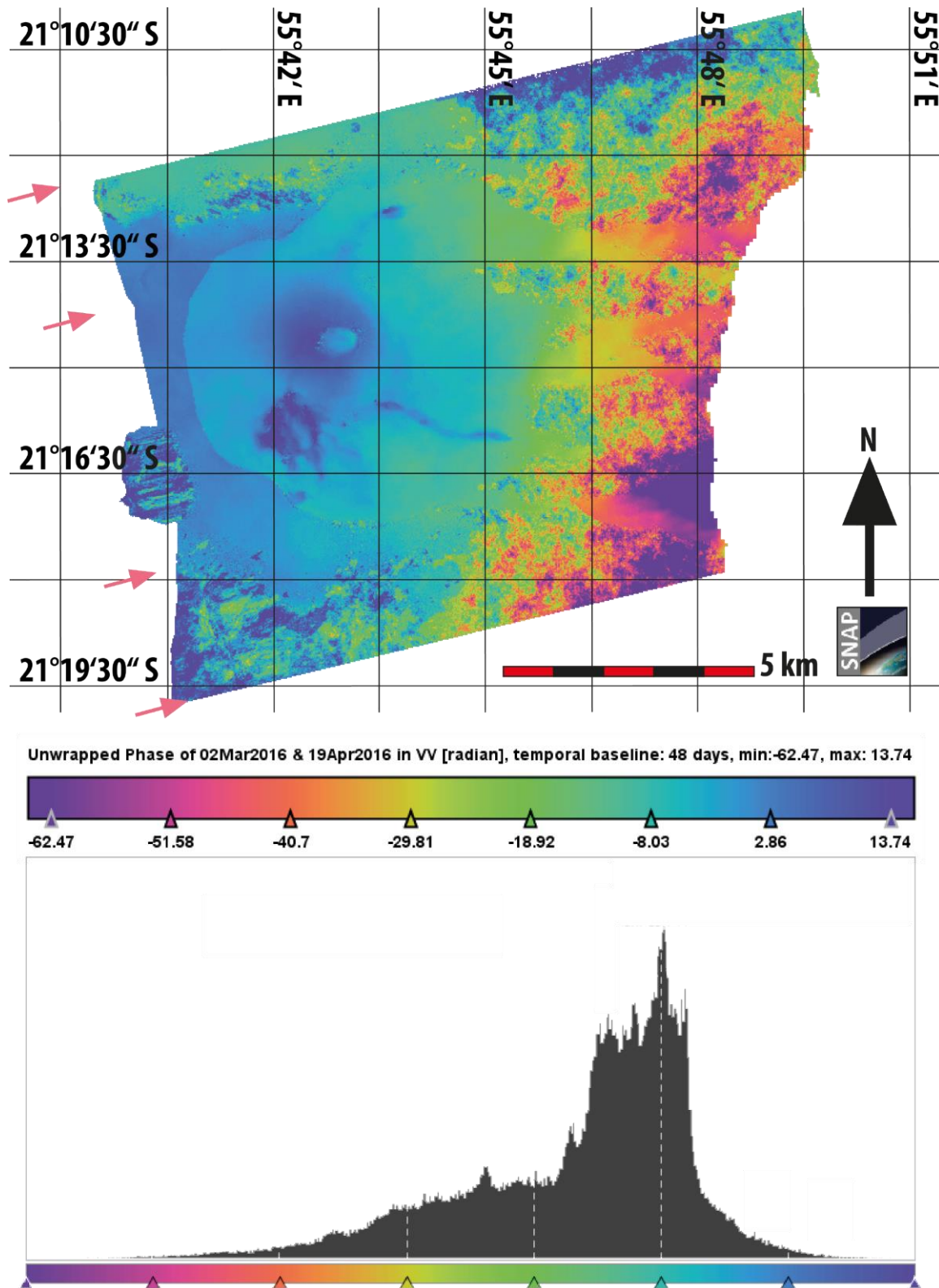


Figure 29: Unwrapped phase values in radians of pair Two. Minimum and maximum of the unwrapped phase represented, own representation,

Preparing the Scene for APD correction

As the phase unwrapping was successfully completed, the data files were exported from SNAP into Matlab by generating a NetCDF4-BEAM data type (.nc format). The DInSAR measurements were still in radians and needed to be converted into distance (here cm was used), as also the estimated APD product is in cm. This step was performed by the following formula:

$$\text{unwrapped phase in cm} = \frac{5.54657\text{cm} * \text{unwrapped phase in radians}}{2 * 2\pi} \quad (5.1)$$

Where 5.54657 cm is the C-Band of S1A and the factor 2 was applied based on the two-way estimation. The unwrapped phase in radian are the pixel values after unwrapping the wrapped phase. The following results of pair One were converted from radians into cm. Figure 30 & 32 represent the same volcanic study area as figures 28 & 29, but coloured with a different and more distinctive colour scheme.

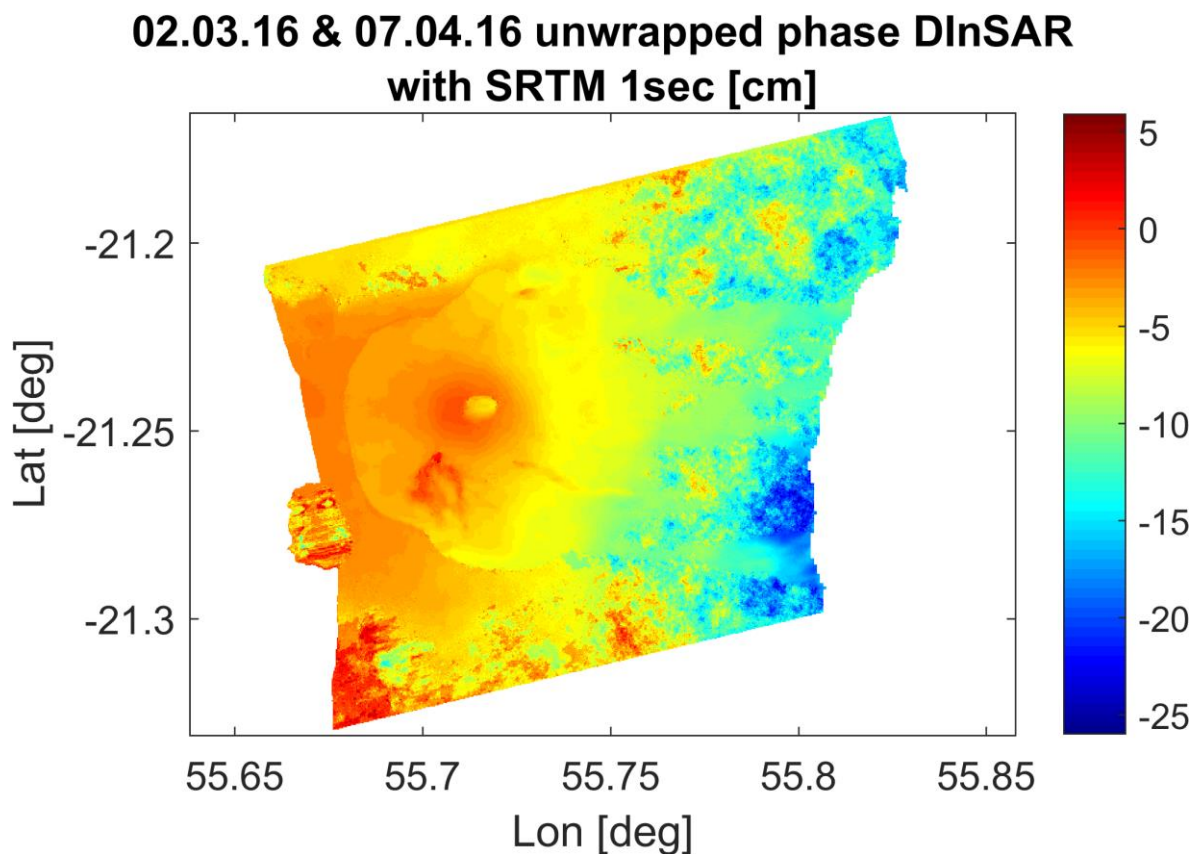


Figure 30: Unwrapped absolute values converted into cm of pair One.

Figure 31 was modified to only represent the unwrapped phase value, superimposing the coherent value. As a coherence threshold the value 0.4 was chosen. A higher value would have resulted in very little coherence pixels in this sense very few unwrapped pixels. Lower value such as 0.3 were tested, but included unfortunately not desirable areas and included noisy parts, which needed to be avoided.

02.03.16 & 07.04.16 unwrapped phase DInSAR with SRTM 1sec coh>0.4 [cm]

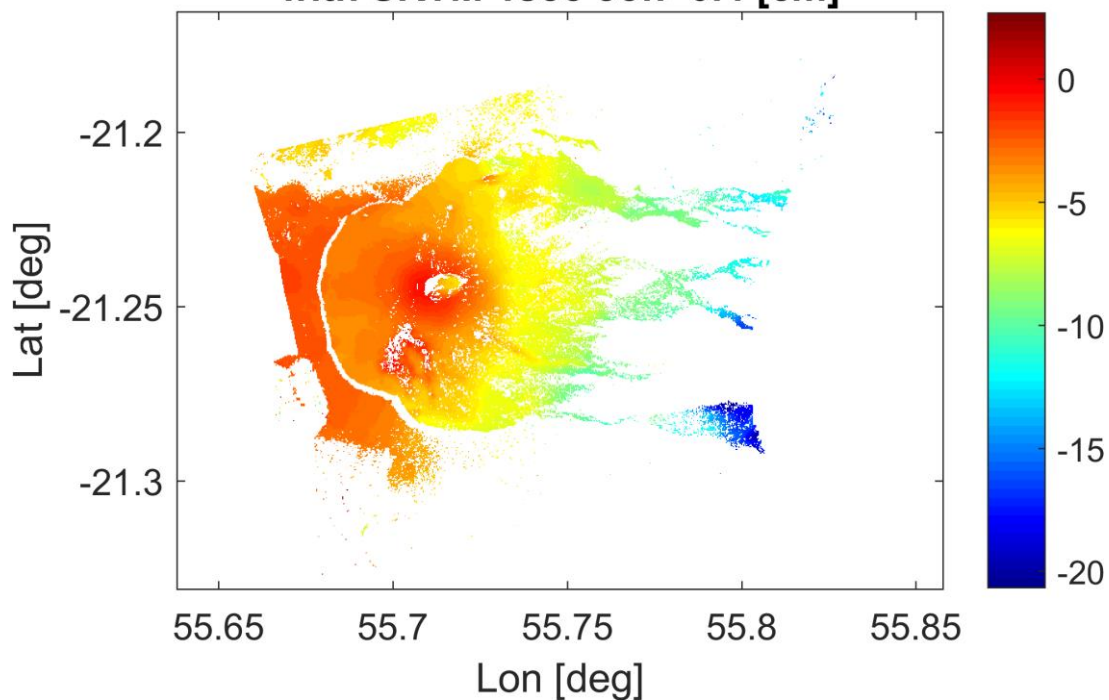


Figure 31: Unwrapped absolute values converted into cm, showing only the coherent pixels with values above 0.4 of pair One.

Also pair Two was processed the same way and converted from radians into cm. A more distinctive colour scheme and a coherent threshold of 0.4 was applied.

02.03.16 & 19.04.16 unwrapped Phase DInSAR with SRTM 1sec [cm]

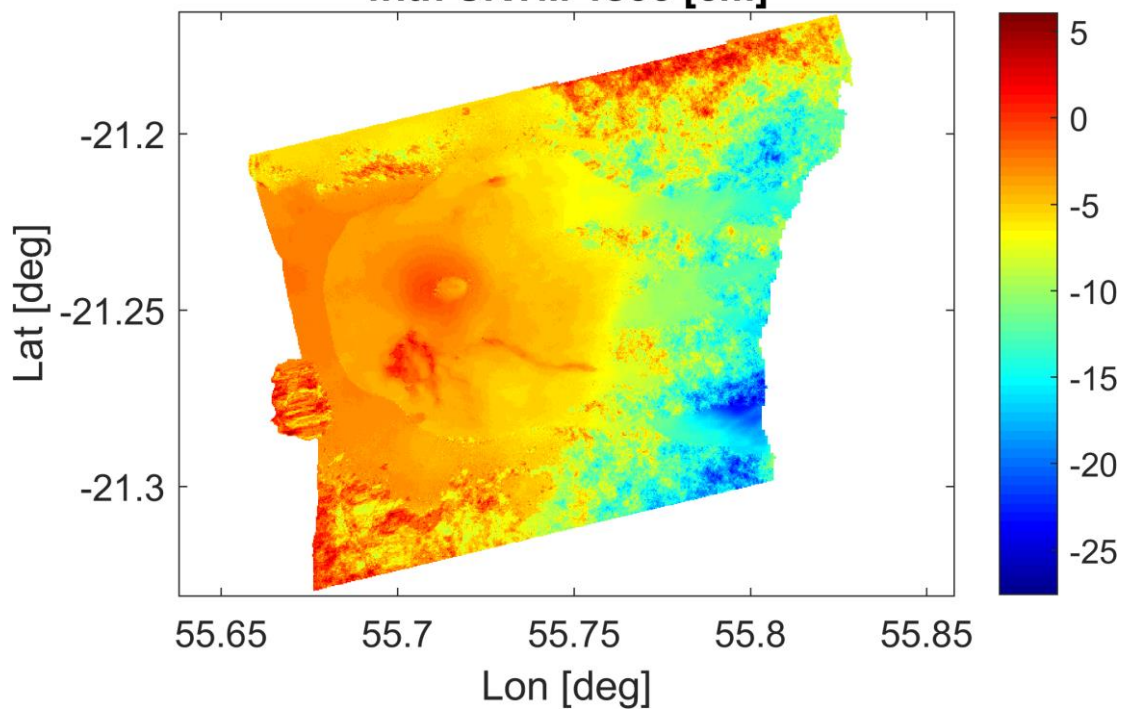


Figure 32: Unwrapped absolute values converted into cm of pair Two.

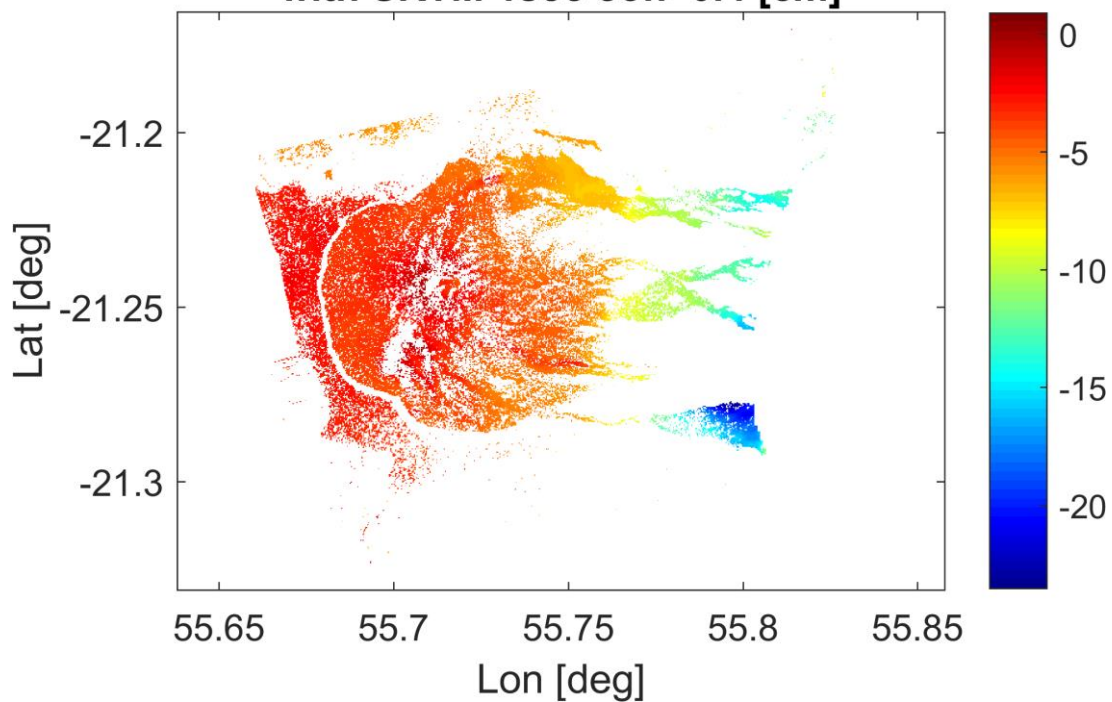
**02.03.16 & 19.04.16 unwrapped phase DInSAR
with SRTM 1sec coh>0.4 [cm]**

Figure 33: Unwrapped absolute values converted into cm, showing only the coherent pixels with values above 0.4 of pair Two.

Both pairs were modified to be compatible with the APD estimation product by converting the value into cm. Masking out the encountered noise might allow to receive more relevant results in the end of the atmospheric corrected interferogram. In figure 33 the coherence threshold of 0.4 reveals that on the volcanic plateau have not as good coherence as the pair One shows.

5.2. Generating the total APD difference

In the next section the estimated APD is presented. Understanding the properties of the ionospheric and tropospheric layer on the DInSAR measurements requires the Knowledge of the atmospheric characteristics at the time and date of the SAR acquisition (02.03.2016, 07.04.2016 and 19.04.2016) used for the DInSAR measurements. The following evaluation was carried out to quantify the possible ionospheric and tropospheric effects in volcanic region (Sarti et al., 1999).

Table 11: The atmospheric path delay measured on time and date of the SLC acquisition. Minimum, maximum and mean values are shown in correspondence to the respective atmospheric layer, own representation.

APD estimation for SLC 02.03.2016 (cm)			
	Mean	Max	Min
Ionosphere	99.1568	100.0662	98.2618
Troposphere	449.7163	524.1032	357.979
Total	717.7503	828.1892	589.2865

APD estimation for SLC 07.04.2016 (cm)			
	Mean	Max	Min
Ionosphere	45.154	45.4993	44.8147
Troposphere	439.2503	509.2128	352.0793
Total	649.3813	753.0254	527.3953

APD estimation for SLC 19.04.2016 (cm)			
	Mean	Max	Min
Ionosphere	29.1857	29.3758	28.999
Troposphere	442.1601	513.7011	353.3232
Total	637.4005	743.0987	513.7011

The two-way APD estimation provides a good overview of which part of the atmospheric layer causes how much signal delay in cm. The mean of the total delay is 637.4003 cm up to 717.7503cm. Regarding the tropospheric path delay, it is clear that the variation in the three acquisition dates is not varying largely. In the case of the ionospheric path delay, table 11 shows significant differences from 29.1875 to 99.1568cm of path delay.

Table 12: Total APD difference of the particular SLC is subtracted for obtaining the path delay difference, own representation.

Total APD Difference of Pair One: 02.03.2016 - 07.04.2016 (cm)			
	Mean	Max	Min
Ionosphere	54.0027	54.5669	53.447
Troposphere	10.466	14.8903	5.8997
Total	68.3691	75.1637	61.8911

Total APD Difference of Pair Two: 02.03.2016 - 19.04.2016 (cm)			
	Mean	Max	Min
Ionosphere	69.9711	70.6905	69.2628
Troposphere	7.5562	10.4021	4.6558
Total	80.3499	84.0905	76.129

Table 12 shows the total APD difference for the ionospheric, tropospheric and the total delay. This table presents clearly that the ionospheric path delay difference was significantly larger than the troposphere-

induced delay. The path delay caused by the troposphere was small in both pairs, in pair Two the differences from ionospheric and tropospheric path delay is 9.2 times higher, compared to pair One that is 5.1 times higher.

First, it can be said that the interaction of the ionosphere with the traversing signals gives a much larger difference than the tropospheric effect. Thus the total signal delay difference ratio of 68.3691cm of pair One is caused by the ionosphere (78.98%) and the troposphere (21.02%). Where the total signal delay difference ratio of pair Two values 80.3499cm is split into the ionospheric (87.08%) and the tropospheric (12.92%) part. Second, the ionospheric effect varies only 1.03% for pair One and 1.02% for pair Two. The impact of TEC variations was limited and behaved as large-scaled effects, thus this might vary significantly only over large areas (100km and more), which was not relevant when observing an area of 17km x 13km as *Piton de la Fournaise* (Bonforte et al., 2001). The worldwide variation of the TEC is seen in the appendix (figure 53). Third, the ionospheric effect compared to the variation of the tropospheric effects was significantly stronger which is 43.1% for pair One and 38.1% for pair Two. The expectation was hereby confirmed to find large tropospheric APD differences. Hopefully those results could lead to a significant atmospheric correction.

The figures 34 & 35 present the estimated total APD differences over the volcanic area. These figures almost look identical, but the spread spans differences. Also there were some visible differences in the figures. The eastern part of the image there is the ocean, but instead of defining it to NaN values, there was the TEC map behind that showed a pattern of ionospheric effects. The mean in pair One is 68.3691cm and the APD model had a spread of 13.2726cm (min to max). Regarding the comparison between pair One and Two, the latter one showed a higher mean of 80.3499cm of total APD difference but the spread of 7.9615 (min to max) was smaller than in pair One.

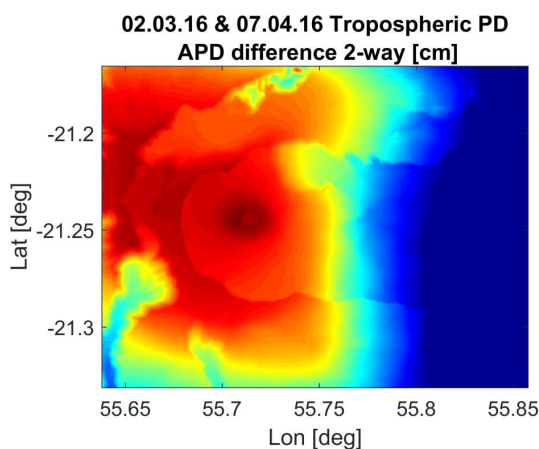


Figure 34: Total APD difference of pair One.

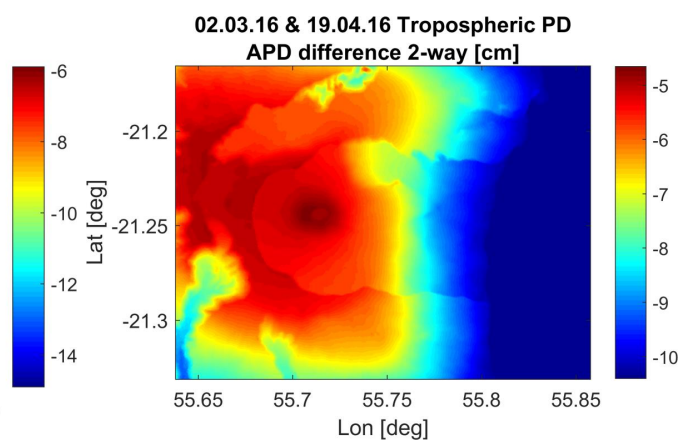


Figure 35: Total APD difference of pair Two.

Both images (figures 34 & 35) show the estimated path delay, that reproduces an approximation of a DEM of the volcanic area. As discussed above, the ionosphere is in the background and does not cause this kind of topographical result. In this case the tropospheric disturbances induce this kind of sub-kilometre scale variability. The strong height dependency was caused by the troposphere as mentioned in the theoretical part of this thesis. To see the separated atmospheric path delay maps of the troposphere in the absence of the ionospheric layer and vice versa (the corresponding figures 56 & 67 and 60 & 61 are available in the appendix.).

The application of S1A SLC in S6 allowed the shallowest angle of LOS of its platform, thus the electromagnetic signal had one of the longest travelling time through the atmospheric layers. The results were showing a long path delays and as this thesis is about obtaining and experimenting a suitable atmospheric correction method, there is no better proving ground to compute the APD estimation.

5.3. Atmospheric corrected DInSAR measurements

5.3.1. Pair One: 02.03.2016 & 07.04.2016

Finally, the atmospheric correction can be computed by simply subtracting figure 31 minus figure 34, or for the corresponding pair Two, the figure 32 minus figure 35. The estimated APD differences were subtracted from the original DInSAR measurement, resulting in an atmospheric corrected interferogram. As the InSAR baseline-induced topographic information was removed by Topo-Removal there should not be any induced heights. Referring to pair One (figures 30 & 31), where the colour scheme (phase-elevation dependency) indicates a highly dependent pattern, the atmosphere-corrected DInSAR interferogram should not represent any colour scheme in the final results that correlates with the topographic height (figure 36). In general, the atmospheric effects act like a topographic layer, based on its physical property and this layer is removed and should provide a feasible result. Thus the values should optimally be “flattened”, so that the atmosphere-induced height dependency is mitigated.

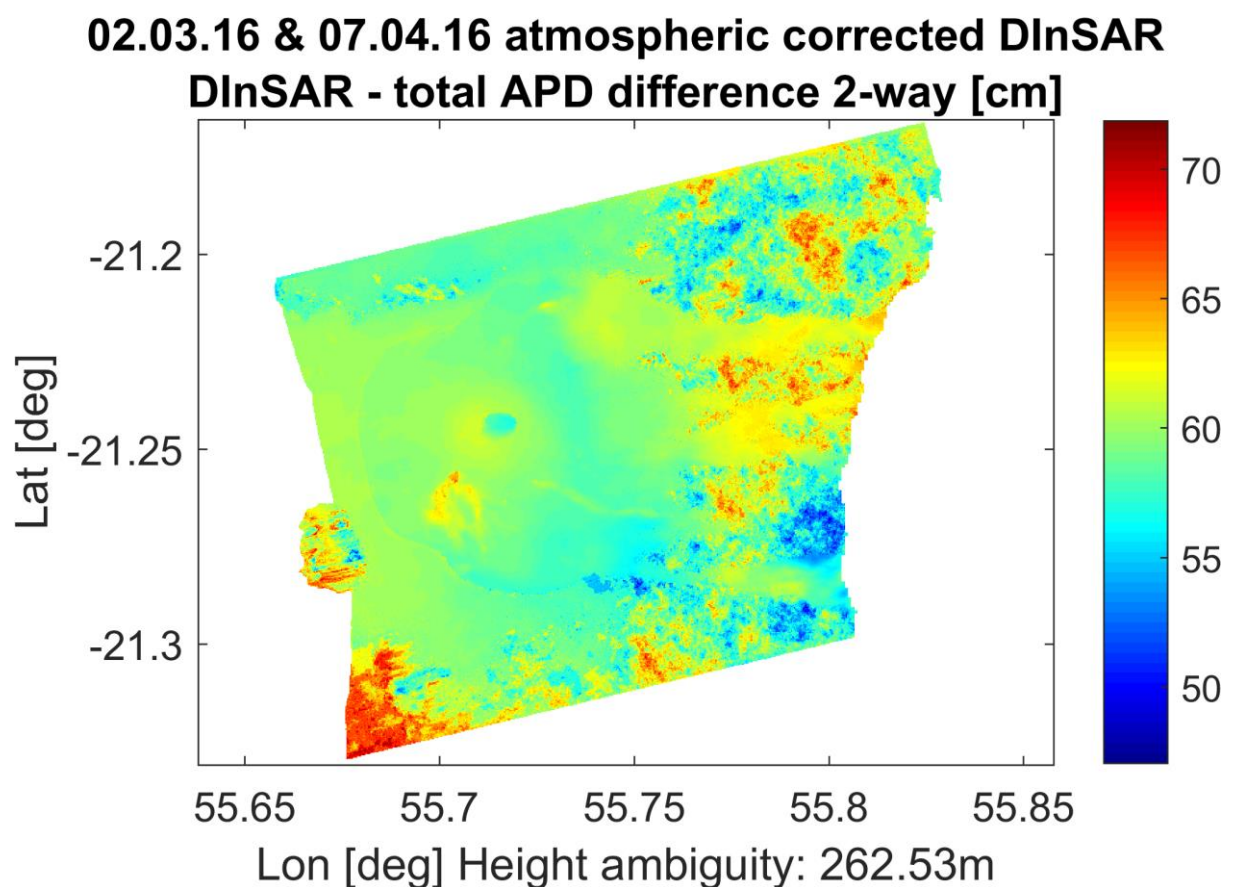


Figure 36: Atmospheric corrected DInSAR measurement with the total APD difference of pair One.

The result shows at first sight that the methods have worked well and visually the promised effect of removing the atmospheric effects was successful. But some geological structures are still visible, as the curved cliff in the east, the Bory and Dolomieu crater and observed lava flow on the eastern flank.

To verify these results statistically, a pixel based 2D density map (figures 37-40) were computed to observe the current adjustment. The 2D density map is spanned by the axis “Elevation” and the DInSAR measurements in cm. The colour indicates the density aka the frequency of the corresponding pixels. First it is to hope that the phase delay and elevation show a linear correlation (Doin et al., 2009) and second, to be able to correct the atmospheric artefact of height-dependence.

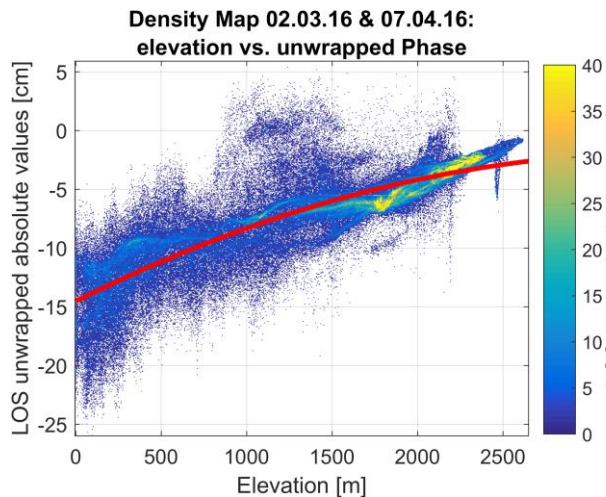


Figure 37: Density map based on the elevation of the volcanic area and the unwrapped absolute values of the DInSAR measurement of pair One.

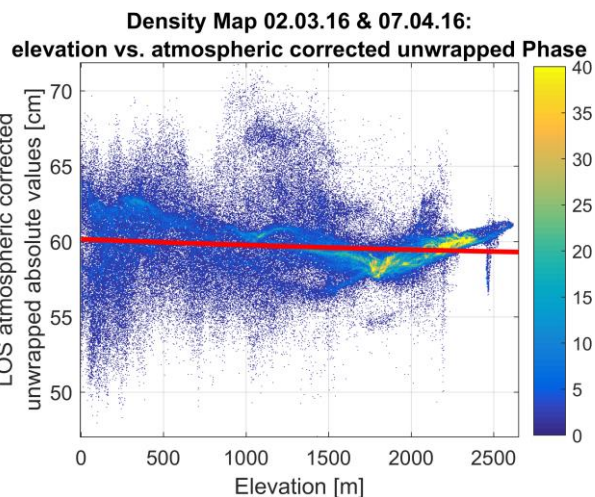


Figure 38: Density map based on the elevation of the volcanic area and the atmospheric corrected DInSAR measurement with the APD of pair One.

The statistical verification gives a further promising feedback. In figure 37, the height-dependent phase trend is remarkably present. When looking at the result in figure 38, the height-dependency were largely corrected. Also the spread was shifted into the centre, so that the overall spread was minimized from approximately -23cm to +3cm (spread of 20cm) to approximately 55cm to 65cm (spread of 10cm). The density map reveals that between 2000m to 2500m there was a large concentration of pixels. The reason for this correlation was that the volcano at this height has a plateau and there were many pixels with the same height. Consulting figure 14, shows also the high distribution of these heights of the area of interest. The fact of the absence of vegetation at this part of the volcano keeps the pixel stable and coherent. This delivers the fact that this correction method based on the APD is functioning and also gives reliable results to improve DInSAR interferograms.

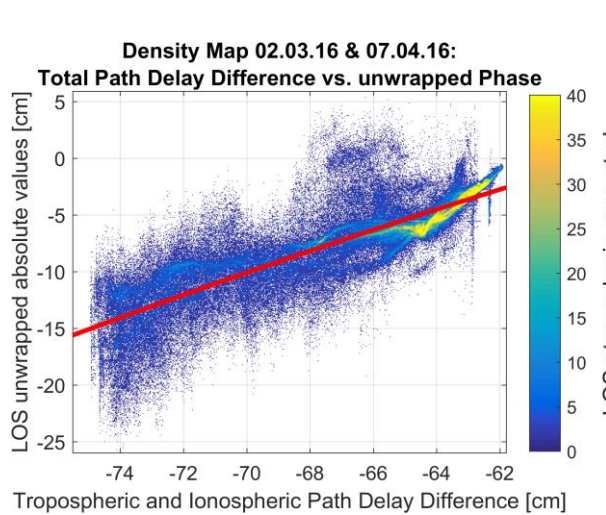


Figure 39: Density map based on the total APD difference and the unwrapped absolute values of the DInSAR measurement of pair One.

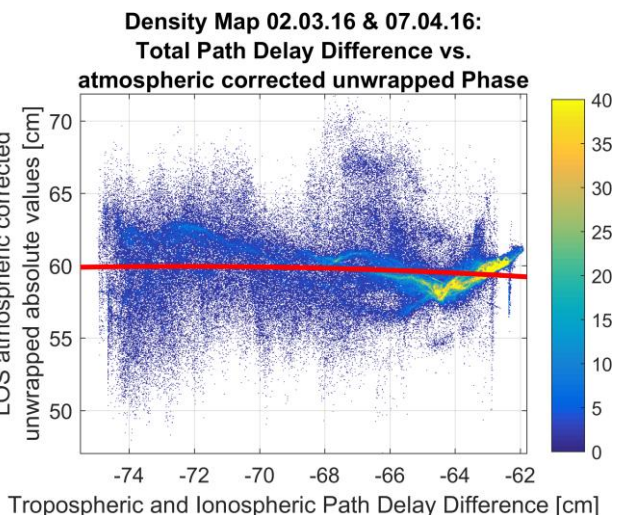


Figure 40: Density map based on the total APD difference and the atmospheric corrected DInSAR measurement with the APD of pair One.

Another statistical approach was completed to modify the density map and swap the x-axis to the total APD difference instead of the elevation of the volcanic area. This combination shows the intensity and correlation of a single pixel with a certain APD to an atmosphere corrected DInSAR measurement. Also this output showed significant improvement of the DInSAR measurement and it is said that this method effectively mitigated the atmospheric artefacts.

5.3.2. Pair Two: 02.03.2016 & 19.04.2016

To present the results of pair Two, figures 32 & 34 were computed to correct the APD. Figure 41 shows the visual result of the scene. The estimated APD differences were subtracted from the original DInSAR measurements, resulting in an atmosphere-corrected interferogram. The assumed presence of the atmospheric effects, indicating a high phase-elevation dependent pattern in figures 32-33, was largely successfully mitigated. As in figure 32, the same geological structures are even more prominent, as the curved cliff in the east, the craters Bory and Dolomieu and observed lava flow on the eastern flank. These structural artefacts could not be removed.

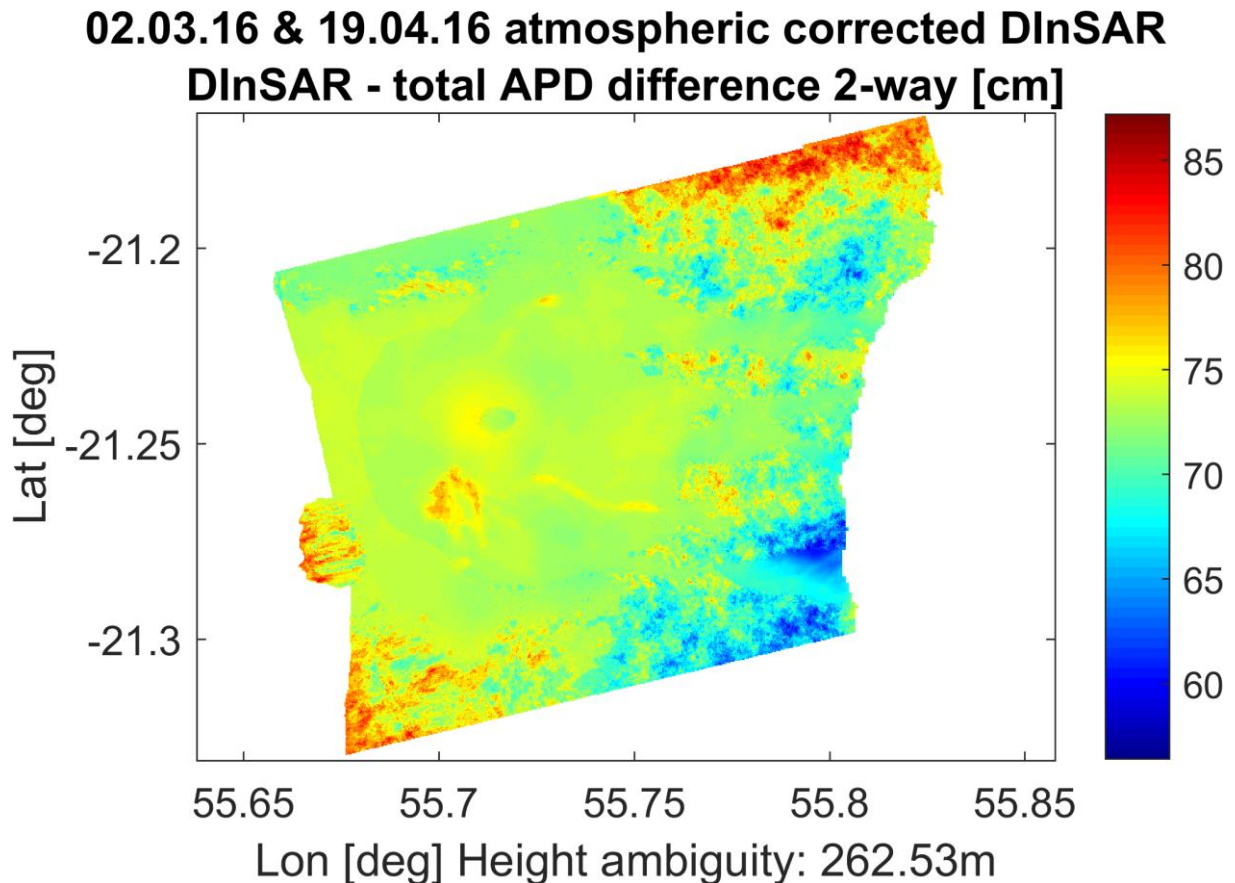


Figure 41: Atmospheric corrected DInSAR measurement with the total APD difference of pair Two.

Figure 41 shows the end product of the atmospheric mitigation. It can be said that the values were largely “flattened”, i.e. the height dependency of the atmospheric effect was mitigated. Also on pair Two the methods worked well and visually the promised effect of removing the atmospheric effects was successful. Also for this pair Two, a statistically pixel based density map was computed to observe the current adjustment.

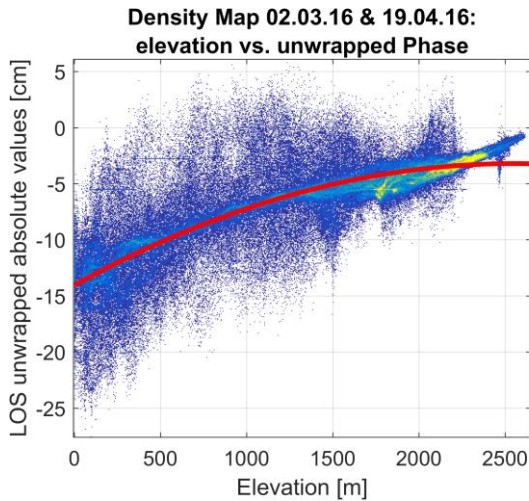


Figure 42: Density map based on the elevation of the volcanic area and the unwrapped absolute values of the DInSAR measurement of pair Two.

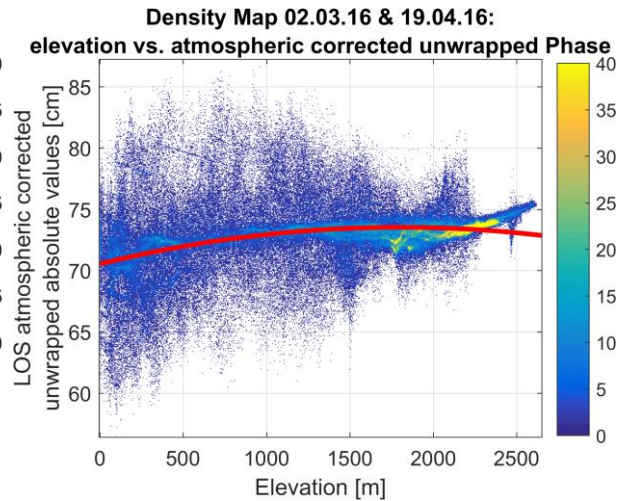


Figure 43: Density map based on the elevation of the volcanic area and the atmospheric corrected DInSAR measurement with the APD of pair Two.

The statistical approach by performing a density map lead to similar results as found in pair One, though the results were not as satisfying as in pair One. The height-dependent trend is strongly present in figure 42 and could mostly be corrected, but there was still a certain tendency left. Also the spread was mostly shifted into the centre, so the overall spread was minimized from approximately 0cm to -20cm (spread of 20cm) and from approximately 65cm to 80cm (spread of 15cm). Also in pair Two there was a large concentration of pixels between 2000m-2500m, contributing to the volcanic plateau and the strong coherence.

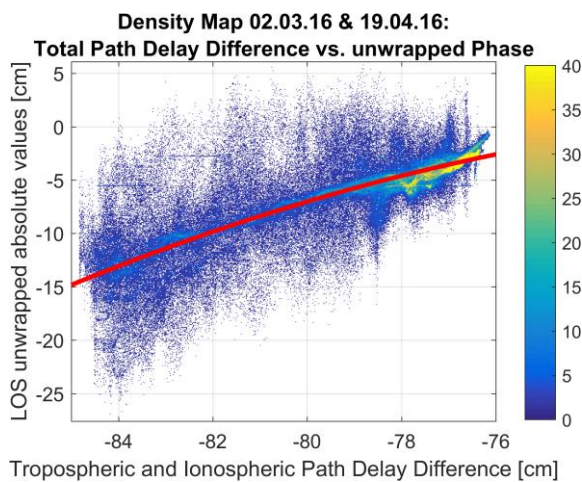


Figure 44: Density map based on the total APD difference and the unwrapped absolute values of the DInSAR measurement of pair Two.

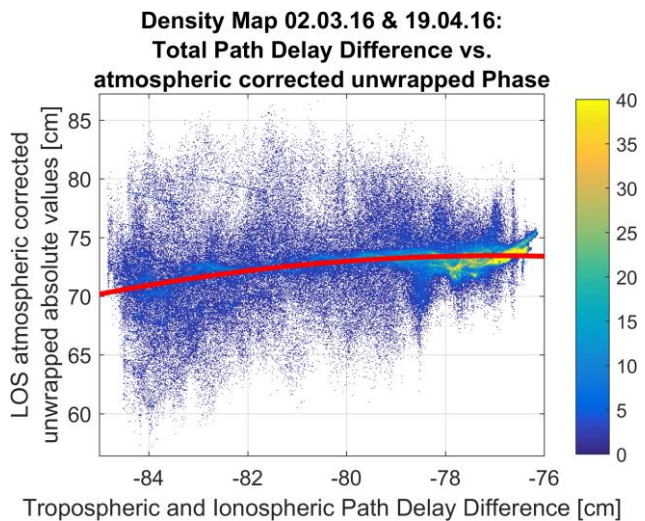


Figure 45: Density map based on the total APD difference and the atmospheric corrected DInSAR measurement with the APD of pair Two.

Also for this case, a second statistical approach (figures 44 & 45) was performed. This output shows significant improvement of the DInSAR measurement and it can be said that this method effectively mitigated the atmospheric artefacts. Both statistical results of pair Two showed less efficient performance of the used methods. Overall, in this chapter the results of the performed method were presented and the outputs were satisfying, even though some geological structures could not be removed effectively and pair Two behaved not as well as pair One. Given that, there was no surface displacement in the interferograms, the atmospheric signatures have been largely mitigated. The reason for the mentioned ineffectiveness is discussed in the next section.

6. Discussion

In this section, the obtained and relevant results corresponding to the research question are discussed and correlated with existing research literature. Sources of uncertainties are outlined and debated.

« Das, wobei unsere Berechnungen versagen, nennen wir Zufall. »

Albert Einstein (1879 – 1955)

6.1. Phase to elevation relationship

The DInSAR results demonstrated a decent initial position to perform the APD mitigation. The stratified tropospheric layers gave useful insight of the phase behaviour. The results presented a phase to elevation relationship, that is mainly caused by the tropospheric layer, with respect to the near surface relative humidity. This relationship is also indicated by tables 9 & 10, where the lower troposphere induced a higher delay than the top of the volcano. It was expected that from 0 to 500m the most total path delay difference occurred, which in this case was achieved. The variation of the atmospheric variables measured over the whole period (figures 16-20), was proved by the pixel wise APD estimation in figure 15. It is to assume that water vapour resp. the relative humidity is elevation dependent, which results in a phase to elevation relationship. Doin et al. (2009) stated that working with meteorological data in combination with InSAR/DInSAR is more sensitive in the path delay analysis than working with GPS, like the findings of Wadge et al. (2002) and Li et al., (2003; 2005).

The results of this thesis showed significant improvement of the DInSAR measurement as the phase dependency on elevation was “flattened”, furthermore it can be said that this method effectively mitigated the atmospheric artefacts, especially the troposphere-induced effect causing the phase elevation dependency was almost fully mitigated. Doin et al. (2009) stated that the accuracy of InSAR/DInSAR phase measurements are mainly limited by the tropospheric layer and correlates with the topography. Doin et al. (2009) demonstrated by neglecting the surface displacement that the InSAR showed a phase to elevation relationship, as the meteorological data, therefore a mitigation of atmospheric effects was performed.

The used technique in this study and the mitigation method could be implemented in further research studies or even be applied into an Earth Observation software to mitigate the atmospheric effects on the InSAR/DInSAR cases. This automatization would require a faster processing time in providing the meteorological data of ECMWF, as currently the data take three months before publishing to the end-users.

6.2. DInSAR Phase consistency of displacement and noisy effects

Interferometry and differential interferometry are unique tools for detecting ground movements. A pixel of a SAR image varies its phase due to the atmospheric variation, the spatial baseline, like the temporal change of a specific target in this area or the relative position of the satellite scatterer (Massonnet and Feigl, 1995; Ferretti et al., 2001). Regarding these decorrelation factors, it can be said, that in general, InSAR and DInSAR gave a good impression measuring displacement in regions of high coherence at the volcano. The evaluation of the parameters spatial and temporal baselines were of importance to ensure a relatively high coherence. In the case of *Piton de la Fournaise*, the measured and observed pixels showed a noisy phase and with high and low coherence sections distributed over the volcanic scene. The S6 acquisitions and the processed pairs feature several sources of errors and noise. Large time intervals between of 36 days, resp. 48 days created temporal decorrelation which reduced the coherence (Hanssen, 2002; Woodhouse, 2005; Ferretti et al., 2007). Especially in a volcanic region where the soil is fertile and ground is heavily moving there is often as a result a loss of coherence and no measurement is even possible to isolate the atmospheric effects. Due to strong vegetation at the foothills of the volcano, the scattering properties changed in time, based on the vegetation movement, leading to a loss of interferometric coherence (Zebker and Villasenor, 1992; Perski, 1998). The spatial baseline was a valuable parameter to distinguish the amount of coherence. Due to the precise orbit of the platform of S1A the baselines were accurately known in this thesis (pair One: 69.45m & pair Two: 39.85m), leading to better results in the coregistration. These values are suitable for the DInSAR approach. The spatial baseline should be as small as possible to determine surface displacement with little baseline-induced topographic phase. Small baseline values also increased the coherence. But in this case a small baseline was requested to minimize the occurrence of noise.

There was the risk, that the volcano was in movement even though no significant eruption is going on. As the eruptive periods were estimated, there was still the possibility that *Piton de la Fournaise* was moving due to inner magma movements, caused by breathing, showing deflation, inflating, flank eruptions and small lava streams, causing low coherence (Segall, 2010; Velez et al., 2011; Baker and Amelung, 2012; González et al., 2015). Both pairs showed on the southern part a flank eruption and eastern part a small lava outlet, although *Piton de la Fournaise* was in a restful period. The lava flow did not affect the coherence in both pairs. The eruptive southern flank was visible in both pairs, only pair Two suffered from decent low coherence on this volcanic area. These movements were not accounted as eruption by the *Institute de Physique du Globe de Paris*, but could influence the DInSAR measurement. Therefore, the isolation of the atmosphere was at risk. Minor issues which contribute to decorrelation in the case of repeat-pass Interferometry like satellite clock errors, phase errors due to thermal noise, baseline errors, false focusing, DEM errors, geometric decorrelation and image disintegration were neglected more (Rosen et al., 1996; Ferretti et al., 2001).

Phase unwrapping with SNAP/SNAPHU software caused during the processing many problems. When the unwrapping field was interpolated, sometimes the unwrapping operator was not accurate and not stable, possibilities of jumping created wrong and impractical results. Often the entire SAR modelling in SNAP needed to be reprocessed. In the beginning of processing the whole SAR acquisition scene was processed, leading to even larger unwrapping misleading results, as the entire area of the SAR acquisition is covered in vegetation. Vegetation often caused wholes in SNAP, leading to unwrapping problems in SNAP/SNAPHU and affected the entire result. Values were interpolated by the unwrapping operator, causing value jumps during unwrapping. More and more the SAR acquisition scene was cropped to the current volcanic scene, reducing the error source of unwrapping problems. Overall the DInSAR outputs of SNAP/SNAPHU led after successful processing to reliable and credible results.

6.3. Validation and processing of the atmospheric data

As the atmosphere showed a higher index of refraction than free space, the velocity is lowered, therefore the atmospheric phase delay effects can contaminate the outputs and lead to spurious phase variations, especially based on the geological structure of a volcano. The interferogram might show some serious atmospheric artefacts, as the tropospheric thickness is inversely related to the elevation of a volcano (Hooper et al., 2004; Perski, 1998; Jung et al., 2014). Therefore, the variation of the meteorological conditions of the two (four) SLCs must be taken into account when processing. Therefore, the estimation for the APD was important, indeed crucial.

In this thesis an estimation of the APD was performed. ERA-Interim was used to model the tropospheric layer. The data provided showed similar results compared to the meteorological station *St. Denis Gillot* at the Airport of *La Réunion*. Although the relative humidity correlated only 50% to the values corresponding value of ERA-Interim. The other meteorological data were well correlated. In case of estimating the tropospheric PD there might be several sources of errors. To dig further into this topic, figure 13 needed to be studied. ERA-Interim daily provided for these shown nine raster points the requested meteorological data, but the SLC image of the volcanic study site does not quite cover whole of the island. Thus it appears that the used meteorological data covered more than the exact volcano area. Therefore, three different approaches were performed, evaluating how many meteorological data raster points of ERA-Interim should be used to obtain a valid meteorological estimation. Three approaches with 20, 9 and 1 raster point were compared to see, if a spatial meteorological difference on the island were observed. The measured variance was insignificant, therefore, all approaches were taken to be valid options for gathering valid meteorological data. Different and more complex averaging methods could have been performed, by using a DEM to interpolate the nine raster point values.

The output of the varying tropospheric path delay in this study behaved similar to the findings in the paper of Zebker et al. (1997), where the phase delay caused by the atmosphere can produce 10-14cm errors in displacement measurements given spatial and temporal change of 20% in relative humidity. Massonnet et al. (1995) said that the path delays caused by the ionosphere and troposphere can't be separated from the effect of topography and displacement (Massonnet and Feigl, 1995; Emdarson et al., 2003; Delacourt et al., 1998; Ding et al., 2008). Tarayre and Massonnet (1996) showed that interferometric fringes correlate with the topography in a region where no ground displacement occurred during the SAR acquisitions. The paper of Doin et al. (2009) proposed to include the hydrostatic delay, when surface temperature varied by more than an annual 10°C span, which was also performed in this thesis.

In this thesis, the cloud coverage of ERA-Interim was calculated but not applied on the APD. But the corresponding parameter of water vapour in figure 18 was used to calculate the relative humidity which gave the assumption that cloud cover was high. To prove this, figures 16-20 presented the climatic condition of the three chosen SAR acquisition. Especially the cloud cover and the water vapour on the 02.03.2016 (master SLC) were high and the atmospheric pressure showed a suitable separation to acquisition date in April (slaves). This indicated a large variation in tropospheric path delay behaviour. The fact that *Piton de la Fournaise* holding the world record for the heaviest and most rainfall during a 12/72/96-hour period and January to March are the wettest periods, there might be a certain type of clouds, that influence the tropospheric path delay. Therefore, prognosis and diagnosis of ERA-Interim modelled climate and meteorological data were useful for obtaining satisfying and reliable result of the water vapour field, as the occurrence of clouds is based on the availability of the water vapour in the atmosphere (Albert et al., 2001). The ionosphere was estimated by using the TEC values from the two-hourly GIMs. In the case of the ionospheric PD calculation, the values were calculated by the CODE and needed to be trusted. At the end, it appeared that the ERA-Interim atmospheric variables provided a suitable prediction and in combination with the RSL APD mitigation model it led to useful results.

6.4. Three-dimensional DInSAR approach

Conventional InSAR methodology considers the objects and surface displacements in line of sight (LOS), therefore it was almost impossible to demonstrate a three-dimensional surface movement. The fact that the satellites flight orbit is directed from north to south and the LOS is east-west oriented, complicated a 3D displacement map (Grandin et al., 2016). Also interferograms with different angles of sights cannot provide a suited solution for a 3D shaping. The applied SLC in this thesis containing an ascending acquisition geometry where the east-west components were mostly measured. The north-south displacement direction cannot be well distinguished, based on the across-track acquisition mode of S1A (Wright, 2004). Hence, the calculated results of the DInSAR measurements were in LOS of the satellite viewing position and the displacement field cannot be resituated solely of this direction.

Ascending and descending SLC data can be processed to obtain the north-south displacement direction, however the surface displacement need to exceed a displacement rate of more than one meter, this was on the *Piton de la Fournaise* not the case (Fialko et al., 2001). The Scientific Data Hub provided acquisitions in descending Stripmap mode S4, these could have been applied for verification reason, if the results were similar in sense of coherence and displacement estimation and for modelling a 3D displacement field. In addition, volcanoes are multi complex systems that should to be considered individually. Volcanoes differ in their internal structure, magma composition outbreak cycles and geographic location. Mainly the surface displacement of volcanoes is based on the inner magma movements (Mogi, 1958; Segall, 2010). In addition to the LOS aspects, a physical approach by regarding and implementing a model to calculate the pressure change of the spherical and ellipsoidal magma chamber and its magmatic pipes and conduits to better understand and estimate the surface movement. Also the pre- and post-viscoelastic relaxation around the magma chambers needs to be considered when observing a volcano (Segall, 2010). Hence, the magmatic transport process could be identified and described in the interior of the volcano. Moreover, a 3D approach requires also an improvement of the single LOS estimation and calculation of the pixel wise APD with a Multi-LOS computation.

7. Conclusion

The results of this thesis illustrate the detection of surface displacements of *Piton de la Fournaise* by performing a DInSAR approach. In order to give acceptable response to research questions, the performed methods of mitigating DInSAR measurements by an APD estimation and correction is valid under the following hypotheses: that the atmospheric conditions are not the same, as it is based on a repeat-pass platform, therefore a difference of the atmospheric variability is given, and second no major surface displacement took place in this period, even a volcano is permanently active and moving unless the structure is extinct (Sarti et al., 1999). Revisiting the research questions, a conclusion was performed.

« Which components of the atmosphere control the electromagnetic waves emitted of satellite-based SAR systems in the repeat-pass mode as Sentinel-1A Stripmap mode S6? »

The results of this study illustrate that the solar dependent ionospheric and meteorological related tropospheric layer had significant effects on electromagnetic waves traversing the atmosphere. It is well known that propagating waves, like amplitudes and phases, fluctuate and vary in time and space. These effects modifies the electromagnetic waves velocity (Tarayre and Massonnet, 1996; Sarti et al., 1999; Hanssen, 1999; Merryman Boncori, 2006; Balaji, 2011). Especially in this case with a repeat-pass space-borne SAR system, the troposphere and the ionosphere affected the fluctuation of altering energy distribution, skewness, kurtosis, broadening pulse width and first and most notably of arrival time. Working with Stripmap mode 6 offered a shallow angle, thus the signal had one of the longest travelling time through the atmospheric layers. This maximised the encountered atmospheric path delay in contrast to steeper angles. The climate of the island also played an important role based on the large precipitation value that this area exhibited, leading to further maximisation of the path delay. In the context of repeat-pass InSAR measurement, the phase difference was a more serious problem, because the two rays must pass through completely different propagation media at different times, depending on the revisit times of the sensor (Li, 2005; Schubert et al., 2015).

« How strong and with which magnitude do the atmospheric dishomogeneities affect the interferometric phase signal on a tropical island as La Réunion ? »

The ionosphere is a multi-layered medium, which is not static and can change over time and space. The solar ultraviolet radiation creates free electrons in the ionosphere. If solar winds brings high-energy electrons into the ionosphere, the electron density will increase. The free electronic density varies based on the solar activity and leads to a change of the refraction index. Minor errors and signal delays induced by the ionosphere are dispersion, group delay, phase shifts and Faraday rotation. The sum of these error sources caused artefacts, that were on large scale in SAR scenes and therefore the variability was temporally non-abrupt and homogeneous. The TEC maps confirmed the stable and not high dependent ionospheric induced effects. Over the island of *La Réunion* the ionospheric path delays were confirmed as stable.

Most of the tropospheric path delay typically occurs in the lower part of the troposphere and depends on the atmospheric pressure, humidity (water vapour) and temperature. The troposphere modulates the refractive index of the propagating wave. Large tropospheric path delays were due to the rainy season from January to March. At *Piton de la Fournaise* the vertical stratification was observed particularly over high topographic structures such as mountains and volcanos, due to the variable tropospheric path length and the correspondent local water vapour induced by the topography. Measuring the tropospheric APD over island the of *La Réunion* indicated a strong height dependency, for which a correction method was formulated to mitigate this dependency.

A pixel wise APD was modelled based on parameters such as atmospheric pressure, humidity (water vapour) and temperature. ERA-Interim provided in-situ meteorological data for the acquisition dates to receive estimate the APD variation across the volcanic scene. Finally, the total APD difference measurements of 02.03.2016 & 07.04.2016 and 02.03.2016 & 19.04.2016 revealed that the ionospheric path delay is 9.2 times higher, respectively 5.1 times higher. What was more interesting was the fact that the high variation of ionosphere-induced effect, which was around 1%, compared to the high variability of approximately 40% induced by the troposphere-induced effects. Although the ionospheric path delay effects were higher, a more important role played the high varying troposphere in the interferometry, leading to a remarkably height-dependency over the observed volcano.

« What are the methods to estimate and correct the atmospheric effects on different SAR interferograms in the case of a volcanic scenario, and does the correction properly mitigate for atmospheric effects? »

The interferometric measurements derived with the DInSAR approach were applied with the computed total APD difference for a pixel wise mitigation. The results demonstrate that the tropospheric and ionosphere-induced effects on the interferometric measurement need to be taken into account and should be corrected. The mitigation method succeeded in reducing the height dependency caused mainly by the tropospheric wet delay. The phase delay mitigation can be performed by using a non-linear dependence to the volcanic study site by implementing meteorological data of ERA-Interim. This used pixel wise APD mitigation method largely corrected the height-dependency induced by the troposphere.

This thesis and the numerous mentioned studies revealed the tropospheric and ionospheric effects on interferometry. Various approaches have been made to analyse the atmospheric induces effects and proposed a mitigation method for the interferometric measurements. The computation of a comprehensive and standardised correction method to mitigate the atmospheric contribution is still a challenge. Some drawbacks were found, like minor side eruptions or potentially deflation or inflation based on the inner magma movements of the volcanic structure that could lead to a surface displacement, which have to be avoided to completely isolate the atmospheric behaviour. At the end, it appeared that the ERA-Interim provided suitably prediction of atmospheric variables on micro-scale and in combination with the RSL APD mitigation model, this approach led to useful DInSAR improvements.

Finally, in nature there are many external factors that influence the electromagnetic wave, but the attempt to be able to relatively correct and improve the interferometric products of S1A, by successfully applying an atmospheric correction APD method, demonstrated that the research of technology and product development of interferometry is a step closer to reality.

8. Outlook

In retrospect, SAR interferometry drastically improved from its algorithm to the estimation of the signal of interest. The computing time and the source of error were reduced to produce suited results with a high value of information. The era of near real-time monitoring program has arrived, especially by the time Sentinel 1C/1D are fully in service, shorter temporal baseline and fast computation lead to an improvement of the observation possibility (Emardson et al., 2003). The accessibility to the decision makers and end users were already established, for example by the Scientific Data Hub for Sentinel data (Ferretti et al., 2015). The availability of data is strongly improving by cloud computing. As the information sources are expanding and growing, there is a need of faster processing and distributed computing to serve the demanding users for monitoring the Earth.

Working with the Sentinel platform does not mean to be working restrictively with one single platform for interferometric computation. The future is offering new possibilities in combining different satellite to work as a constellation, for example to feature S1A/B/C/D (CSAR) and COSMO-SkyMed (XSAR). At first sight this might be useless based on the different wavelength and orbits, nevertheless, interferometric displacement measurements could be performed, whenever the incidence angle do not differ significantly (just a few degrees). Therefore, a combination of different platforms can create a virtual data constellation. This synergy might lead to create an efficient and effective monitoring tool. Regarding a total breakdown or a temporary failure of a satellite, this monitoring scheme could be extremely promising for bypassing in times where the data flow must be preserved, in case of emergency response and continuous monitoring (Emardson et al., 2003; Sansosti et al., 2015; Ferretti et al., 2015).

SAR systems on geostationary and geosynchronous orbits give raise for auspicious monitoring approaches (Ruiz Rodon et al., 2013). In the case of a geostationary orbit, the distant to the earth can lead to spread loss, this could be solved by a higher integration time, though leading to a drawback in resolution. Monti Guarnieri et al. (2015) proposed for the mentioned disadvantage already a solution that is around the corner by launching a swarm of numerous microsattellites to reduce the integration time (Monti Guarnieri et al., 2015; Sansosti et al., 2015).

In addition, a new volcano monitoring tool called RapidSAR (FutureVolc Project) brings an algorithm for handling high volumes of data of the modern SAR platforms including S1A/B/C/D and is effective on small baseline time series. This tool created a high SNR for surface displacement mapping, leading to a quick processing time, estimating the modelled coherence and identifying a necessary amount of high coherence point for suitable surface displacement monitoring, complimentary linking to the PSI approach (Ferretti et al., 2000; Hooper et al., 2004; Crosetto et al., 2009; Costantini et al., 2016; Spaans and Hooper, 2016). In general, a more efficient and effective phase unwrapping algorithm might overcome a larger temporal baseline (Spaans and Hooper, 2016). Besides this, the 3D Interferometry might be implemented on the next generation SAR platforms. These different and innovative acquisition modes as the high promising bidirectional SAR as the MAI or the SuperSAR could bring an 3D evolution into the Interferometry era (Bechor and Zebker, 2006; Jung et al., 2009; Grandin, 2015; Grandin et al., 2016; Jung et al., 2015).

Concerning the meteorological data sources, a faster and spatial higher resolution platform should be established to deliver near-real time data, which could be applied to an atmosphere mitigation method, leading to a more convenient and user-friendly data environment.

As shown, the future of SAR Interferometry is promising and regarding the atmospheric correction methods, it should be stated that, rapid processing, cloud services and more data sources could lead to a better connectivity between the different aspects and open even more possibilities to quantify and mitigate the atmosphere-induced effects on Interferometry.

Bibliography

- Afraimovich, E.L., Pirog, O.M., & Terekhov, A.I. (1992). Diagnostics of large-scale structures of the high-latitude ionosphere based on tomographic treatment of navigation-satellite signals and of data from ionospheric stations. *Journal of Atmospheric and Terrestrial Physics*, *54*, 1265–1273.
- Albert, P., Bennartz, R., & Fischer, J. (2001). Remote Sensing of Atmospheric Water Vapor from Backscattered Sunlight in Cloudy Atmospheres. *Journal of Atmospheric and Oceanic Technology*, *18*, 865–874.
- Allen, C.T. (1995). Interferometric synthetic aperture radar. *IEEE Geoscience and Remote Sensing Society Newsletter*, *96*, 6–13.
- Amelung, F., Jónsson, S., Zebker, H., & Segall, P. (2000). Widespread uplift and ‘trapdoor’ faulting on Galapagos volcanoes observed with radar interferometry. *Nature*, *407*, 993–996.
- Askne, J., & Nordius, H. (1987). Estimation of tropospheric delay for microwaves from surface weather data. *Radio Science*, *22*, 379–386.
- Baby, B., Golé, P., & Lavergnat, J. (1988). A model for the tropospheric excess path length of radio waves from surface meteorological measurements. *Radio Science*, *23*, 1023–1038.
- Bachèlery, P., Lénat, J.-F., Di Muro, A., & Michon, L. (Eds.) (2016). Active volcanoes of the Southwest Indian Ocean. Piton de la Fournaise and Karthala. Heidelberg, New York, Dordrecht, London: Springer.
- Baker, S., & Amelung, F. (2012). Top-down inflation and deflation at the summit of Kīlauea Volcano, Hawai‘i observed with InSAR. *Journal of Geophysical Research: Solid Earth*, *117*, n/a-n/a.
- Balaji, P.M. (2011). Estimation and Correction of Tropospheric and Ionospheric Effects on Differential SAR Interferograms. *Unpublished M. Sc. Dissertation, ITC, The Netherlands*. 72p.
- Bamler, R., & Philipp Hartl (1998). Synthetic aperture radar interferometry. *Inverse Problems*, *14*. <http://stacks.iop.org/0266-5611/14/i=4/a=001>.
- Beach, T.L., & Kintner, P.M. (2001). Development and use of a GPS ionospheric scintillation monitor. *IEEE Transactions on Geoscience and Remote Sensing*, *39*, 918–928.
- Beauducel, F., Briole, P., & Froger, J.-L. (2000). Volcano-wide fringes in ERS synthetic aperture radar interferograms of Etna (1992-1998). Deformation or tropospheric effect? *Journal of Geophysical Research: Solid Earth*, *105*, 16391–16402.
- Bechor, N.B.D., & Zebker, H.A. (2006). Measuring two-dimensional movements using a single InSAR pair. *Geophysical Research Letters*, *33*.
- Berardino, P., Fornaro, G., Lanari, R., & Sansosti, E. (2002). A new algorithm for surface deformation monitoring based on small baseline differential SAR interferograms. *IEEE Transactions on Geoscience and Remote Sensing*, *40*, 2375–2383.
- Bilow, H.J. (1984). Propagation and Scattering Considerations for the 0.2-3.0 GHz Frequency Range for a Space-Based Radar. DTIC Document.
- Bonforte, A., Ferretti, A., Prati, C., Puglisi, G., & Rocca, F. (2001). Calibration of atmospheric effects on SAR interferograms by GPS and local atmosphere models. First results. *Journal of Atmospheric and Solar-Terrestrial Physics*, *63*, 1343–1357.
- Briole, P., Massonnet, D., & Delacourt, C. (1997). Post-eruptive deformation associated with the 1986-87 and 1989 lava flows of Etna detected by radar interferometry. *Geophysical Research Letters*, *24*, 37–40.
- Buck, A.L. (1981). New Equations for Computing Vapour Pressure and Enhancement Factor. *Journal of Applied Meteorology*, *20*, 1527–1532.
- Budden, K.G. (1961). *The wave-guide mode theory of wave propagation*: Logos Press.
- Cavalié, O., Doin, M.-P., Lasserre, C., & Briole, P. (2007). Ground motion measurement in the Lake Mead area, Nevada, by differential synthetic aperture radar interferometry time series analysis. Probing the lithosphere rheological structure. *Journal of Geophysical Research*, *112*.

- Chen, C.W., & Zebker, H.A. (2001). Two-dimensional phase unwrapping with use of statistical models for cost functions in nonlinear optimization. *Journal of the Optical Society of America A*, 18, 338.
- Climat et Hydrologie Etude climatique.
<http://hmf.enseeiht.fr/travaux/CD9598/travaux/optsee/bei/nome41/n41p03.htm>.
- Costantini, F., Mouratidis, A., Schiavon, G., & Sarti, F. (2016). Advanced InSAR techniques for deformation studies and for simulating the PS-assisted calibration procedure of Sentinel-1 data. Case study from Thessaloniki (Greece), based on the Envisat/ASAR archive. *International Journal of Remote Sensing*, 37, 729–744.
- Costantini, M. (1998). A novel phase unwrapping method based on network programming. *IEEE Transactions on Geoscience and Remote Sensing*, 36, 813–821.
- Crosetto, M. (2002). Calibration and validation of SAR interferometry for DEM generation. *ISPRS Journal of Photogrammetry and Remote Sensing*, 57, 213–227.
- Crosetto, M., Crippa, B., Biescas, E., Monserrat, O., Agudo, M., & Fernández, P. (2005). Land deformation measurement using SAR interferometry: state-of-the-art. *Photogrammetrie Fernerkundung Geoinformation*, 2005, 497.
- Crosetto, M., Monserrat, O., Jungner, A., & Crippa, B. (2009). Persistent scatterer interferometry: Potentials and limits. *Proceedings of the ISPRS Hannover Workshop 2009 High-Resolution Earth Imaging for Geospatial Information*.
- Curlander, J.C., & McDonough, R.N. (1991). *Synthetic aperture radar*: John Wiley & Sons New York, NY, USA.
- Dana, P.H. (1997). Global Positioning System (GPS) Time Dissemination for Real-Time Applications. *Real-Time Systems*, 12, 9–40.
- Danklmayer, A., Doring, B.J., Schwerdt, M., & Chandra, M. (2009). Assessment of Atmospheric Propagation Effects in SAR Images. *IEEE Transactions on Geoscience and Remote Sensing*, 47, 3507–3518.
- Davies, K., & Smith, E.K. (2002). Ionospheric effects on satellite land mobile systems. *IEEE Antennas and Propagation Magazine*, 44, 24–31.
- Delacourt, C., Briole, P., & Achache, J.A. (1998). Tropospheric corrections of SAR interferograms with strong topography. Application to Etna. *Geophysical Research Letters*, 25, 2849–2852.
- Ding, X., Li, Z., Zhu, J., Feng, G., & Long, J. (2008). Atmospheric Effects on InSAR Measurements and Their Mitigation. *Sensors*, 8, 5426–5448.
- Dodson, A.H., Shardlow, P.J., Hubbard, L.C.M., Elgered, G., & Jarlemark, P.O.J. (1996). Wet tropospheric effects on precise relative GPS height determination. *Journal of Geodesy*, 70, 188–202.
- Doin, M.-P., Lasserre, C., Peltzer, G., Cavalié, O., & Doubre, C. (2009). Corrections of stratified tropospheric delays in SAR interferometry. Validation with global atmospheric models. *Journal of Applied Geophysics*, 69, 35–50.
- Ducret, G. (2013). *Mesure de déformation par interférométrie radar: développements méthodologiques et applications à la subduction chilienne*.
- Dzurisin, D. (2007). *Volcano deformation. Geodetic monitoring techniques*. Berlin, New York, Chichester, UK: Springer; Praxis.
- ECMWF Landingpage. <http://www.ecmwf.int/>.
- ECMWF near-surface humidity. <http://www.ecmwf.int/en/does-era-40-dataset-contain-near-surface-humidity-data>.
- ECMWF Part IV: Physical Processes. <http://www.ecmwf.int/en/elibrary/9211-part-iv-physical-processes>.

- Elliott, J.R., Biggs, J., Parsons, B., & Wright, T.J. (2008). InSAR slip rate determination on the Altyn Tagh Fault, northern Tibet, in the presence of topographically correlated atmospheric delays. *Geophysical Research Letters*, *35*, n/a-n/a.
- Emardson, T.R., Simons, M., & Webb, F.H. (2003). Neutral atmospheric delay in interferometric synthetic aperture radar applications. Statistical description and mitigation. *Journal of Geophysical Research: Solid Earth*, *108*.
- ERA-Interim Daily. <http://apps.ecmwf.int/datasets/data/interim-full-daily/levtype=sfc/>.
- ESA Galileo Tropospheric Correction Model. http://www.navipedia.net/index.php/Galileo_Tropospheric_Correction_Model.
- ESA Sentinel-1 SAR Revisit and Coverage. <https://sentinel.esa.int/web/sentinel/user-guides/sentinel-1-sar/revisit-and-coverage>.
- ESA Sentinel-1 SAR Level-1. <https://sentinel.esa.int/web/sentinel/user-guides/sentinel-1-sar/product-types-processing-levels/level-1>.
- ESA Sentinel-1 SAR Overview. <https://sentinel.esa.int/web/sentinel/user-guides/sentinel-1-sar/overview>.
- ESA Sentinel-1 SAR Stripmap. <https://sentinel.esa.int/web/sentinel/user-guides/sentinel-1-sar/acquisition-modes/stripmap>.
- ESA Sentinel-1A & Sentinel-1B delivers. http://www.esa.int/Our_Activities/Observing_the_Earth/Copernicus/Sentinel-1/Sentinel-1B_delivers.
- ESA Sentinels Scientific Data Hub. <https://scihub.copernicus.eu/dhus/>.
- Essen, L., & Froome, K.D. (1951). The Refractive Indices and Dielectric Constants of Air and its Principal Constituents at 24,000 Mc/s. *Proceedings of the Physical Society. Section B*, *64*, 862.
- Farrell, W.E. (1972). Deformation of the Earth by surface loads. *Reviews of Geophysics*, *10*, 761.
- Ferretti, A., Colombo, D., Fumagalli, A., Novali, F., & Rucci, A. (2015). InSAR data for monitoring land subsidence. Time to think big. *Proceedings of the International Association of Hydrological Sciences*, *372*, 331–334.
- Ferretti, A., Monti-Guarnieri, A., Prati, C., Rocca, F., & Massonet, D. (2007). *InSAR principles-guidelines for SAR interferometry processing and interpretation*.
- Ferretti, A., Prati, C., & Rocca, F. (2000). Nonlinear subsidence rate estimation using permanent scatterers in differential SAR interferometry. *IEEE Transactions on Geoscience and Remote Sensing*, *38*, 2202–2212.
- Ferretti, A., Prati, C., & Rocca, F. (2001). Permanent scatterers in SAR interferometry. *IEEE Transactions on Geoscience and Remote Sensing*, *39*, 8–20.
- Fialko, Y., Simons, M., & Agnew, D. (2001). The complete (3-D) surface displacement field in the epicentral area of the 1999 M W 7.1 Hector Mine Earthquake, California, from space geodetic observations. *Geophysical Research Letters*, *28*, 3063–3066.
- Fletcher, K. (2012). *Sentinel-1: ESA's Radar Observatory Mission for GMES Operational Services*. Agence spatiale européenne; ESA communications.
- Franceschetti, G., & Lanari, R. (1999). *Synthetic aperture radar processing*: CRC Press.
- Freeman, A., & Saatchi, S.S. (1997). Effects of Faraday rotation on backscatter signatures in SAR image data. In H. Mott, & W.-M. Boerner (Eds.), *Optical Science, Engineering and Instrumentation '97* (pp. 37–44): SPIE.
- Fruneau, B., Deffontaines, B., Rudant, J.-P., & Le Parmentier, A.-M. (2005). Monitoring vertical deformation due to water pumping in the city of Paris (France) with differential interferometry. *Comptes Rendus Geoscience*, *337*, 1173–1183.
- Gens, R., & van Genderen, J.L. (2007). Review Article SAR interferometry—issues, techniques, applications. *International Journal of Remote Sensing*, *17*, 1803–1835.

- Ghiglia, D.C., & Pritt, M.D. (1998). *Two-dimensional phase unwrapping: theory, algorithms, and software*: Wiley New York.
- Global Volcanism Program Piton de la Fournaise. <http://volcano.si.edu/volcano.cfm?vn=233020>.
- Goldstein, R. (1995). Atmospheric limitations to repeat-track radar interferometry. *Geophysical research letters*, 22, 2517.
- Goldstein, R.M., & Werner, C.L. (1998). Radar interferogram filtering for geophysical applications. *Geophysical Research Letters*, 25, 4035–4038.
- Gonzalez, P.J., Marinkovic, P., Samsonov, S., Hooper, A., Larsen, Y., & Wright, T. (2015). Sentinel-1 TOPS interferometry for geophysical applications: Dyke intrusion imaged during 2014 Pico do Fogo eruption. In *EGU General Assembly Conference Abstracts* (p. 13194).
- González, P.J., Bagnardi, M., Hooper, A.J., Larsen, Y., Marinkovic, P., Samsonov, S.V., & Wright, T.J. (2015). The 2014–2015 eruption of Fogo volcano. Geodetic modeling of Sentinel-1 TOPS interferometry. *Geophysical Research Letters*, 42, 9239–9246.
- Grandin, R. (2015). Interferometric processing of SLC Sentinel-1 TOPS data. In *Proceedings of the 2015 ESA Fringe workshop, ESA Special Publication, SP*.
- Grandin, R., Klein, E., Métois, M., & Vigny, C. (2016). Three-dimensional displacement field of the 2015 Mw 8.3 Illapel earthquake (Chile) from across- and along-track Sentinel-1 TOPS interferometry. *Geophysical Research Letters*, 43, 2552–2561.
- Gupta, R.P. (2013). *Remote sensing geology*: Springer Science & Business Media.
- Hanssen, R., & Feijt, A. (1997). A first quantitative evaluation of atmospheric effects on SAR interferometry. In *ERS SAR Interferometry* (p. 277).
- Hanssen, R., Moiseev, D., & Businger, S. (2003). Resolving the acquisition ambiguity for atmospheric monitoring in multi-pass radar interferometry. In *IGARSS 2003. 2003 IEEE International Geoscience and Remote Sensing Symposium. Proceedings* (pp. 1202–1205).
- Hanssen, R.F. (1998). *Atmospheric heterogeneities in ERS tandem SAR interferometry*: Delft University Press.
- Hanssen, R.F. (1999). High-Resolution Water Vapor Mapping from Interferometric Radar Measurements. *Science*, 283, 1297–1299.
- Hanssen, R.F. (2002). *Radar Interferometry. Data Interpretation and Error Analysis*. Dordrecht: Kluwer Academic Publishers.
- Historical Weather St. Denis Gillot. <http://www.worldweatheronline.com/v2/historical-weather.aspx?q=-21.22,55.32>.
- Hooper, A., Zebker, H., Segall, P., & Kampes, B. (2004). A new method for measuring deformation on volcanoes and other natural terrains using InSAR persistent scatterers. *Geophysical Research Letters*, 31.
- Hooper, A., Bekaert, D., Spaans, K., & Arikan, M. (2012). Recent advances in SAR interferometry time series analysis for measuring crustal deformation. *Tectonophysics*, 514-517, 1–13.
- Hopfield, H.S. (1969). Two-quartic tropospheric refractivity profile for correcting satellite data. *Journal of Geophysical Research*, 74, 4487–4499.
- Interactive Map of Active Volcanoes and recent Earthquakes world-wide. <http://earthquakes.volcanodiscovery.com/>.
- IPGP Bulletin les dernières actualités de l'observatoire. <http://www.ipgp.fr/fr/dernieres-actualites/344>.
- IPGP Le Piton de la Fournaise. <http://www.ipgp.fr/fr/ovpf/piton-de-fournaise>.
- IPGP Observatoire volcanologique du Piton de la Fournaise. <http://www.ipgp.fr/fr/ovpf/observatoire-volcanologique-piton-de-fournaise>.
- Ishimaru, A. (1978). *Wave propagation and scattering in random media*: Academic press New York.
- Janssen, V., Ge, L., & Rizos, C. (2004). Tropospheric corrections to SAR interferometry from GPS observations. *GPS Solutions*, 8, 140–151.

- Jarlemark, P.O.J., Emardson, T.R., & Johansson, J.M. (1998). Wet delay variability calculated from radiometric measurements and its role in space geodetic parameter estimation. *Radio Science*, 33, 719–730.
- Jehle, M., Perler, D., Small, D., Schubert, A., & Meier, E. (2008). Estimation of Atmospheric Path Delays in TerraSAR-X Data using Models vs. Measurements. *Sensors*, 8, 8479–8491.
- Jehle, M., Small, D., Meier, E., & Nüesch, D. (2004). Improved knowledge of SAR geometry through atmospheric modelling. In *Proc. EUSAR*.
- Johansson, J.M., Emardson, T.R., Jarlemark, P., Gradinarsky, L.P., & Elgered, G. (1998). The atmospheric influence on the results from the Swedish GPS network. *Physics and Chemistry of the Earth*, 23, 107–112.
- Jung, H.-S., Lu, Z., Shepherd, A., & Wright, T. (2015). Simulation of the SuperSAR Multi-Azimuth Synthetic Aperture Radar Imaging System for Precise Measurement of Three-Dimensional Earth Surface Displacement. *IEEE Transactions on Geoscience and Remote Sensing*, 53, 6196–6206.
- Jung, H.-S., Won, J.-S., & Kim, S.-W. (2009). An Improvement of the Performance of Multiple-Aperture SAR Interferometry (MAI). *IEEE Transactions on Geoscience and Remote Sensing*, 47, 2859–2869.
- Jung, J., Kim, D.J., & Park, S.-E. (2014). Correction of Atmospheric Phase Screen in Time Series InSAR Using WRF Model for Monitoring Volcanic Activities. *IEEE Transactions on Geoscience and Remote Sensing*, 52, 2678–2689.
- Kim, J.-W., Lu, Z., & Degrandpre, K. (2016). Ongoing Deformation of Sinkholes in Wink, Texas, Observed by Time-Series Sentinel-1A SAR Interferometry (Preliminary Results). *Remote Sensing*, 8, 313.
- Kim, Y., & van Zyl, J. (1998). Ionospheric effects on polarimetric and interferometric space-borne SAR. In *IGARSS '98. Sensing and Managing the Environment. 1998 IEEE International Geoscience and Remote Sensing Symposium Proceedings. (Cat. No.98CH36174) (472-474 vol.1)*.
- Koppel, K., Zalite, K., Sisas, A., Voormansik, K., Praks, J., & Noorma, M. (2015). Sentinel-1 for urban area monitoring — Analysing local-area statistics and interferometric coherence methods for buildings' detection. In *IGARSS 2015 - 2015 IEEE International Geoscience and Remote Sensing Symposium* (pp. 1175–1178).
- Kükenbrink, D. (2014). Biomass estimation from polarimetric L-band SAR data over Swiss temperate forests. Master's Thesis. Remote Sensing Laboratories, Department of Geography, University of Zürich.
- Lanari, R. (2015). From ERS-1 TO SENTINEL-1: A big data challenge for 25 years of DInSAR observations. In *IGARSS 2015 - 2015 IEEE International Geoscience and Remote Sensing Symposium* (pp. 1460–1463).
- Lanari, R., Berardino, P., Bonano, M., Casu, F., Luca, C. de, Elefante, S., Fusco, A., Manunta, M., Manzo, M., Ojha, C., Pepe, A., Sansosti, E., & Zinno, I. (2015). Sentinel-1 results: SBAS-DInSAR processing chain developments and land subsidence analysis. In *IGARSS 2015 - 2015 IEEE International Geoscience and Remote Sensing Symposium* (pp. 2836–2839).
- Lanari, R., Mora, O., Manunta, M., Mallorqui, J.J., Berardino, P., & Sansosti, E. (2004). A small-baseline approach for investigating deformations on full-resolution differential SAR interferograms. *IEEE Transactions on Geoscience and Remote Sensing*, 42, 1377–1386.
- Li, F.K., & Goldstein, R.M. (1990). Studies of multibaseline spaceborne interferometric synthetic aperture radars. *IEEE Transactions on Geoscience and Remote Sensing*, 28, 88–97.
- Li, Z. (2005). Correction of atmospheric water vapour effects on repeat-pass SAR interferometry using GPS, MODIS and MERIS data.
- Li, Z., Fielding, E.J., & Cross, P. (2009a). Integration of InSAR Time-Series Analysis and Water-Vapor Correction for Mapping Postseismic Motion After the 2003 Bam (Iran) Earthquake. *IEEE Transactions on Geoscience and Remote Sensing*, 47, 3220–3230.

- Li, Z., Fielding, E.J., Cross, P., & Preusker, R. (2009b). Advanced InSAR atmospheric correction. MERIS/MODIS combination and stacked water vapour models. *International Journal of Remote Sensing*, 30, 3343–3363.
- Li, Z., Muller, J., Cross, P., Albert, P., Fischer, J., & Bennartz, R. (2006). Assessment of the potential of MERIS near- infrared water vapour products to correct ASAR interferometric measurements. *International Journal of Remote Sensing*, 27, 349–365.
- Li, Z., Muller, J.-P., & Cross, P. (2003). Tropospheric correction techniques in repeat-pass SAR interferometry. In *Proceedings of the FRINGE 2003 workshop* (pp. 1–5).
- Li, Z.W., Ding, X.L., Huang, C., Zou, Z.R., & Chen, Y.L. (2007). Atmospheric effects on repeat-pass InSAR measurements over Shanghai region. *Journal of Atmospheric and Solar-Terrestrial Physics*, 69, 1344–1356.
- Libert, J. La Pluviométrie. <http://pedagogie2.ac-reunion.fr/cotamarp/calliopee/general/pluie.html>.
- Lohman, R.B., & Simons, M. (2005). Locations of selected small earthquakes in the Zagros mountains. *Geochemistry, Geophysics, Geosystems*, 6, n/a-n/a.
- Massonnet, D., Briole, P., & Arnaud, A. (1995). Deflation of Mount Etna monitored by spaceborne radar interferometry. *Nature*, 375, 567–570.
- Massonnet, D., & Feigl, K.L. (1995). Discrimination of geophysical phenomena in satellite radar interferograms. *Geophysical Research Letters*, 22, 1537–1540.
- Massonnet, D., & Feigl, K.L. (1998). Radar interferometry and its application to changes in the Earth's surface. *Reviews of Geophysics*, 36, 441–500.
- Massonnet, D., Feigl, K., Rossi, M., & Adragna, F. (1994). Radar interferometric mapping of deformation in the year. *Nature*, 369, 19.
- Massonnet, D., & Souyris, J.-C. (2008). *Imaging with synthetic aperture radar*: CRC Press.
- Mattar, K.E., & Gray, A.L. (2014). Reducing ionospheric electron density errors in satellite radar interferometry applications. *Canadian Journal of Remote Sensing*, 28, 593–600.
- Meier, E. (2013). Einführung in die Radar-Fernerkundung. Skript für GEO 371 und 443. Remote Sensing Laboratories, Department of Geography, University of Zürich.
- Merryman Boncori, J.P. (2006). ERROR MODELLING FOR SAR INTERFEROMETRY AND SIGNAL PROCESSING ISSUES RELATED TO THE USE OF AN ENCODING SAR TRANSPONDER. Ph.D. thesis. Faculty of Engineering.
- Mogi, K. (1958). Relations between the eruptions of various volcanoes and the deformations of the ground surfaces around them.
- Mohila, S. Lage und Klima von der Insel La Réunion. <https://www.reunion-urlaub.com/vor-der-reise/lage-klima/klima-und-reisezeit.html>.
- Monti Guarnieri, A., Broquetas, A., Recchia, A., Rocca, F., & Ruiz-Rodon, J. (2015). Advanced Radar Geosynchronous Observation System. ARGOS. *IEEE Geoscience and Remote Sensing Letters*, 12, 1406–1410.
- Mora, O., Mallorqui, J.J., & Broquetas, A. (2003). Linear and nonlinear terrain deformation maps from a reduced set of interferometric sar images. *IEEE Transactions on Geoscience and Remote Sensing*, 41, 2243–2253.
- Nagler, T., Rott, H., Hetzenecker, M., Wuite, J., & Potin, P. (2015). The Sentinel-1 Mission. New Opportunities for Ice Sheet Observations. *Remote Sensing*, 7, 9371–9389.
- National Centers for Environmental Information (NCEI). <http://www.ncdc.noaa.gov/cdo-web/datatools/findstation>.
- Peltzer, G., Crampé, F., Hensley, S., & Rosen, P. (2001). Transient strain accumulation and fault interaction in the Eastern California shear zone. *Geology*, 29, 975.
- Perski, Z. (1998). Applicability of ERS-1 and ERS-2 InSAR for land subsidence monitoring in the Silesian coal mining region, Poland. *International Archives of Photogrammetry and Remote Sensing*, 32, 555–558.

- Polcari, M. (2016). 3D displacement field retrieved by integrating Sentinel-1 InSAR and GPS data. The 2014 South Napa earthquake. *European Journal of Remote Sensing*, 1.
- Puysségur, B., Michel, R., & Avouac, J.-P. (2007). Tropospheric phase delay in interferometric synthetic aperture radar estimated from meteorological model and multispectral imagery. *Journal of Geophysical Research*, 112.
- Qing, X., Guowang, J., Caiying, Z., Zhengde, W., Yu, H., & Peizhang, Y. (2004). The Filtering and Phase Unwrapping of Interferogram. *Proc. ISPRS XXXV Comm VI/WG4*.
- Rees, G., & Rees, W.G. (2013). *Physical principles of remote sensing*: Cambridge University Press.
- Rosen, P.A., Hensley, S., Joughin, I.R., Li, F.K., Madsen, S.N., Rodriguez, E., & Goldstein, R.M. (2000). Synthetic aperture radar interferometry. *Proceedings of the IEEE*, 88, 333–382.
- Rosen, P.A., Hensley, S., Zebker, H.A., Webb, F.H., & Fielding, E.J. (1996). Surface deformation and coherence measurements of Kilauea Volcano, Hawaii, from SIR-C radar interferometry. *Journal of Geophysical Research: Planets*, 101, 23109–23125.
- Ruiz Rodon, J., Broquetas, A., Monti Guarnieri, A., & Rocca, F. (2013). Geosynchronous SAR Focusing With Atmospheric Phase Screen Retrieval and Compensation. *IEEE Transactions on Geoscience and Remote Sensing*, 51, 4397–4404.
- Saastamoinen, J. (1973). Contributions to the theory of atmospheric refraction. *Bulletin géodésique*, 107, 13–34.
- Sakar, N., Brcic, R., Gonzalez, F.R., & Yague-Martinez, N. (2015). An advanced co-registration method for TOPSAR interferometry. In *IGARSS 2015 - 2015 IEEE International Geoscience and Remote Sensing Symposium* (pp. 5240–5243).
- Salvi, S., Tolomei, C., Merryman Boncori, J.P., Pezzo, G., Atzori, S., Antonioli, A., Trasatti, E., Giuliani, R., Zoffoli, S., & Coletta, A. (2012). Activation of the SIGRIS monitoring system for ground deformation mapping during the Emilia 2012 seismic sequence, using COSMO-SkyMed InSAR data. *Annals of Geophysics*.
- Sansosti, E., Berardino, P., Bonano, M., Calò, F., Castaldo, R., Casu, F., Manunta, M., Manzo, M., Pepe, A., Pepe, S., Solaro, G., Tizzani, P., Zeni, G., & Lanari, R. (2014). How second generation SAR systems are impacting the analysis of ground deformation. *International Journal of Applied Earth Observation and Geoinformation*, 28, 1–11.
- Sansosti, E., Manunta, M., Casu, F., Bonano, M., Ojha, C., Marsella, M., & Lanari, R. (2015). Radar remote sensing from space for surface deformation analysis. Present and future opportunities from the new SAR sensor generation. *Rendiconti Lincei*, 26, 75–84.
- Sarti, F., Vadon, H., & Massonnet, D. (1999). A method for the automatic characterization of InSAR atmospheric artifacts by correlation of multiple interferograms over the same site.
- Schmidt, D.A. (2005). Distribution of aseismic slip rate on the Hayward fault inferred from seismic and geodetic data. *Journal of Geophysical Research*, 110.
- Schubert, A., & Small, D. (2016). Extended Sentinel-1 product annotations supporting enhanced accuracy geolocation. *VEGA Technical Note, Ref. UZH-S1-APD-TN-03*, Iss. 1.01, 15 Feb. 2016, 51.
- Schubert, A., Small, D., Miranda, N., Geudtner, D., & Meier, E. (2015). Sentinel-1A Product Geolocation Accuracy. Commissioning Phase Results. *Remote Sensing*, 7, 9431–9449.
- Secan, J.A., & Fremouw, E.J. (1988). Development of advanced ionospheric models in support of space-based radar design studies, phase I Rep. NWRA-CR-88-R022Northwest Res. Assoc., Inc., Bellevue, Wash.
- Segall, P. (2010). *Earthquake and volcano deformation*: Princeton University Press.
- Sheng, Y., Wang, Y., Ge, L., & Rizos, C. (2012). Differential radar interferometry and its application in monitoring underground coal mining induced subsidence, 227–232.
- Shimada, M. (2000). Correction of the satellite's state vector and the atmospheric excess path delay in SAR interferometry-application to surface deformation detection. In *IGARSS 2000. IEEE 2000*

- International Geoscience and Remote Sensing Symposium. Taking the Pulse of the Planet: The Role of Remote Sensing in Managing the Environment* (pp. 2236–2238).
- Shuttle Radar Topography Mission 1 Arc-Second Global. <https://lta.cr.usgs.gov/SRTM1Arc>.
- Sigmundsson, F., Hreinsdottir, S., Hooper, A., Arnadóttir, T., Pedersen, R., Roberts, M.J., Oskarsson, N., Auriac, A., Deciem, J., Einarsson, P., Geirsson, H., Hensch, M., Ofeigsson, B.G., Sturkell, E., Sveinbjornsson, H., & Feigl, K.L. (2010). Intrusion triggering of the 2010 Eyjafjallajökull explosive eruption. *Nature*, *468*, 426–430.
- Small, D., & Schubert, A. (2008). Guide to ASAR geocoding. *Issue, 1*, 2008.
- SNAP STEP. <http://step.esa.int/main/toolboxes/snap/>.
- SNAPHU. <http://web.stanford.edu/group/radar/softwareandlinks/sw/snaphu/>.
- Spaans, K., & Hooper, A. (2016). InSAR processing for volcano monitoring and other near-real time applications. *Journal of Geophysical Research: Solid Earth*, *121*, 2947–2960.
- Stramondo, S., Vannoli, P., Cannelli, V., Polcari, M., Melini, D., Samsonov, S., Moro, M., Bignami, C., & Saroli, M. (2014). X- and C-Band SAR Surface Displacement for the 2013 Lunigiana Earthquake (Northern Italy). A Breached Relay Ramp? *IEEE Journal of Selected Topics in Applied Earth Observations and Remote Sensing*, *7*, 2746–2753.
- Tarayre, H., & Massonnet, D. (1996). Atmospheric Propagation heterogeneities revealed by ERS-1 interferometry. *Geophysical Research Letters*, *23*, 989–992.
- Taylor, M., & Peltzer, G. (2006). Current slip rates on conjugate strike-slip faults in central Tibet using synthetic aperture radar interferometry. *Journal of Geophysical Research: Solid Earth*, *111*, n/a-n/a.
- Torres, R., Snoeij, P., Geudtner, D., Bibby, D., Davidson, M., Attema, E., Potin, P., Rommen, B., Floury, N., Brown, M., Traver, I.N., Deghaye, P., Duesmann, B., Rosich, B., Miranda, N., Bruno, C., L'Abbate, M., Croci, R., Pietropaolo, A., Huchler, M., & Rostan, F. (2012). GMES Sentinel-1 mission. *Remote Sensing of Environment*, *120*, 9–24.
- Trevett, J.W. (1987). Imaging radar for resources surveys. *Geocarto International*, *2*. <http://dx.doi.org/10.1080/10106048709354112>.
- Uppala, S.M., Kållberg, P.W., Simmons, A.J., Andrae, U., Bechtold, V.D.C., Fiorino, M., Gibson, J.K., Haseler, J., Hernandez, A., Kelly, G.A., Li, X., Onogi, K., Saarinen, S., Sokka, N., Allan, R.P., Andersson, E., Arpe, K., Balmaseda, M.A., Beljaars, A.C.M., van de Berg, L., Bidlot, J., Bormann, N., Caires, S., Chevallier, F., Dethof, A., Dragosavac, M., Fisher, M., Fuentes, M., Hagemann, S., Hólm, E., Hoskins, B.J., Isaksen, I., Janssen, P.A.E.M., Jenne, R., McNally, A.P., Mahfouf, J.-F., Morcrette, J.-J., Rayner, N.A., Saunders, R.W., Simon, P., Sterl, A., Trenberth, K.E., Untch, A., Vasiljevic, D., Viterbo, P., & Woollen, J. (2005). The ERA-40 re-analysis. *Quarterly Journal of the Royal Meteorological Society*, *131*, 2961–3012.
- Velez, M.L., Euillades, P., Caselli, A., Blanco, M., & Díaz, J.M. (2011). Deformation of Copahue volcano. Inversion of InSAR data using a genetic algorithm. *Journal of Volcanology and Geothermal Research*, *202*, 117–126.
- Wadge, G., Webley, P.W., James, I.N., Bingley, R., Dodson, A., Waugh, S., Veneboer, T., Puglisi, G., Mattia, M., Baker, D., Edwards, S.C., Edwards, S.J., & Clarke, P.J. (2002). Atmospheric models, GPS and InSAR measurements of the tropospheric water vapour field over Mount Etna. *Geophysical Research Letters*, *29*, 11-1-11-4.
- Wen, Y., Xu, C., Liu, Y., & Jiang, G. (2016). Deformation and Source Parameters of the 2015 Mw 6.5 Earthquake in Pishan, Western China, from Sentinel-1A and ALOS-2 Data. *Remote Sensing*, *8*, 134.
- Williams, S., Bock, Y., & Fang, P. (1998). Integrated satellite interferometry: Tropospheric noise, GPS estimates and implications for interferometric synthetic aperture radar products. *Journal of geophysical research*, *103*, 27051–27067.
- Woodhouse, I.H. (2005). *Introduction to microwave remote sensing*: CRC Press.

- Wright, T.J. (2004). Toward mapping surface deformation in three dimensions using InSAR. *Geophysical Research Letters*, 31.
- Xu, W.B., Li, Z.W., Ding, X.L., & Zhu, J.J. (2011). Interpolating atmospheric water vapor delay by incorporating terrain elevation information. *Journal of Geodesy*, 85, 555–564.
- Xu, Z.-W., Wu, J., & Wu, Z.-S. (2004). A survey of ionospheric effects on space-based radar. *Waves in Random Media*, 14, S189-S273.
- Yeh, K.C., & Liu, C.H. (1972). Theory of ionosphere waves. *Academic, San Diego, Calif.*
- Zebker, H.A., & Rosen, P. (1994). On the derivation of coseismic displacement fields using differential radar interferometry: The Landers earthquake. In *IGARSS '94 - 1994 IEEE International Geoscience and Remote Sensing Symposium* (pp. 286–288).
- Zebker, H.A., Rosen, P.A., & Hensley, S. (1997). Atmospheric effects in interferometric synthetic aperture radar surface deformation and topographic maps. *Journal of Geophysical Research: Solid Earth*, 102, 7547–7563.
- Zebker, H.A., & Villasenor, J. (1992). Decorrelation in interferometric radar echoes. *IEEE Transactions on Geoscience and Remote Sensing*, 30, 950–959.

A. DInSAR Scene



Figure 46: Intensity image in VV Polarization in ascending mode of SLC 02.03.2016. Product level: L1. Product name: SIA_S6_SLC_ISDV_20160302T145244_20160302T145307_010191_00F0AD_D28E.



Figure 47: Intensity image in VV Polarization in ascending mode of SLC 07.04.2016. Product level: L1. Product name: SIA_S6_SLC_ISDV_20160407T145244_20160407T145308_010716_00FFC7_A6F9.



Figure 48: Intensity image in VV Polarization in ascending mode of SLC 19.04.2016. Product level: LI. Product name: SIA_S6_SLC__ISDV_20160419T145245_20160419T145309_010891_01050B_A397.

B. Meteorology Data

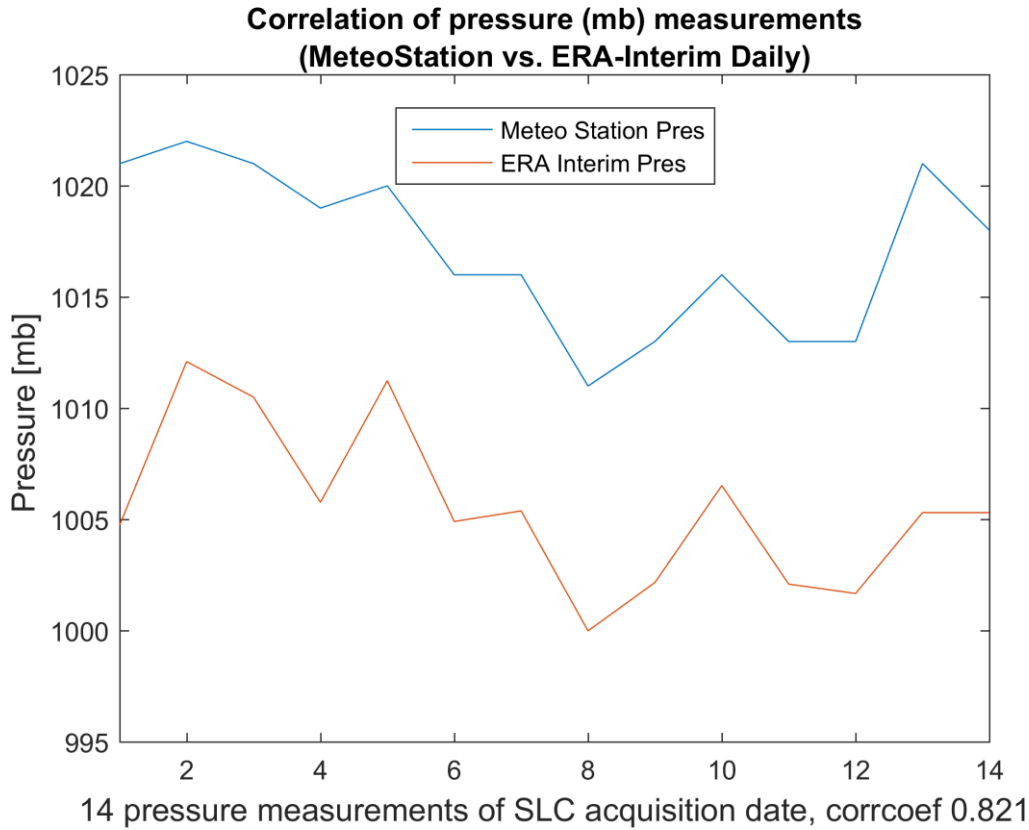


Figure 49: Correlation of atmospheric pressure meteorological data between the meteorological station St. Denis Gillot. The station is 20m above sea level.

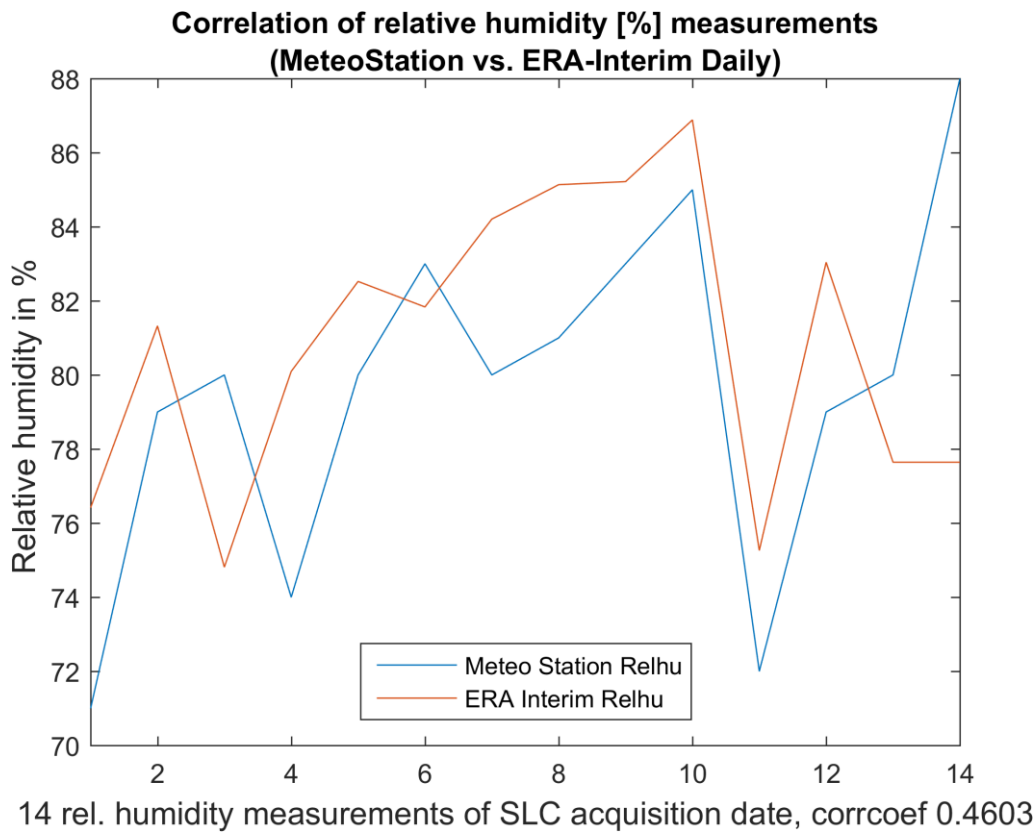
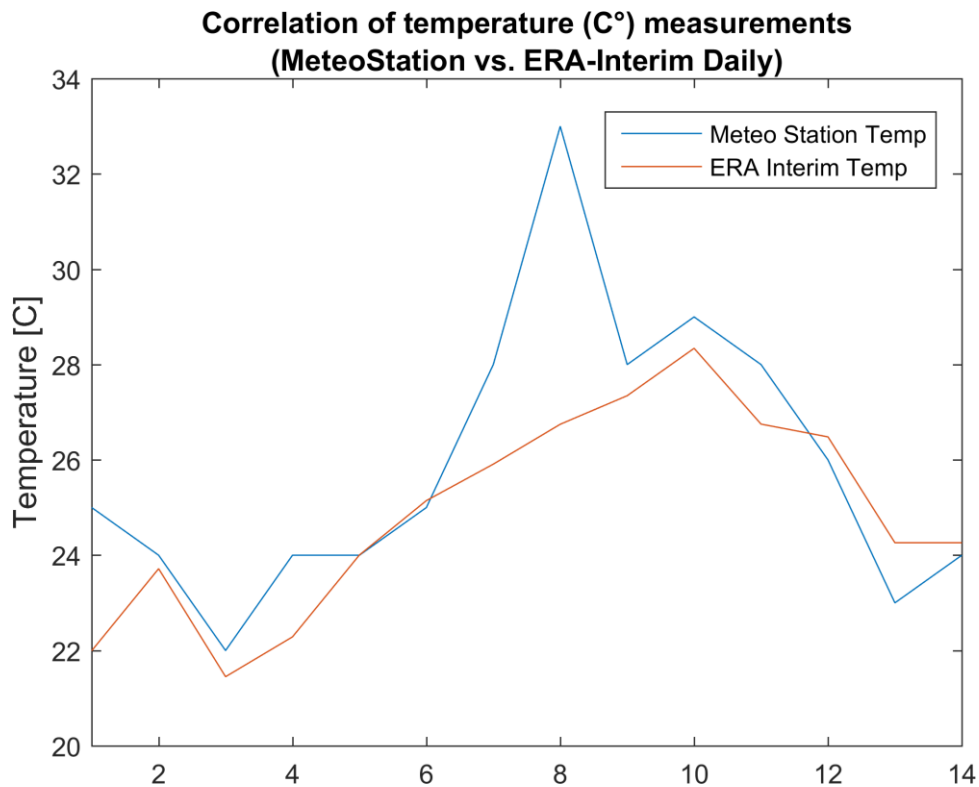
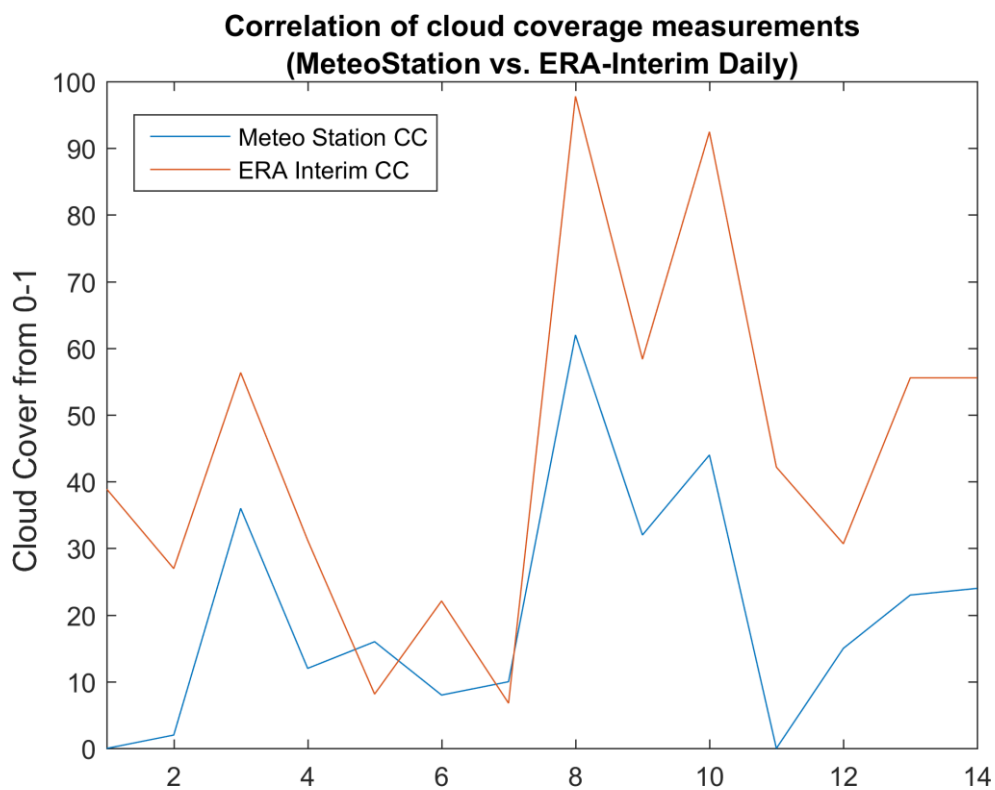


Figure 50: Correlation of relative humidity meteorological data between the meteorological station St. Denis Gillot. The station is 20m above sea level.



14 temperature measurements of SLC acquisition date, corrcoeff 0.774

Figure 51: Correlation of temperature meteorological data between the meteorological station St. Denis Gillot. The station is 20m above sea level.



14 cloud coverage measurements of SLC acquisition date, corrcoeff 0.822

Figure 52: Correlation of cloud cover meteorological data between the meteorological station St. Denis Gillot. The station is 20m above sea level.

C. Auxiliary product of the APD estimation and mitigation

TEC Maps

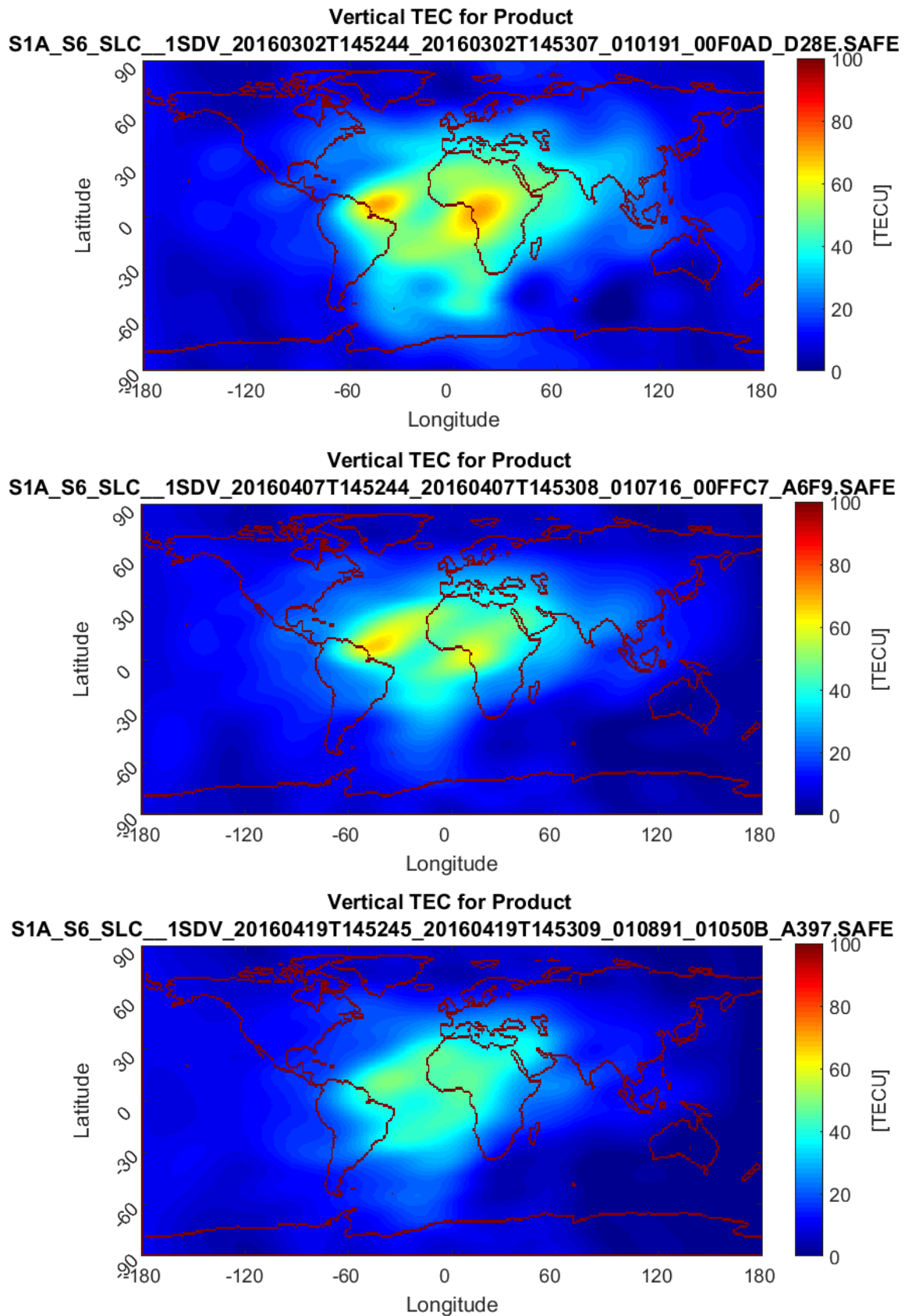


Figure 53: TEC Maps for the three SLC acquisition dates.

Auxiliary products of pair One

**02.03.16 & 07.04.16 unwrapped phase DInSAR
with SRTM 1sec coh>0.4 [cm]**

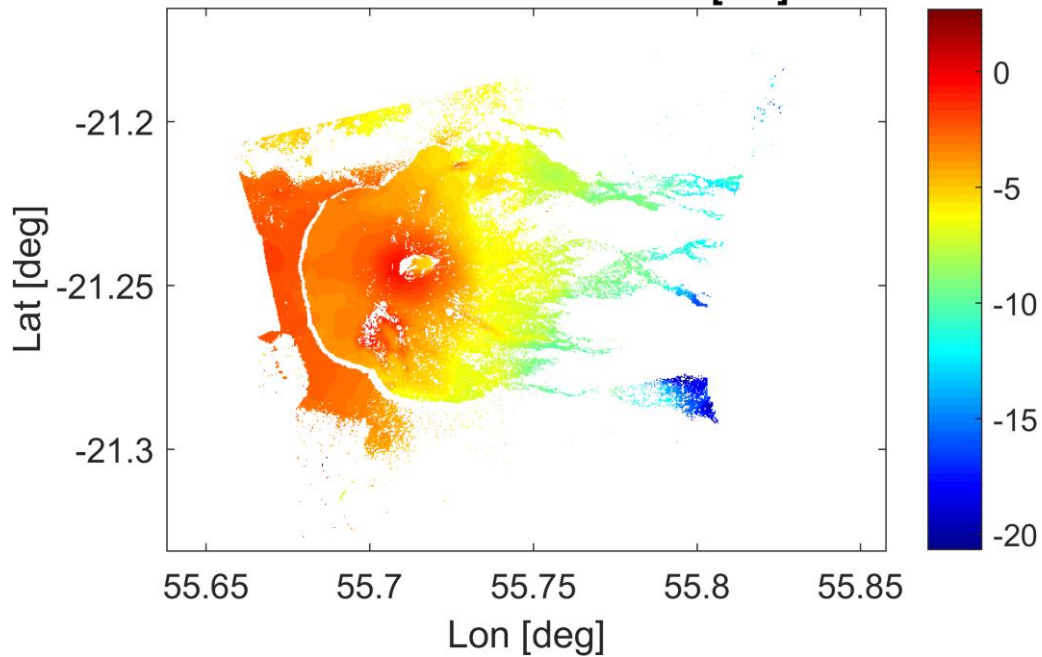


Figure 54: Unwrapped absolute values converted into cm, showing only the coherent pixels with values above 0.4 of pair One.

**02.03.16 & 07.04.16 atmospheric corrected DInSAR
DInSAR - total APD difference 2-way coh>0.4 [cm]**

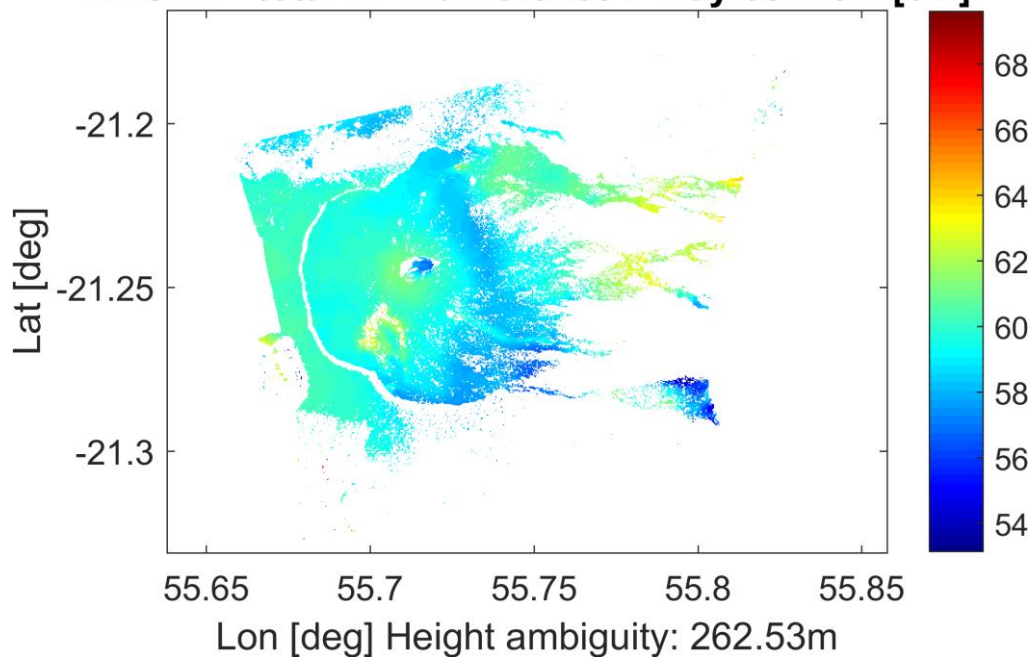


Figure 55: Atmospheric corrected DInSAR measurement with the total APD difference, showing only the coherent pixels with values above 0.4 of pair One.

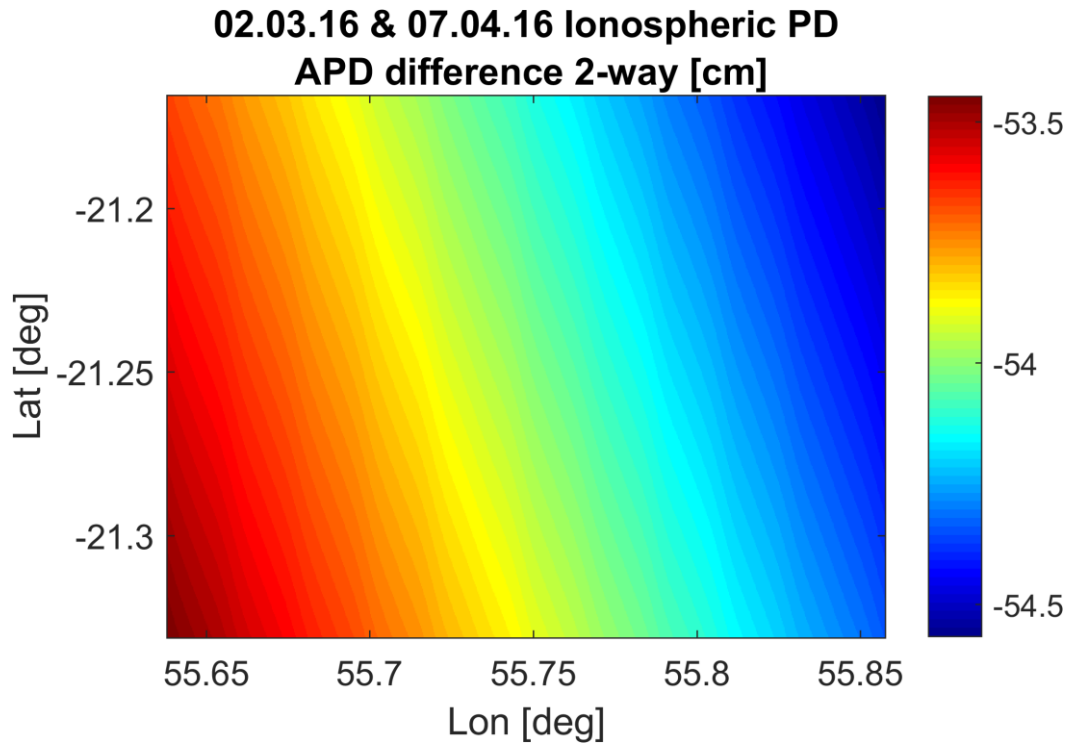


Figure 56: Only total ionospheric path delay difference (two-way) of pair Two.

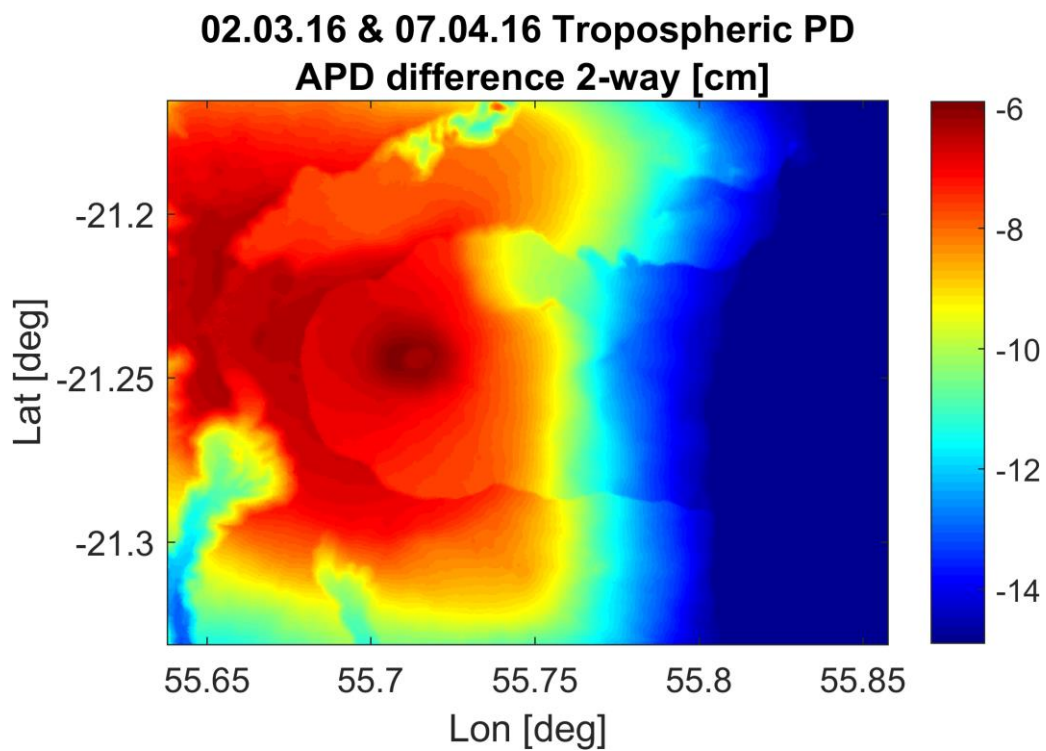


Figure 57: Only total tropospheric path delay difference (two-way) of pair Two.

Side products of pair Two

**02.03.16 & 19.04.16 unwrapped phase DInSAR
with SRTM 1sec coh>0.4 [cm]**

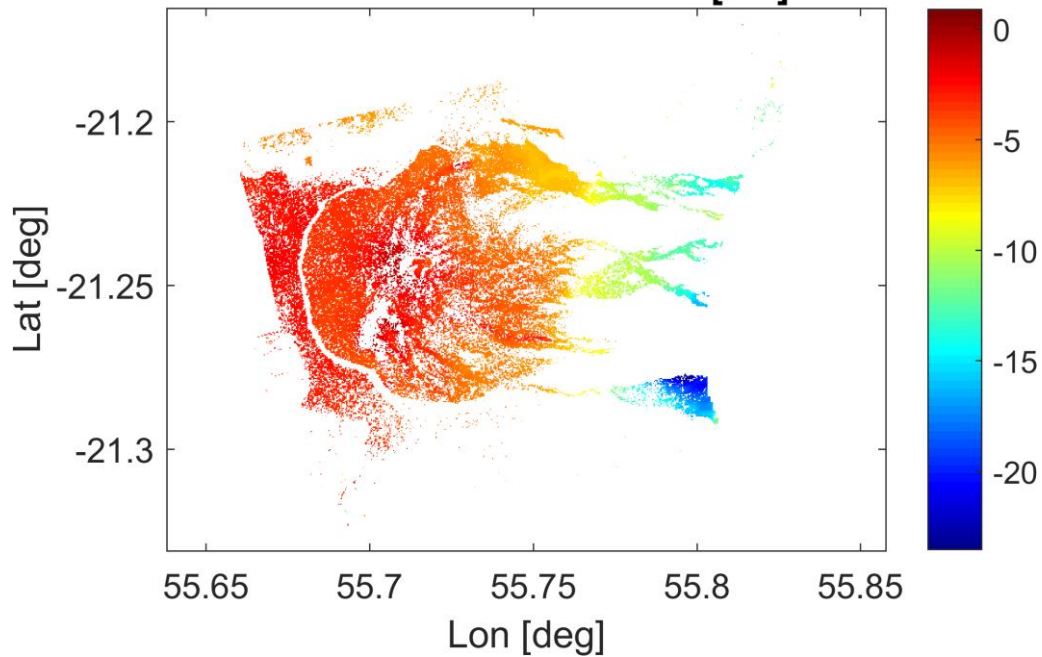


Figure 58: Unwrapped absolute values converted into cm, showing only the coherent pixels with values above 0.4 of pair Two.

**02.03.16 & 19.04.16 atmospheric corrected DInSAR
DInSAR coh>0.4 - total APD difference 2-way [cm]**

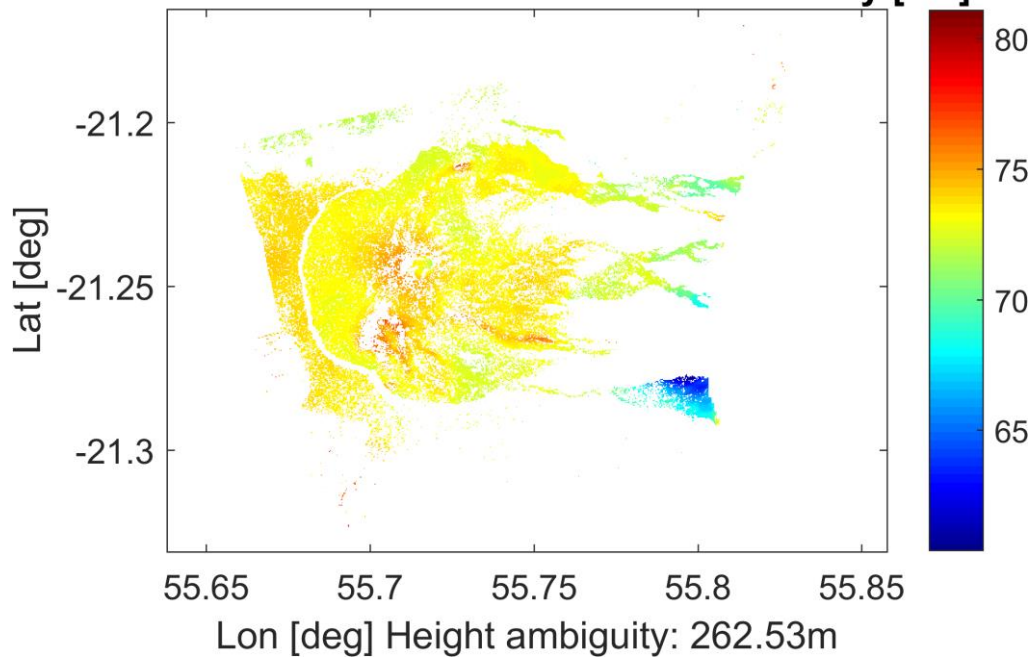


Figure 59: Atmospheric corrected DInSAR measurement with the total APD difference, showing only the coherent pixels with values above 0.4 of pair Two.

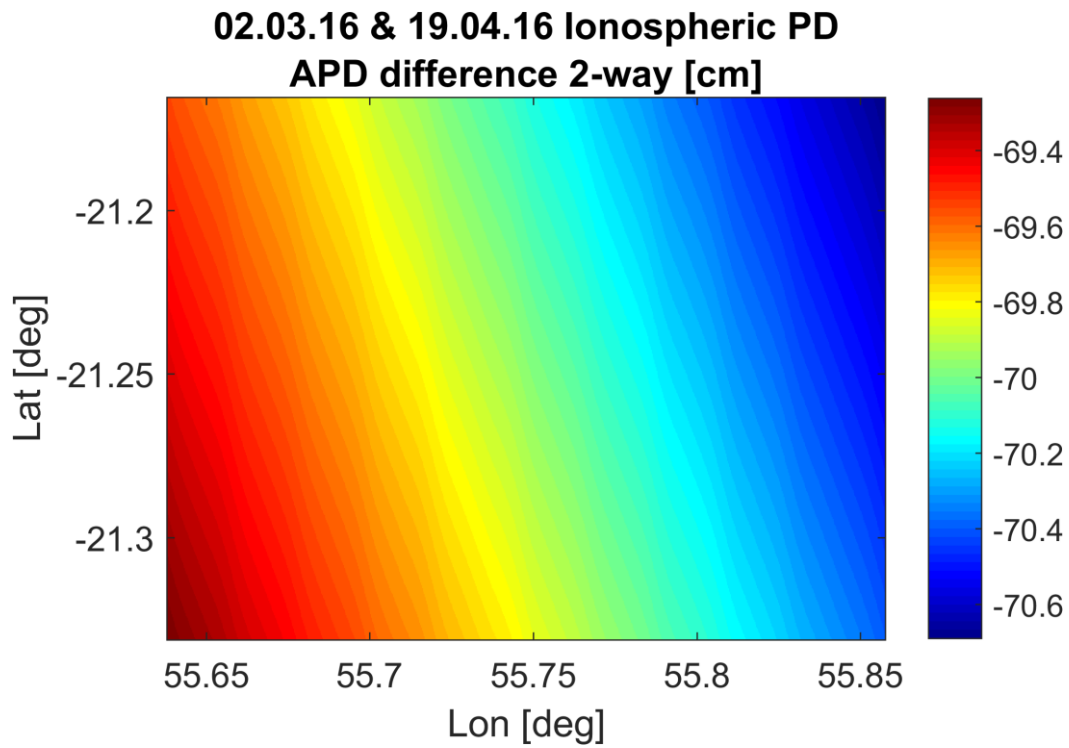


Figure 60: Only total ionospheric path delay difference (two-way) of pair Two.

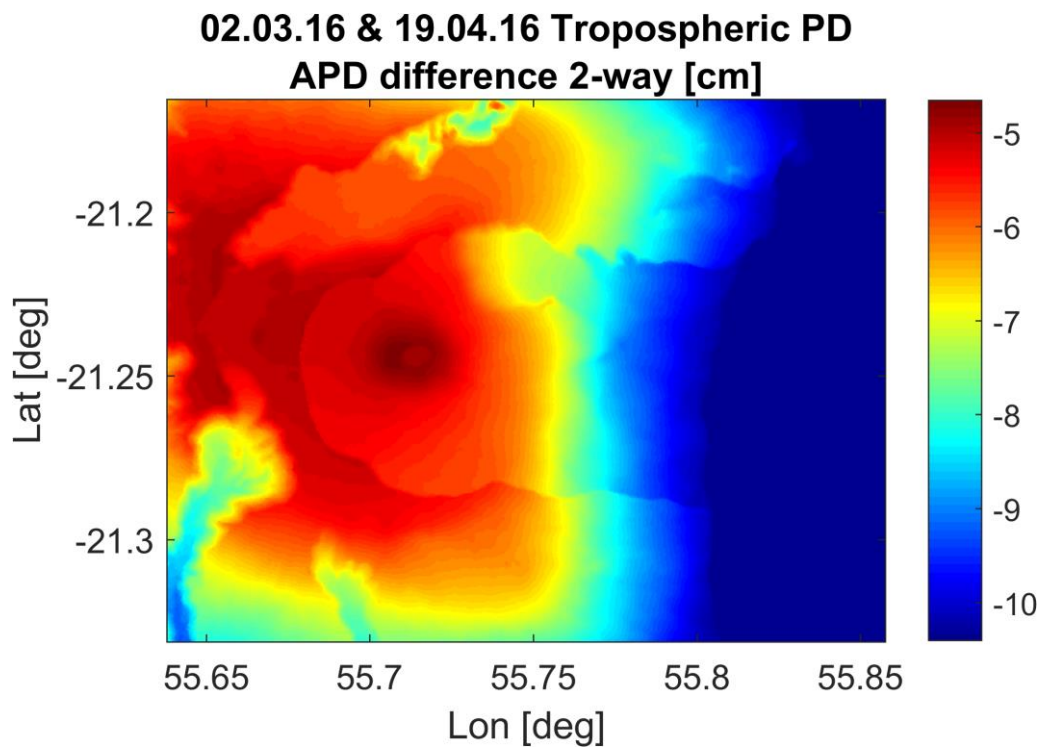


Figure 61: Only total tropospheric path delay difference (two-way) of pair Two.

Personal Declaration

« Hereby I declare that the submitted thesis is the result of my own, independent work. All external sources are explicitly acknowledged in the thesis. Additionally, I affirm that I did not use the contents of this work for obtaining credits otherwise. »

Zurich, September 30th, 2016

Philippe Ott

Reference Management System: Citavi v.5.4.0.2

Citation Style: Remote Sensing of Environment